Local and Upscale Impacts of Airflow over Mountains: Finite Amplitude Dynamics and Downslope Windstorm Predictability

Johnathan Metz

A dissertation
submitted in partial fulfillment of the
requirements for the degree of

Doctor of Philosophy

University of Washington

2021

Reading Committee:

Dale R. Durran, Chair

Lynn McMurdie

Gregory Hakim

Program Authorized to Offer Degree:
Atmospheric Sciences

University of Washington

Abstract

Local and Upscale Impacts of Airflow over Mountains: Finite Amplitude Dynamics and Downslope Windstorm Predictability

Johnathan Metz

Chair of the Supervisory Committee:
Professor Dale R. Durran
Atmospheric Sciences

Mountain waves are gravity waves generated by flow over terrain. The generation of these waves is significant for both their local impacts in mountainous areas, such as strong downslope winds, and their broader impacts on the general circulation through effects such as gravity wave drag and the Brewer-Dobson circulation. In this dissertation, we analyze two facets of mountain wave-induced dynamics: impacts of nonlinearity on mountain wave amplitude and predictability of downslope windstorms.

Linear assumptions have long been used to formulate parameterizations of gravity wave drag. However, previous results have indicated significant discrepancies between linear theory and the nonlinear solution, particularly in the presence of the tropopause. In our work, we conduct a systematic evaluation of nonlinear effects in a 2D framework, beginning with the simplest case of two layers of constant static stability and no shear. We then include cases of more complexity, including low-level inversions and forward shear in the troposphere. Our results verify the results from previous studies. In addition, our results show that in the presence of a tropopause and strong forward shear, there can exist a much larger amplification or deamplification of the surface pressure drag due to finite-amplitude nonlinear effects than was previously recognized. This has significant implications for the parameterization of gravity wave drag, as the accurate estimation of the surface pressure drag is important for

representing the true drag aloft.

More direct impacts to communities in the immediate lee of mountains are caused by downslope windstorms. Such windstorms can cause large amounts of property damage and extreme fire spread, and their accurate prediction is therefore important. Although some early studies suggested high predictability for downslope windstorms, more recent analyses have found limited predictability of these events. However, there is a theoretical reason to suspect higher predictability in cases with a mean-state critical level, and this is supported by at least one previous study. To investigate downslope windstorm predictability, we compare ensemble simulations from the NCAR ensemble to observed winds at stations determined to be susceptible to strong downslope flows. Although our results indicate some improvement in predictive skill for the mean-state critical level regime in certain contexts, the trade-offs are such that there is no significant practical difference in either ensemble spread or forecast skill for the mean-state critical-level regime.

TABLE OF CONTENTS

Page

List of Figures ii

Chapter 1: Introduction 1
1.1 Relevant Mountain Wave Theory 2
1.2 Downslope Windstorms 4
1.3 Dissertation Organization 16

Chapter 2: Finite-Amplitude Effects On Non-breaking Mountain Waves 17
2.1 Introduction and Background 17
2.2 Model Description 22
2.3 Upstream Environments 26
2.4 Results 27
2.5 Discussion 38
2.6 Conclusions 45

Appendices 49
2.A Generation of Shear Soundings 49
2.B Computation of Linear Streamlines 50

Chapter 3: Predictability of Downslope Windstorms in Critical-Level and Non-Critical-Level Environments 55
3.1 Introduction and Background 55
3.2 Methodology 57
3.3 Results 74
3.4 Discussion and Conclusions 87

Chapter 4: Conclusions 90

LIST OF FIGURES

Figure Number Page

1.1 Shallow water flow over an obstacle for a) supercritical flow, b) subcritical flow, and c) subcritical flow that transitions to supercritical flow at the crest, resulting in a hydraulic jump downstream. Reproduced from Durran (2015a). 7

1.2 Schematic of the setup of the problem considered in Smith (1985). The upper boundary condition is the height of the dividing streamline, $H_0 + \delta_c$, while the lower boundary condition is a function of the mountain height $h(x)$. The well-mixed region, denoted by carets, has a density ρ_c equal to that of the upstream density at the dividing streamline. Reproduced from Smith (1985). 11

1.3 Solution curves from Smith (1985), as adapted by Durran and Klemp (1987). The x-axis is a nondimensionalized mountain height, where $l \equiv N/U$ is the Scorer parameter. Similarly, the y-axis is a nondimensionalized streamline displacement. Solution curves are plotted for varying values of the upstream dividing streamline height H_0, nondimensionalized such that the numeric values correspond to multiples of 1/12 of a hydrostatic vertical wavelength $2\pi/l$. Symbols h, δ_c, and H_0 are defined and visualized in Fig. 1.2. (Reproduced from Durran and Klemp (1987).) 14

2.1 Comparison of streamlines of the one-layer linear (black) and nonlinear (red) solutions for a Witch of Agnesi mountain with $a = 10\,\text{km}$ and $Nh_m/U = 0.6$. Airflow is left to right; the mountain profile is shown in blue. 19

2.2 Comparison of a $\cos^4$ (blue) and a Witch of Agnesi (orange) profile with the same values of h_m and a. 25

2.3 Vertical profiles of (a) Brunt-Väisälä frequency N and (b) horizontal wind speed U for an Experiment-3 case with the tropopause height set at 10 km. . 28

2.4 Cross-mountain pressure drag $\tilde{D}_l$ as a function of nondimensional tropopause height $\tilde{z}_T$ for Experiment 1 computed by the semi-analytic method (blue line) and using the linearized meso12 model run to steady state (orange points). . 30

2.5 (a) Normalized cross-mountain pressure drag $\tilde{D}_{nl}$ for the Experiment-1 simulations contoured as a function of nondimensional mountain and tropopause heights, and (b) Amplification of the nonlinear drag relative to that for the corresponding linear solution. The linear solution is plotted at a mountain height of 0.0. The thick black line indicates a normalized pressure drag or amplification of 1.0. White areas are plotted for those values of $\tilde{h}_m$ and $\tilde{z}_T$ that produce breaking mountain waves. The black dashed line, satisfying $\tilde{z}_T = 1.17\tilde{h}_m + 0.5$, is an empirical fix to the set of $(\tilde{h}_m, \tilde{z}_T)$ along which $\tilde{D}_{nl}$ is maximized and is discussed in connection with Fig. 2.13. 31

2.6 Vertical velocity (colour fill) and streamlines (black lines) from the (a) linear and (b) nonlinear meso12 simulations of an Experiment-1 case with nonlinear amplification in which $\tilde{z}_T = 0.55\lambda_L$ and $\tilde{h}_m = 0.3$. The grey line indicates the tropopause, and grey stippling indicates the stratosphere. 34

2.7 As in Fig. 2.6, but for a case with nonlinear deamplification in which $\tilde{z}_T = 0.45\lambda_L$ and $\tilde{h}_m = 0.6$. 34

2.8 Normalized drag $\tilde{D}_{nl}$ as in Fig. 2.5a for the Experiment-2 simulations with (a) $\Delta z = 1\,\text{km}$ and (c) $\Delta z = 2\,\text{km}$. Amplification of the drag relative to the linear solution $\tilde{D}_{nl}/\tilde{D}_l$ as in Fig. 2.5b for cases with (b) $\Delta z = 1\,\text{km}$ and (d) $\Delta z = 2\,\text{km}$. 35

2.9 (a) Normalized drag $\tilde{D}_{nl}$ and (b) amplification of the drag relative to the linear solution $\tilde{D}_{nl}/\tilde{D}_l$, as in Fig. 2.5, for the Experiment-3 simulations. . . . 36

2.10 As in Fig. 2.6, but for the 10 m/s to 30 m/s shear sounding with a tropopause height of $z_T = 8\,\text{km}$ and a mountain height of $h_m = 800\,\text{m}$. 37

2.11 (a) Normalized drag $\tilde{D}_{nl}$ and (b) amplification of the drag relative to the linear solution $\tilde{D}_{nl}/\tilde{D}_l$, as in Fig. 2.5, for the Experiment-4 simulations. . . . 39

2.12 As in Fig. 2.6, but for Experiment 4 with $h_m = 800\,\text{m}$ and $z_T = 11\,\text{km}$. . . . 39

2.13 Normalized pressure drag as a function of mountain height along the dashed lines in Figs. 2.5a, 2.9a and 2.11a for the no-shear case (blue), the lower-level/upper-level maximum in the 10-30 m/s case (green/orange), and for the 10-50 m/s case (red). 40

2.14 Local pressure drag for the (a) no-shear case, (b) 10-30 m/s shear case, and (c) 10-50 m/s shear case. Blue, orange, green, and red lines are for mountain heights of 200 m, 400 m, 600 m, and 800 m, respectively. Tropopause heights are $\tilde{z}_T = 0.65$ for the no-shear case and $z_T = 8\,\text{km}$ and $z_T = 11\,\text{km}$ for the 10-30 m/s and 10-50 m/s shear cases, respectively. For reference, the mountain profile is plotted as a black dashed line. 43

2.15 Vertical profiles of (a, c) Scorer parameter l squared (red) and (b, d) real part of the Fourier-transformed vertical velocity $\hat{w}(z)$ for the trapped wave mode supported by the (a, b) 10-30 m/s shear case with a tropopause height of 8 km and (c, d) 10-50 m/s shear case with a tropopause height of 11 km. The horizontal wavenumber k of this mode is plotted as the blue vertical line in (a, c). The grey shading in (b, d) indicates the interval $[-|\hat{w}|, |\hat{w}|]$, where $|\hat{w}|$ is the magnitude of $\hat{w}$. The parameters λ_x and D_λ indicate the horizontal wavelength and downstream decay per wavelength, respectively. 44

2.16 Demonstration of the construction of a wind profile in the stratosphere. The blue curve indicates the solution for a constant Scorer parameter l. The red dot indicates the first point with zero curvature above the tropopause, while the green curve indicates the ellipse used to transition between the constant-l and constant-U profiles. The resulting wind profile is shown in black. 51

2.17 Comparison between two methods of plotting linear streamlines in flow from left to right over a Witch of Agnesi mountain: red lines use Eqs. 2.26 and 2.27; black lines use Eqs. 2.28 and 2.29. The mountain profile is shown in blue and coincides with the lowest black streamline. 54

3.1 Regions satisfying the small-scale criterion (purple color fill) and the boundary of the large-scale criterion (red contour). 61

3.2 Location of the 15 selected observation stations in the western United States. 64

3.3 Station location relative to terrain for stations on the east side of mountain ranges. Filled contours indicate terrain height, with darker shades of gray indicating progressively higher terrain. Terrain contours are in 250 m intervals. The mountain-normal vector for each station is plotted as a red arrow. . . . 65

3.4 As in Fig. 3.3, but for stations on the west side of mountain ranges. The left-most panel is magnified in space by a factor of two for clarity. 66

3.5 Relevant windstorm parameters for station CO109 in Boulder, CO. From top to bottom: Cross-mountain wind-component (color fill) and critical level height (when present, dashed); ensemble wind speed (thin colored curves), mean ensemble wind speed (thick solid red curve), and observed sustained winds (solid black curve) and gusts (dashed black curve); as in the panel above, but for wind direction; and standard deviation of the ensemble members. Winds below mountain-top height are not plotted (white area) in the top panel. 68

3.6 As in Fig. 3.5, but for Sill Hill, CA (SILSD). 69

3.7 From top to bottom: average ensemble spread and 95% confidence intervals as a function of lead time for no-CL events (blue), low-CL events (orange), and high-CL events (green); average ensemble spread scaled by the average ensemble mean; the average ensemble mean as a function of lead time and critical level presence/height; and the number of data samples as a function of lead time and critical level presence/height. 75

3.8 Root mean square error (solid) and corrected ensemble spread, calculated as in Eq. 3.4 and multiplied by the correction factor $\sqrt{11/10}$ (dashed), as a function of lead time for the no-CL (blue), low-CL (orange), and high-CL (green) cases. The dashed curves differ from the curves shown in the top panel of Fig. 3.7 in that these curves are the square root of the average variance instead of the average standard deviation. 77

3.9 Number of no-critical-level bins at each station where the ensemble forecast a windstorm and one was observed (true positives; green), where the ensemble forecast a windstorm and none was observed (false positives; blue), and where the ensemble did not forecast a windstorm and one was observed (false negatives; orange). POD, FAR, and CSI are shown for each station. Station names are printed in black for those stations on the east side of mountain ranges; those on the west are shown in red. 79

3.10 As in Fig. 3.9, but for critical level bins. 81

3.11 Comparison of no-CL and CL events for all stations aggregated together. The meaning of bar colors is equivalent to Fig. 3.9. 82

3.12 POD (blue), FAR (orange), and CSI (green) as a function of ensemble member threshold for the no-CL (solid) and CL (dashed) cases. 84

3.13 As in Fig. 3.11, but for verification windows of 3 and 12 hours. 85

3.14 As in Fig. 3.11, but with the critical level cases separated into low ($z < 8\,\mathrm{km}$) and high ($z \geq 8\,\mathrm{km}$) cases. 86

ACKNOWLEDGMENTS

First and foremost, I am deeply indebted to my graduate advisor, Dale Durran, who provided so much mentoring and guidance throughout the past six years. I have truly grown as a scientist and a person throughout graduate school, and that is in no small part due to him. Thank you, Dale.

I would also like to thank the rest of my committee members, both for my master's degree and for this doctoral degree: Lynn McMurdie, Greg Hakim, Chris Bretherton, Jim Doyle, Bernard Deconinck, and Kyle Armour. Their feedback and advice was instrumental in this process. I am also extremely grateful to my undergraduate mentors, Gretchen Mullendore and Mike Fiorino, for their guidance and preparation as I made my way through my undergraduate studies and began graduate school. Their advice is what truly led me here.

I also wish to thank the rest of the faculty and staff of both the departments of Atmospheric Sciences and Applied Mathematics. In particular, many thanks to the academic advisors over the years—Melissa Pritchard, Erica Coleman, Jennifer Siembor, and Lauren Lederer—for their guidance and always helpful checklists as I navigated through my various programs. Thank you also to David Warren for his always fun conversations about computing and helpful solutions to any problems I had. I would also like to acknowledge funding support from the American Meteorological Society, who funded the first year of my graduate studies through an AMS Graduate Fellowship, and the National Science Foundation, who provided support through grants AGS-1138977 and AGS-1929466.

I am extremely grateful to my family—Mom, Dad, Janessa, Grandma, Grandpa, and all the others—for always being supportive in my endeavors and helping me along the way. I know I wouldn't have been able to do it without you.

Thank you also to all of my friends—from UND, UW, and beyond—who made my educational experience the best time of my life.

Finally, I would like to thank my partner, Preston, for all his support and understanding as I worked to finish this degree over the past three years. I am so happy that we were on this journey together. I know that it wasn't always easy, but we made it!

DEDICATION

To Grandpa Chuck, for starting me down this path and leading me here.

Chapter 1

INTRODUCTION

Mountain waves are generated when stably-stratified air flows over a mountain barrier and are responsible for multiple effects in the atmosphere (Durran, 1990). Gravity waves in the atmosphere act to redistribute momentum, and the drag force induced on the atmosphere by a mountain is not typically exerted on the low-level flow. Instead, this drag force is communicated upward through the atmosphere by mountain waves and exerted at some higher level (Eliassen and Palm, 1960).

This gravity wave drag (GWD) has been shown to have a significant decelerative effect in the upper troposphere and stratosphere (McFarlane, 1987), and efforts to parameterize it in numerical weather prediction and general circulation models (NWP and GCMs, respectively) have been an active area of research since the 1980s (Palmer et al., 1986; McFarlane, 1987; Kim and Arakawa, 1995; Lott and Miller, 1997; Kim and Doyle, 2005). Implementation of even the most basic GWD parameterization has been shown to significantly improve forecast skill (Palmer et al., 1986).

While GWD has a significant impact on the large-scale circulation, local impacts from mountain waves can also be significant. The strong updrafts associated with mountain waves have long been sought out by glider pilots. In fact, the highest altitude records set by glider pilots have been in the vicinity of mountainous regions using this exact mechanism.

One further local impact related to mountain wave motions is that of downslope windstorms. These windstorms exhibit extremely strong flow down the mountain, sometimes in excess of $50\,\mathrm{m\,s^{-1}}$. For communities located at the base of terrain susceptible to these flows, property damage due to downslope windstorms is a primary concern. In addition, in areas such as the American West, mountainous terrain coupled with relatively dry climates result

in areas prone to severe fire spread from these windstorms.

In this dissertation, we examine two distinct research questions related to airflow over mountains. The first is an investigation of the degree to which finite-amplitude topography influences the amplitude of the resulting mountain wave. The second is a study of the predictability of downslope windstorms in the presence of a mean-state critical level.

1.1 Relevant Mountain Wave Theory

In two-dimensional, inviscid, adiabatic, linear Boussinesq flow with Coriolis forces neglected, the equation governing steady-state flow over a mountain is

$$\left(\frac{\partial^2}{\partial x^2} + \frac{\partial}{\partial z^2}\right) w + \left(\frac{N^2}{U^2} - \frac{1}{U}\frac{d^2U}{dz^2}\right) w = 0, \tag{1.1}$$

where x and z are the horizontal and vertical coordinates, $w(x, z)$ is the vertical velocity, $N(z)$ is the Brunt-Väisälä frequency, and $U(z)$ is the base-state vertical velocity. Eliassen and Palm (1960) show that for waves satisfying Eq. 1.1 that have mountain profiles which approach zero at $x = \pm\infty$, the horizontally integrated vertical momentum flux,

$$\rho_0 \int_{-\infty}^{\infty} u'w' \, dx, \tag{1.2}$$

is constant with height. Here, u' and w' are the perturbation horizontal and vertical velocities, respectively, and ρ_0 is a constant reference density. (Note that since there is no base state vertical velocity, $w = w'$.) Therefore, all drag force exerted on the flow by the mountain is propagated upward without inducing any change in the mean flow wherever Eq. 1.1 holds.

It is clear from examination of Eq. 1.1 that a singularity is present when $U = 0$. A level where $U = 0$ is known as a critical level. More precisely, this is a *mean-state* critical level. This is the only type of critical level possible in linear theory; however, in the true nonlinear case, where the total horizontal wind velocity $u = U(z) + u'$ is the relevant quantity, another type of critical level is possible. This is the *self-induced* critical level and occurs when the wave amplitude is so strong that overturning occurs and therefore $u' = -U$ at some location.

Booker and Bretherton (1967) examined the behavior of linear waves interacting with a mean-state critical level. They found that if the Richardson number

$$\mathrm{Ri} \equiv \frac{N^2}{U_z^2} \tag{1.3}$$

was greater than 1/4 at the critical level, the wave is largely absorbed, and momentum is transferred to the mean flow. This momentum deposition results in the drag known as gravity wave drag (GWD). On the other hand, if $\mathrm{Ri} < 1/4$ at the critical level, waves incident on the critical level from below are largely reflected. Although this result stems entirely from linear theory, results by Peltier and Clark (1983) demonstrate that the self-induced critical level, an inherently finite amplitude phenomenon, behaves largely as would be expected from the Booker and Bretherton (1967) result for a critical level with $\mathrm{Ri} < 1/4$. The resulting wave reflection has strong implications for downslope windstorms, as noted in both a linear sense by Clark and Peltier (1984) and a finite-amplitude sense by Smith (1985).

Of course, the behavior of solutions to Eq. 1.1 is strongly influenced by the quantity

$$l^2 \equiv \frac{N^2}{U^2} - \frac{1}{U}\frac{d^2U}{dz^2}. \tag{1.4}$$

This quantity was first derived by Scorer (1949). It, or rather its square root, is known as the *Scorer parameter*. In a manner analogous to sharp changes in the refractive index of light, sharp changes in the Scorer parameter with height can result in partial or total wave reflections. These wave reflections can constructively or destructively interfere with the primary wave and have an impact on the resulting amplitude of the wave system. As the wave amplitude at the surface is directly related to the drag force induced on the atmosphere, such wave reflections have an impact on the magnitude of gravity wave drag. Previous studies, such as Durran (1986) and Durran (1992), have indicated potential significant deviations from the amplitude predicted by linear theory when nonlinearity and finite-amplitude effects are present. We examine the effects of these sharp discontinuities, as well as the impacts of background shear, on mountain wave amplitude in the finite-amplitude system later in this dissertation.

1.2 Downslope Windstorms

Downslope windstorms, as indicated by the name, are weather events characterized by severely strong winds flowing down a mountain slope. Such winds are relatively common in the lee of mountains, and can account for severe property damage in these regions. Furthermore, in dry mountainous regions prone to fire weather, downslope windstorms can contribute significantly to fire spread (e.g. Brewer and Clements, 2020; Mass and Ovens, 2021). For these reasons, understanding the dynamics of downslope windstorms, particularly as it relates to accurate forecasting of these events, is an important forecast goal.

Early theories about the development of downslope windstorms relied upon two different dynamical mechanisms: linear mountain wave theory and hydraulic theory. Both have their benefits and drawbacks. While linear mountain wave theory is easily applied to the atmosphere, it is obviously unable to account for nonlinear effects. Hydraulic theory, on the other hand, does take into account nonlinear effects, but its direct application to the atmosphere is difficult.

1.2.1 Linear Mountain Wave Theory

The attempt to describe downslope windstorms using linear mountain wave theory is largely due to Klemp and Lilly (1975). As discussed above in regards to nonlinearity, when a sharp interface is present, partial reflections can occur at the interface. The phase of the wave incident on the interface determines the degree of constructive or destructive interference. For a two layer system with the basic-state Brunt-Väisälä frequency N and wind speed U constant with height in each layer, Klemp and Lilly (1975)'s linear analysis shows that the maximum amplification factor is $\max(N_U/N_L, N_L/N_U)$, where N_U and N_L are the Brunt-Väisälä frequencies of the upper and lower layers, respectively. However, since the degree of amplification is reliant on the phase of the wave, the actual amplification factor is highly sensitive to the height of the interface. For physically relevant values where $N_U/N_L = 2.0$, the amplification factor in fact ranges from 0.5 (a *deamplification!*) to 2.0.

Real-world downslope windstorms often feature low-level stable layers. Incorporating a third layer into their model, Klemp and Lilly (1975) found that the maximum amplification factor in this system is $N_3 N_1 / N_2^2$. Here the index increases such that N_1 represents the lowest layer and N_3 the highest. Note that in this instance, increasing the static stability of either the low-level stable layer or the stratosphere increases the maximum amplification factor, although again the exact value for the amplification factor is highly sensitive to the exact heights of the interfaces.

While linear theory has the advantage that quite general atmospheric profiles can be considered and analyzed, its applicability to finite-amplitude flows that are more nonlinear is questionable. Durran (1992) found significant differences in the wave response and amplitude such that the applicability of linear theory for mountain heights significant enough to generate large-amplitude lee flows is difficult. An alternative theory based on analogy to hydraulic shallow-water theory allows for nonlinearity, but it has its own difficulties with application to the atmosphere, as will be discussed below.

1.2.2 Hydraulic Theory

The hydraulic analog for downslope windstorms is related to the concept of a hydraulic jump, such as that found downstream of an obstacle in a river. Such jumps are predicted by shallow water theory in certain contexts, which are related to the criticality of the flow over the obstacle. The following discussion is based upon that of Durran (1990) and Durran (2015a).

If the flow is steady and hydrostatic, and if the flow does not vary in the coordinate parallel to the obstacle, the horizontal shallow-water momentum equation is

$$u\frac{\partial u}{\partial x} + g\frac{\partial D}{\partial x} = -g\frac{\partial h}{\partial x}. \tag{1.5}$$

Here, x is the horizontal coordinate perpendicular to the obstacle, u is the velocity in the x direction, D is the depth of the fluid, and h is the height of the obstacle.

In addition, the flow is also governed by the shallow-water continuity equation

$$\frac{\partial uD}{\partial x} = 0. \tag{1.6}$$

Substitution of Eq. 1.6 into Eq. 1.5 yields

$$\left(1 - \mathrm{Fr}^{-2}\right) \frac{\partial}{\partial x} \left(D + h\right) = \frac{\partial h}{\partial x}, \tag{1.7}$$

where

$$\mathrm{Fr} = \frac{u}{\sqrt{gD}} \tag{1.8}$$

is the *Froude number*. This quantity is the ratio between the horizontal velocity u and the phase speed $\sqrt{gD}$ of a shallow-water gravity wave.

Eq. 1.7 has a simple interpretation. Since $D + h$ is the height of the free surface, Eq. 1.7 determines how the height of the free surface changes due to the obstacle below. The sign of $\left(1 - \mathrm{Fr}^{-2}\right)$ determines whether the free surface rises or falls for a given change in the obstacle height. If $\mathrm{Fr} > 1$ everywhere, $1 - \mathrm{Fr}^{-2} > 0$ everywhere, and the free surface rises (falls) as the obstacle height increases (decreases). This is known as *supercritical* flow. Such a case is shown in Fig. 1.1a. If, on the other hand, $\mathrm{Fr} < 1$ everywhere, the free surface falls (rises) as the obstacle height increases (decreases). This is known as *subcritical* flow. This case is shown in Fig. 1.1b.

The case relevant to downslope windstorms occurs when there is a transition from subcritical flow to supercritical flow over the obstacle. In this case, the upstream side is subcritical, and therefore the free surface decreases as the flow ascends the obstacle. However, the downstream side is supercritical, and therefore the free surface continues to decrease as the flow descends the lee side. The convergence at the interface between the shallow, fast-moving fluid and the ambient slower-moving fluid downstream eventually results in a shock. In a physical system, the shock degenerates into turbulence and results in a *hydraulic jump*. The resulting situation is shown in Fig. 1.1c. Note, however, that since the jump is caused by turbulence, it cannot be explicitly accounted for in the shallow water system.

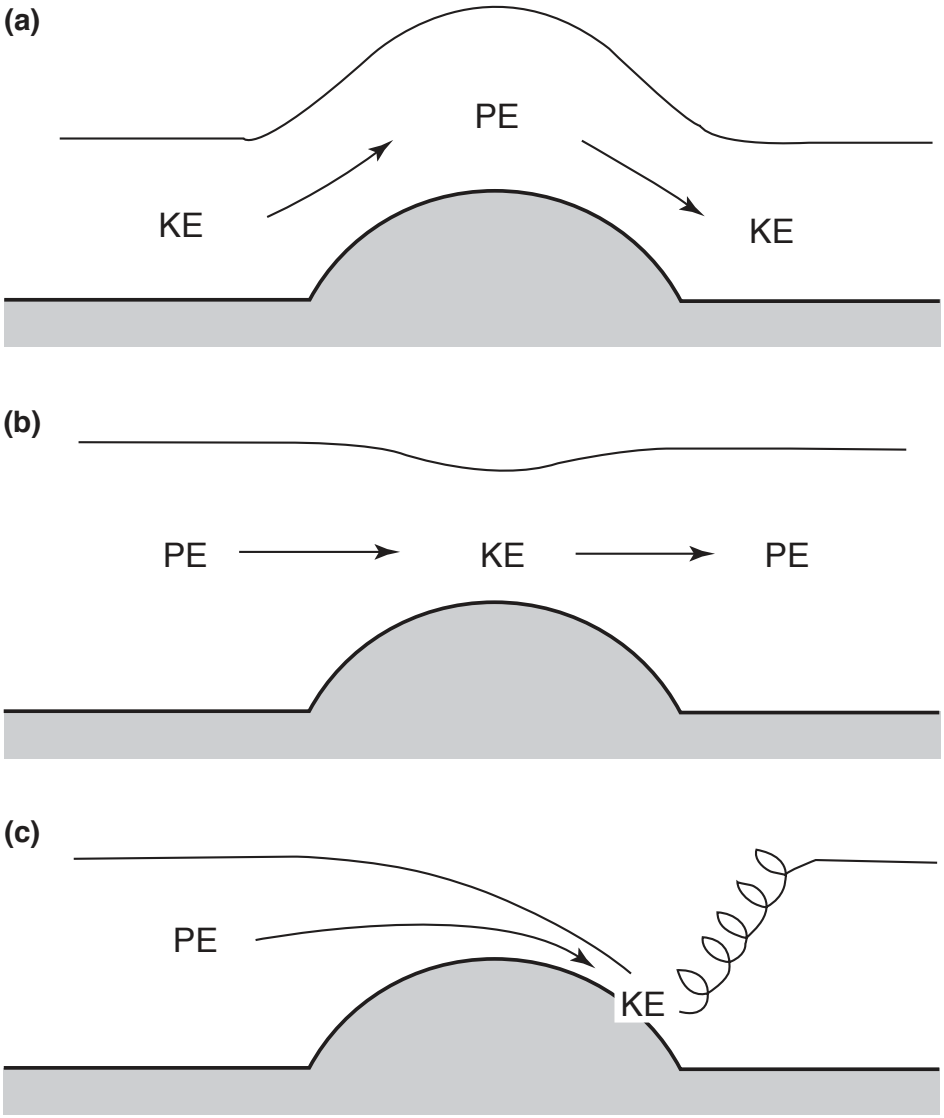

Figure 1.1: Shallow water flow over an obstacle for a) supercritical flow, b) subcritical flow, and c) subcritical flow that transitions to supercritical flow at the crest, resulting in a hydraulic jump downstream. Reproduced from Durran (2015a).

Why is the shallow flow on the downstream side so fast? The answer lies in the shallow water momentum equation (Eq. 1.5), which can be integrated along a streamline to give the Bernoulli relation for this system. The result implies that the quantity

$$\frac{u^2}{2} + g\,(D + h) \tag{1.9}$$

is constant along a streamline. Therefore, as the height of the free surface $(D + h)$ decreases, the flow must accelerate.

This acceleration can be explained in a couple of different ways, but one helpful way is to explore it in terms of energy conversions. The second term in Eq. 1.9 represents both the gravitational potential energy and the potential energy due to pressure of the system. In the supercritical case, the increase of the free surface as the flow ascends the obstacle therefore represents a conversion from kinetic energy to potential energy, while the decrease of the free surface on the downstream side represents a conversion from potential energy back to kinetic energy. In the subcritical case, the situation is reversed, representing a conversion from potential energy to kinetic energy and back again. However, in the case relevant to downslope windstorms, the continuous decrease in the height of the free surface represents a continual conversion of potential energy into kinetic energy. This conversion is not reversed until the hydraulic jump restores the fluid to its upstream height.

Behavior resembling the above hydraulic jump scenario has been observed in systems more closely related to the real atmosphere. For example, simulations conducted by Durran (1986) with a layer of higher static stability topped by a layer of lower static stability indicate that hydraulic-jump-like behavior can form for certain configurations of the mountain height and interface height. However, the application of hydraulic theory to a continuously stratified fluid is not straightforward. In the case where there is a strong inversion at some height H, various authors have attemped to define a Froude number applicable to that atmosphere as $U/\sqrt{g'H}$, where $g' = g\Delta\theta/\theta_0$ is a "reduced gravity", $\Delta\theta$ is the potential temperature change across the inversion, and θ_0 is the mean potential temperature below the inversion. However, this does not generalize well in cases with shear or if the inversion is not strong enough. Even

in cases where such a parameter can be more easily defined, it does not typically result in quantitatively accurate results due to the dynamical differences between the shallow water system and the atmosphere.

One other proposed definition of a Froude number for the atmosphere is U/Nh, where N is the Brunt-Vaisala frequency and h is the maximum height of the mountain. Note, however, that unlike the shallow-water Froude number, where $\sqrt{gD}$ is the phase speed of a shallow water gravity wave, Nh is not the phase speed of any special wave in the atmosphere. However, the perturbation horizontal velocity u' does scale with Nh in the linear system, so this quantity (or rather its reciprocal, Nh/U) is often used as a measure of nonlinearity. In fact, Nh/U is a common choice for nondimensionalization of the mountain height.

1.2.3 Applicability of Theory to the Real Atmosphere

Unfortunately, despite the analogous behavior between hydraulic theory and real atmospheric flow, direct application of hydraulics to forecasting is difficult. Qualitative application is possible, however. Note that in supercritical shallow-water flow, the Froude number is greater than 1 (by definition). This implies that the flow velocity is greater than the phase speed of a shallow water gravity wave. No standing wave is therefore possible, since even the nominally upstream propagating wave will be carried downstream by the strong basic-state flow. On the other hand, subcritical flow supports modes which propagate upstream. Therefore, the phenomenon in the real atmosphere analogous to the transition from subcritical to supercritical flow in the shallow-water problem is a transition from wave-like motion over the windward side of the mountain to non-wave-like motion in the lee.

There are three recognized regimes under which this transition, and therefore strong downslope windstorms, can occur (Durran, 1990). These are 1) the presence of a strong stable layer at crest height with a region of lower stability aloft, 2) the presence of a wave of sufficient amplitude such that it breaks and self-induces a critical level, or 3) the presence of a critical-level in the mean state. Case 1 is probably the most directly analogous to shallow-water theory, as the stable layer acts somewhat analogously to a layer of shallow fluid. In

cases 2 and 3, the breaking region disrupts the wave motion such that the wave structure which decelerates parcels as they flow over the ridge is no longer present. This allows parcels flowing down the slope to attain strong wind perturbations.

The mechanism for the disruption of the wave in cases 2 and 3 is different. In case 2, it is the wave itself which attains such a strong amplitude that the isentropes become vertical, which leads to static instability and the wave breaking. This turbulent region then acts as a critical level for waves below (Peltier and Clark, 1979). In case 3, there is already a critical level present in the mean state background flow.

Clark and Peltier (1984) described a theory of downslope windstorms related to wave resonance from the wave reflection off of a low Richardson number critical level. This theory was based on linear dynamics, and as such, the results are independent of the mountain height. However, the conditions necessary for strong constructive interference occur only when the critical level is at specific heights

$$H_0 = \frac{(2n-1)\,\pi U}{2N},\ n = 1, 2, 3, \ldots. \tag{1.10}$$

Here, H_0 is the critical level height, U is the constant base-state wind below the critical level, and N is the static stability.

On the other hand, Smith (1985) advanced a theory based on finite-amplitude dynamics, taking advantage of the remarkable result that for atmospheres with constant wind and static stability, the finite-amplitude, nonlinear hydrostatic flow is described by the linear equation

$$\frac{\partial^2 \delta}{\partial z^2} + l^2 \delta = 0, \tag{1.11}$$

where $\delta(x, z) = z - z_0$, z_0 being the upstream height of the streamline through the point (x, z) (Long, 1953). The finite-amplitude lower boundary condition is given by

$$\delta\left[x, h(x)\right] = h(x), \tag{1.12}$$

where $h(x)$ is the terrain height. For the upper-boundary condition, Smith uses what is termed the "dividing streamline": the streamline immediately below a well-mixed turbulent

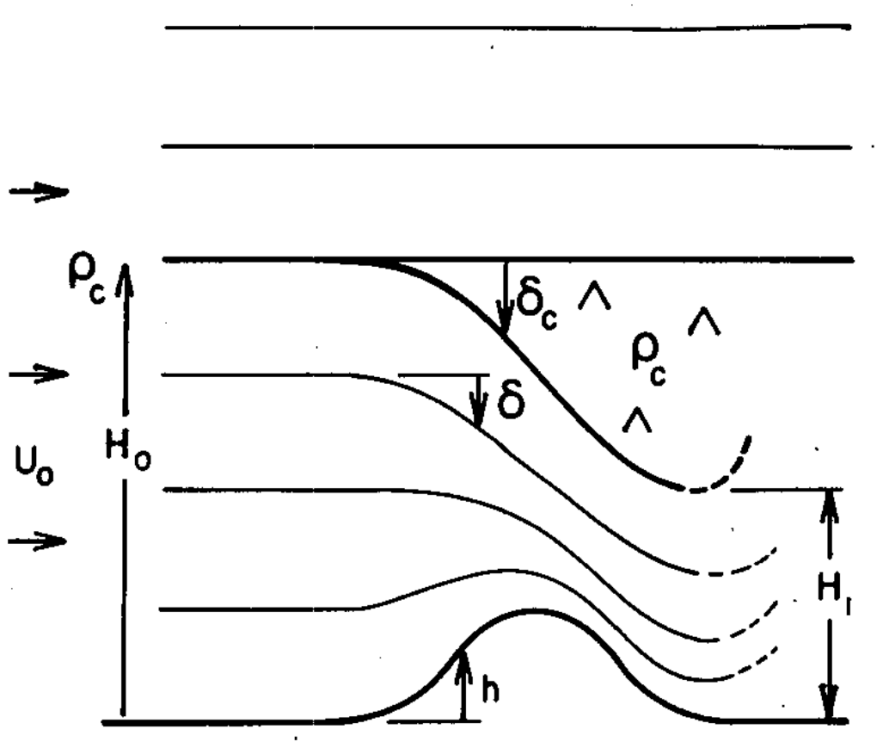

Figure 1.2: Schematic of the setup of the problem considered in Smith (1985). The upper boundary condition is the height of the dividing streamline, $H_0+\delta_c$, while the lower boundary condition is a function of the mountain height $h(x)$. The well-mixed region, denoted by carets, has a density ρ_c equal to that of the upstream density at the dividing streamline. Reproduced from Smith (1985).

region representing a critical level. A schematic of the setup of this problem is shown in Fig. 1.2. For specified upstream critical level heights and mountain heights, the boundary value problem can be solved to yield the height of the dividing streamline. These solution curves are shown in Fig. 1.3.

The solution curves have the following interpretation. The (nondimensional) mountain height is given on the x-axis. Each individual curve corresponds to a critical level height. In this figure, the solutions plotted correspond to critical level heights between 1/4 and 3/4 of a

hydrostatic vertical wavelength. For typical mountain profiles, the mountain height will first increase, reach the peak, and then decrease again (in an idealized sense, back to zero). For the critical level heights shown in this figure, as the mountain height increases, the height of the dividing streamline will at first decrease. If the mountain is high enough, eventually there will be a turning point in the curve for the height of the dividing streamline such that when the mountain height begins to decrease again, the dividing streamline continues to lower as the mountain height returns to zero, corresponding to a high-drag windstorm state. This turning point is analogous to the previously-described transition between subcritical and supercritical flow in shallow-water theory.

In contrast to the theory of Clark and Peltier (1984), Smith (1985)'s theory allows for the transition from subcritical to supercritical flow for a wide range of critical level heights. However, the results are such that the peak mountain height must correspond exactly to the turning point for the corresponding critical level height. If the peak mountain height is too low, the dividing streamline will simply return to its original upstream height as the mountain returns to zero. On the other hand, the theory does not provide for the case where the peak mountain height surpasses the turning point, as noted by Durran and Klemp (1987).

Bacmeister and Pierrehumbert (1988) conducted time-dependent simulations of downslope windstorms and found that the time-dependent solutions more closely match the theory of Smith (1985), rather than the linear theory of Clark and Peltier (1984). Furthermore, their results provided insight into the the behavior of systems for which the peak mountain height does not perfectly correspond to the turning point height. In the case where the true critical level height is below the height necessary to generate a windstorm by Smith (1985)'s idealization, an "upstream surge" develops in the time-dependent simulations. This surge alters the upstream wind speed and static stability, which results in a corresponding change in the nondimensional mountain height. This change brings the nondimensional mountain height to approximately that of the turning point height, and a high-drag state results. Note that this appears to indicate a relative insensitivity of the downslope windstorm response to the

precise height of the critical level, as long is the critical level height is originally below that required for the high-drag response.

Mean-state critical levels, and therefore case 3 windstorms, are prevalent on the west side of major mountain ranges in the midlatitudes. For example, they occur along the Wasatch Front of Utah (e.g. Lawson and Horel, 2015a,b), and are also one cause of strong Santa Ana winds in California (e.g. Cao and Fovell, 2015, 2018). This particular windstorm generation mechanism is special in a sense because, unlike either case 1 or 2 windstorms, the Bacmeister and Pierrehumbert (1988) results indicate a relative insensitivity to the height of the critical level.

1.2.4 Predictability

In his seminal work on predictability, Lorenz (1969) used an idealized turbulence model and argued that the predictability horizon, the time after which the state of the system cannot be well-predicted from the initial conditions, was extremely limited for mesoscale motions due to the rapid upscale propagation of initial condition errors. However, Anthes et al. (1985) argued that for mesoscale phenomena either strongly coupled to large-scale flow or externally forced through well known features such as topography, the predictability may be much greater than that expected given the results of Lorenz. On the other hand, subsequent work such as that of Durran and Gingrich (2014) and Weyn and Durran (2017) indicate that small relative errors on the synoptic scale can cascade rapidly downscale and destroy predictability at the smallest scales in the same manner as if the errors had simply originated at smaller scales. In a mountain meteorology context, Nuss and Miller (2001) found that the mesoscale flow and resulting precipitation were quite sensitive to small changes in the flow relative to the topography.

These results combined seem to lead to a quite pessimistic outlook on mesoscale predictability. However, although the hypothesis of Anthes et al. (1985) certainly requires modification, perhaps it still has some merit if the mesoscale response is coupled but yet suitably insensitive to precise details of the large-scale flow. The combination of known ex-

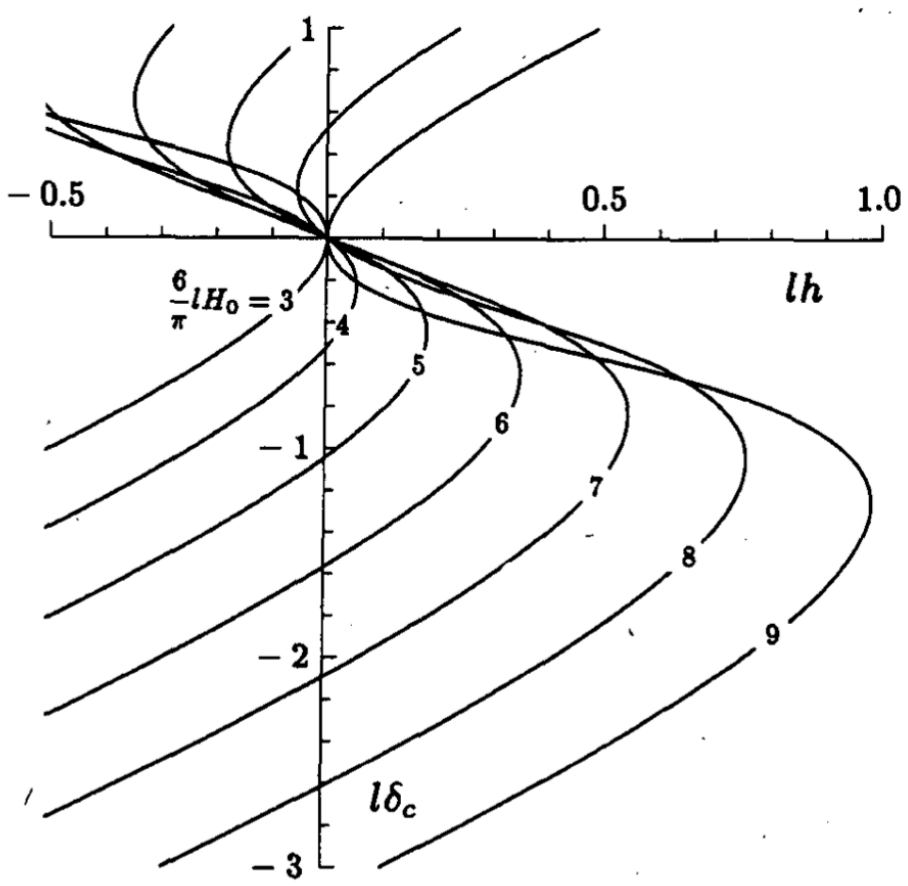

Figure 1.3: Solution curves from Smith (1985), as adapted by Durran and Klemp (1987). The x-axis is a nondimensionalized mountain height, where $l \equiv N/U$ is the Scorer parameter. Similarly, the y-axis is a nondimensionalized streamline displacement. Solution curves are plotted for varying values of the upstream dividing streamline height H_0, nondimensionalized such that the numeric values correspond to multiples of 1/12 of a hydrostatic vertical wavelength $2\pi/l$. Symbols h, δ_c, and H_0 are defined and visualized in Fig. 1.2. (Reproduced from Durran and Klemp (1987).)

ternal forcing due to the topography, in conjunction with an apparent adjustment process leading to severe downslope flow, at least for certain downslope windstorm regimes, may lead to enhanced predictability.

Unfortunately, previous studies of the predictability of downslope windstorms have returned mixed results. Theoretical studies using ensemble methods and adjoint analyses have found limited predictive skill, often on time scales as short as 12 hours (Doyle et al., 2007; Doyle and Reynolds, 2008; Reinecke and Durran, 2009). On the other hand, colloquial evidence from forecasters, as well as some case studies, have seemed to exhibit extended predictability. For example, one study of a downslope event on the Wasatch Front of Utah on 1 December 2011 found extended predictability of up to two days in advance (Lawson and Horel, 2015b).

One crucial difference between the windstorms analyzed by Reinecke and Durran (2009) and Lawson and Horel (2015b) is that the Owens Valley of California, the site of the Reinecke and Durran (2009) study, is located on the eastern side of a mountain range, while the areas studied along the Wasatch Front are along the western side. This, combined with the apparent relative insensitivity of high-drag responses to the exact height of the mean-state critical-level, leads to the hypothesis that downslope windstorms occurring in environments with mean-state critical levels may be more predictable than those occurring in the other two regimes. Nance and Colman (2000), testing a deterministic two-dimensional model, found that predictions of windstorms without mean-state critical levels tended to be severely overpredicted, but windstorms occurring in the presence of a mean-state critical-level exhibited a distribution of model wind speed error (defined as the observed wind speed minus the model forecast wind speed) centered and peaking at 0.

The Nance and Colman (2000) result hints at enhanced predictability in the presence of a mean-state critical level, but their analysis was not conducted using ensemble methods. The predictability of mean-state critical-level windstorms has not been extensively explored using both ensembles and observations. While one of the cases considered in Doyle and Reynolds (2008) included a mean-state critical level and resulted in no corresponding increase

in predictability, this question has not been previously analyzed with a larger sample size and in conjunction with actual observations. Our investigation of this hypothesis is the topic of Chapter 3.

1.3 Dissertation Organization

The remainder of this dissertation is organized as follows. Chapter 2 contains our analysis of finite-amplitude mountain waves and was previously published as Metz and Durran (2021). Chapter 3 contains our analysis of the predictability of downslope windstorms in the mean-state critical level regime. Chapter 4 contains overall conclusions and concluding remarks.

Chapter 2

FINITE-AMPLITUDE EFFECTS ON NON-BREAKING MOUNTAIN WAVES

2.1 Introduction and Background

Linear theory has been applied to the study of mountain waves for decades, including some of the earliest works on the subject (Queney, 1948; Scorer, 1949) and some of the latest analysis of observational data (Smith and Kruse, 2017). The relationship derived by Eliassen and Palm (1960) between vertical energy and momentum fluxes for steady nondissipating mountain waves has been verified using observations from recent field campaigns (Smith et al., 2008, 2016). Wentzel-Kramers-Brillouin (WKB) ray-tracing has been successfully used to explain gravity propagation into the middle atmosphere (Marks and Eckermann, 1995; Guest et al., 2000). There is, therefore, considerable evidence that linear theory provides a reasonably good approximation to the dynamics governing gravity-wave propagation through much of the atmosphere.

Partly for this reason, as well as for simplicity and to minimize computational cost, linear theory is widely used in the parameterization of orographic gravity wave drag (GWD) in both numerical weather prediction (NWP) and general circulation models (GCMs). In particular, the estimate of the low-level mountain-wave momentum flux typically uses the functional dependence on the near-surface wind U_s, static stability N_s, and the unblocked mountain height $h_{\rm ub}$ given by linear-theory: $N_s U_s h_{\rm ub}^2$. Farther aloft, the changes in wave amplitude and the level of wave breaking are parameterized using the WKB assumption (e.g. Palmer et al., 1986; McFarlane, 1987; Kim and Arakawa, 1995; Kim et al., 2003; Kim and Doyle, 2005). While improvements to orographic GWD parameterizations have been made to include low-level flow blocking (e.g. Lott and Miller, 1997; Kim and Doyle, 2005)

and mountain anisotropy (e.g. Scinocca and McFarlane, 2000; Kim and Doyle, 2005; Choi and Hong, 2015), major global modelling centres such as the U.S. National Centers for Environmental Prediction (NCEP; Chen et al., 2019; Zhou et al., 2019), the European Centre for Medium-Range Weather Forecasts (ECMWF; Sandu et al., 2016; ECMWF, 2020), and the UK Met Office (Walters et al., 2017) continue to estimate the momentum flux in the waves launched by the mountain as proportional to $N_s U_s h_{\mathrm{ub}}^2$.

Nevertheless, nonlinear processes can be important in setting the amplitude at which mountain waves are generated, but the importance of nonlinearity in regulating wave amplitude is poorly understood, perhaps because so much theoretical attention as been devoted to the special case in which the upstream environmental Brunt-Väisälä frequency $N(z)$ and the cross-mountain wind speed $U(z)$ are constant with height. When N and U are constant, the streamline displacement $\delta(x, z)$ in steady two-dimensional Boussinesq flow over such a ridge is governed by Long's equation (Long, 1953),

$$\left(\frac{\partial^2}{\partial x^2} + \frac{\partial^2}{\partial z^2}\right)\delta + \frac{N^2}{U^2}\delta = 0. \tag{2.1}$$

Here x is the horizontal coordinate perpendicular to the ridge-line; z is the vertical coordinate.

Although Long's equation is a linear partial differential equation, it may be derived from the fully nonlinear equations without making any small-amplitude assumptions. Nevertheless, if U is constant, Eq. 2.1 may also be derived by assuming the mountain is infinitesimally high and linearizing the governing equations in the usual manner. When N and U are constant, the only difference between the linear and nonlinear solutions arises from the lower boundary condition. Letting $h(x)$ be the height of the topography, the lower boundary condition requires $\delta\left[x, h(x)\right] = h(x)$ in the exact finite-amplitude case and is approximated by $\delta(x, 0) = h(x)$ in the small-amplitude limit.

As one might guess from the similarities in the governing equations for linear and finite-amplitude perturbations, when N and U are constant the influence of nonlinear dynamics on the wave structure is often relatively minor. This similarity can be appreciated by comparing

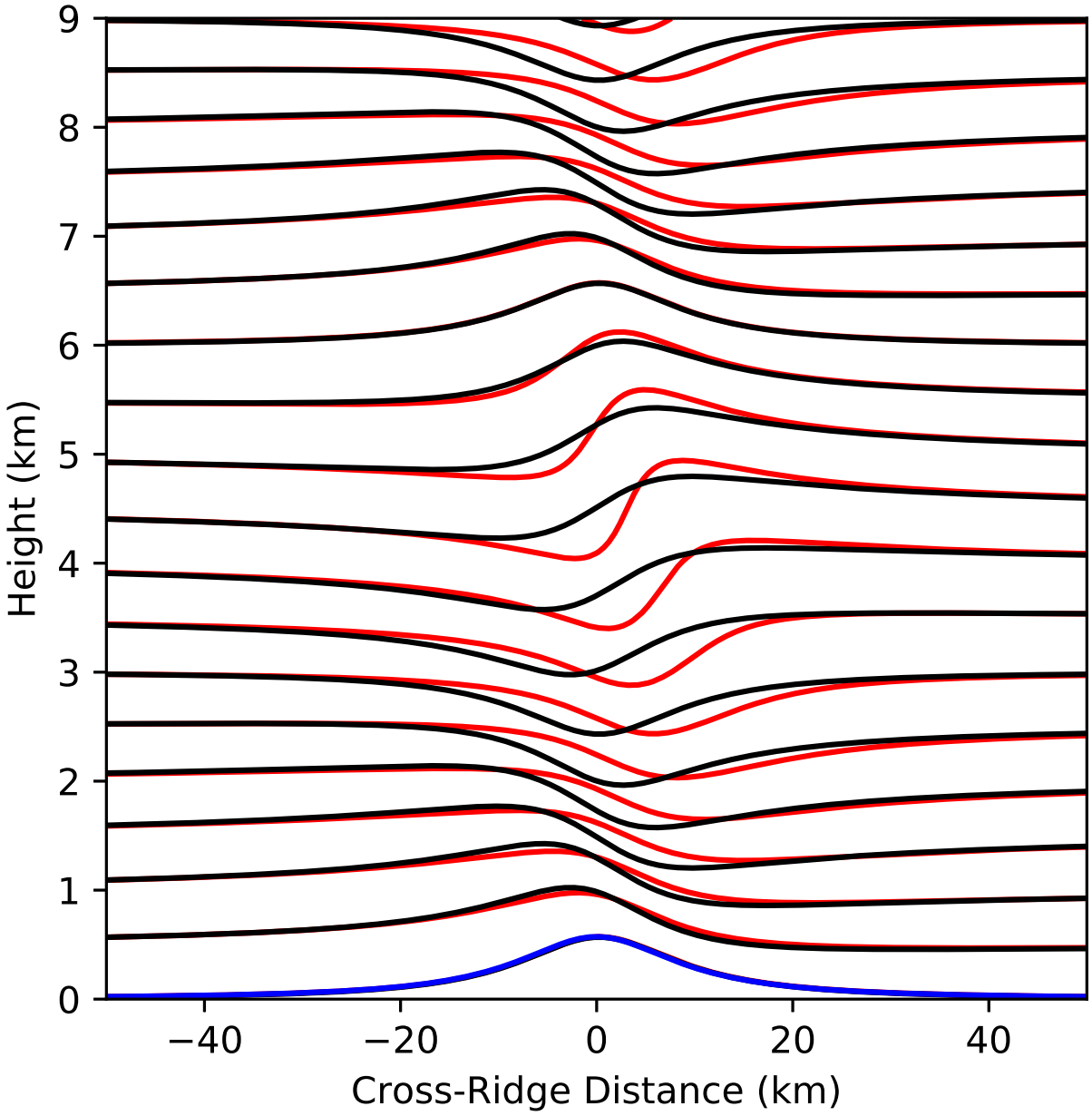

Figure 2.1: Comparison of streamlines of the one-layer linear (black) and nonlinear (red) solutions for a Witch of Agnesi mountain with $a = 10\,\text{km}$ and $Nh_m/U = 0.6$. Airflow is left to right; the mountain profile is shown in blue.

the linear and nonlinear solutions[1] in Fig. 2.1, which is for a case with $N = 0.01\,\mathrm{s}^{-1}$, $U = 10\,\mathrm{m/s}$, and $Nh_m/U = 0.6$, where h_m is the mountain height. Nonlinear processes steepen the streamlines above the mountain around $z = 4.5\,\mathrm{km}$, which is 3/4 of a hydrostatic vertical wavelength ($2\pi U/N$) above the topography. Despite the modest differences in the shape of the streamlines between the linear and nonlinear waves, the wave amplitude is almost identical in both cases. Hence, nonlinear processes do not have a dramatic impact on the mountain-wave momentum flux generated in constant-N-and-U flow over a ridge unless the ridge is high enough to force wave overturning.

In contrast to the constant-N idealization, there is typically a factor of two change in static stability between the troposphere and the lower stratosphere, and changes in the height of a sharp tropopause can strongly modulate the strength of momentum fluxes associated with vertically propagating hydrostatic mountain waves. If there is a factor of two difference in N across the tropopause and U is the same constant value in both layers, the ratio of the momentum fluxes in the optimally tuned case to the maximally detuned case is a factor of four in linear mountain waves (Blumen, 1965; Klemp and Lilly, 1975). The wave reflections at the tropopause responsible for this variation in momentum fluxes are not captured in a WKB framework, as they are neglected by the fundamental WKB assumption of a slowly-varying mean state. Laprise (1993) examined the appropriateness of applying the WKB approximation to linear wave propagation. He found that while the WKB approximation often provided a good estimate of the onset of linear steady-state wave breaking (i.e. where $Nh/U = 1.0$), it often under- or over-estimated the drag significantly compared to a linear steady-state column model. Furthermore, as shown in the semi-analytic analysis in Durran (1992, their Fig. 7), even such linear calculations for complex atmospheric profiles as in Laprise (1993)'s steady-state column model may themselves dramatically over- or under-estimate the momentum fluxes in finite-amplitude non-breaking waves.

The results of Blumen (1965) and Klemp and Lilly (1975) assume discontinuous jumps

[1]There are two ways to display streamlines for a mountain-wave linear solution; their differences and our approach are discussed in Appendix 2.B.

in static stability. As noted by Blumen (1985) and others, the partial reflection of vertically propagating waves at the tropopause decreases as the thickness of the tropopause transition layer is increased. Teixeira and Argaín (2020) related the decrease in reflection coefficient to the surface pressure drag, and as might be expected, the variation in pressure drag is smaller for larger tropopause thicknesses.

Nevertheless, evidence suggests a discontinuity may often be the best approximation for the tropopause. Birner (2006) constructed a climatology of the fine-scale structure of the tropopause and found that the transition between tropospheric and stratospheric values of static stability is often quite sharp and essentially discontinuous. While a simple discontinuity in static stability can therefore serve as a prototypical model for the tropopause, it is still useful to examine how a smoother tropopause impacts the solution. Teixeira and Argaín (2020) did conduct a preliminary analysis of nonlinear effects on their smooth tropopause solutions, but many of their cases (when dimensionalized with realistic values) result in quite broad tropopause transition layers. In this paper we will extend the investigation in Teixeira and Argaín (2020) to consider thinner and more realistic tropopause transition layers.

Significant vertical variations in $U(z)$ are common during most real-world mountain wave events. Defining the square of the Scorer parameter as

$$l^2 = \frac{N^2}{U^2} - \frac{1}{U}\frac{d^2U}{dz^2}, \tag{2.2}$$

the linear, two-dimensional, steady-state Boussinesq wave equation in the presence of vertical wind shear is

$$\left(\frac{\partial^2}{\partial x^2} + \frac{\partial^2}{\partial z^2}\right) w + l^2 w = 0, \tag{2.3}$$

where w is the vertical velocity. In contrast to the case with constant U and Eq. 2.1, the nonlinear governing equations cannot be expressed in a form similar to Eq. 2.3, suggesting that nonlinear effects could be more significant in the presence of shear. While nonlinear effects in the presence of shear have been examined previously by Wells and Vosper (2010), we investigated stronger finite-amplitude effects by simulating higher mountains than the 10 m high ridges considered in their paper.

Since the numerical method used in Durran (1992) was based on two-layer solutions of Long's equation, it is unable to incorporate smooth vertical variations of static stability, which is needed to explore a smooth transition region at the tropopause. It is also unable to incorporate wind shear. To overcome these limitations, we employed a different methodology by linearizing a time-dependent numerical model and comparing its simulations with those of its nonlinear counterpart. This approach allowed us to investigate a much larger space of background profiles than was possible in previous studies.

The rest of the chapter proceeds as follows. The linearization of the model and its configuration are described in Section 2.2. The environmental conditions for the various numerical experiments are described in Section 2.3. We analyse the results of our simulations in Section 2.4, and provide further perspective on the way that finite-amplitude effects impact the flow in Section 2.5. Section 2.6 contains our conclusions.

2.2 Model Description

Our nonlinear simulations are performed with the University of Washington meso12 model (Durran and Klemp, 1983) running in a Boussinesq configuration. By neglecting the decrease in mean density with height, the Boussinesq assumption reduces the chance of stratospheric wave breaking in our simulations. This model also serves as the basis for our linearized version. For simplicity in implementing the linearization, we utilize leapfrog time differencing with a Robert-Asselin time filter and fourth order advection in both the linear and nonlinear models.

2.2.1 Linearization

For the model to be fully linear, three components must be linearized: the advection terms, the lateral boundary conditions, and the lower boundary condition. The radiation upper boundary condition is already linear (Durran, 2010) and requires no modification. For the basic state, we specify vertically varying but horizontally homogeneous profiles of potential temperature $\bar{\theta}(z)$ and horizontal wind speed $\bar{u}(z)$. The base-state vertical velocity $\bar{w}(z)$ is

taken to be identically zero.

In the linear configuration, the coordinate surfaces are flat, and no terrain-following coordinate transformation is required. Letting overbars denote the vertically-varying basic state and primes the perturbations, the advection terms are simply linearized as

$$u_i \frac{\partial s_j}{\partial x_i} = \bar{u}_i \frac{\partial s'_j}{\partial x_i} + u'_i \frac{\partial \bar{s}_j}{\partial x_i} \tag{2.4}$$

where $(u_1, u_2) = (u, w)$, $(x_1, x_2) = (x, z)$, and $(s_1, s_2, s_3) = (u, w, \theta)$. The outflow boundary conditions are that of Klemp and Wilhelmson (1978), but with a linearized advection term. For example, at the left boundary, their Equation 2.27,

$$\frac{\partial u}{\partial t} + (u + c^*) \frac{\partial u}{\partial x} = 0, \tag{2.5}$$

becomes

$$\frac{\partial u'}{\partial t} + (\bar{u} + c^*) \frac{\partial u'}{\partial x} = 0. \tag{2.6}$$

Here c^* is a prescribed outflow phase speed. Waves with this phase speed approaching the boundary are perfectly transmitted through the boundary, while all others are imperfectly transmitted (Durran, 2010).

2.2.2 Model Configuration

Our simulations are conducted in two dimensions (x, z) to explore a larger parameter space and also to compare with the two-dimensional two-layer semi-analytic solutions of Durran (1992). However, in contrast to Durran (1992), which used a Witch of Agnesi profile given by

$$h(x) = \frac{h_m a^2}{(x - x_0)^2 + a^2}, \tag{2.7}$$

where h_m is the mountain crest height, a is the half-width, and x_0 is the centre of the mountain, the terrain profile in our simulations is a $\cos^4$ mountain given by

$$h(x) = \begin{cases} \frac{h_m}{16} \left[1 + \cos\left(\frac{\pi(x - x_0)}{4a}\right)\right]^4, & \left|\frac{(x-x_0)}{4a}\right| < 1 \\ 0, & \left|\frac{(x-x_0)}{4a}\right| \geq 1. \end{cases} \tag{2.8}$$

A comparison between the $\cos^4$ mountain and the Witch of Agnesi mountain with the same crest height and half-width is shown in Fig. 2.2. The $\cos^4$ mountain has the advantage that the mountain height drops to zero at a finite distance from the crest. Because of this, all contributions to the surface pressure drag are confined to a small neighbourhood in the centre of the domain. In a constant N and U environment, the linear pressure drag across the $\cos^4$ mountain exceeds that across a Witch of Agnesi with same values of h_m and a by a factor of 1.3. This factor was evaluated numerically from the linear analytic solution using Fourier transforms and confirmed with the time-dependent linearized meso12 model.

For our simulations, the model was run with a horizontal resolution of $\Delta x = 500$ m and a vertical resolution of $\Delta z = 50$ m. The domain was $L_x = 600$ km wide and 30 km tall; the large time step, which is used to integrate all terms not involved in the generation of acoustic modes, was 2 s, and the small time step, used for acoustic modes, was 2/3 s. The Robert-Asselin filter coefficient was set to 0.1. The terrain height was varied between simulations, but the terrain width was specified using a constant $a = 20$ km. The mountain was placed in the centre of the domain at $x_0 = 300$ km in all simulations. The outflow phase speed at the lateral boundaries was specified as $c^* = 35$ m/s at the upstream boundary and $c^* = 15$ m/s at the downstream boundary. These values were chosen to ensure that modes are directed out of the computational domain with appropriate Doppler-shifted phase speeds at both lateral boundaries. The upper boundary used the radiation condition specified in Durran (2010, p. 484), with perfect upward transmission specified for horizontal wavelengths of 18, 72, and 144 km. Although the model is inviscid, it incorporates scale-selective fourth-derivative dissipation as well as a sub-grid-scale mixing parameterization. This parameterization was active for the nonlinear simulations but inactive for the linear simulations. The background wind field was ramped up from zero to its full value over a period of 4000 s. The model was run to a nondimensional time $U_0 t/a = 43.6$, where U_0 is the surface wind speed, which was long enough for all non-breaking cases to achieve an approximate steady state.

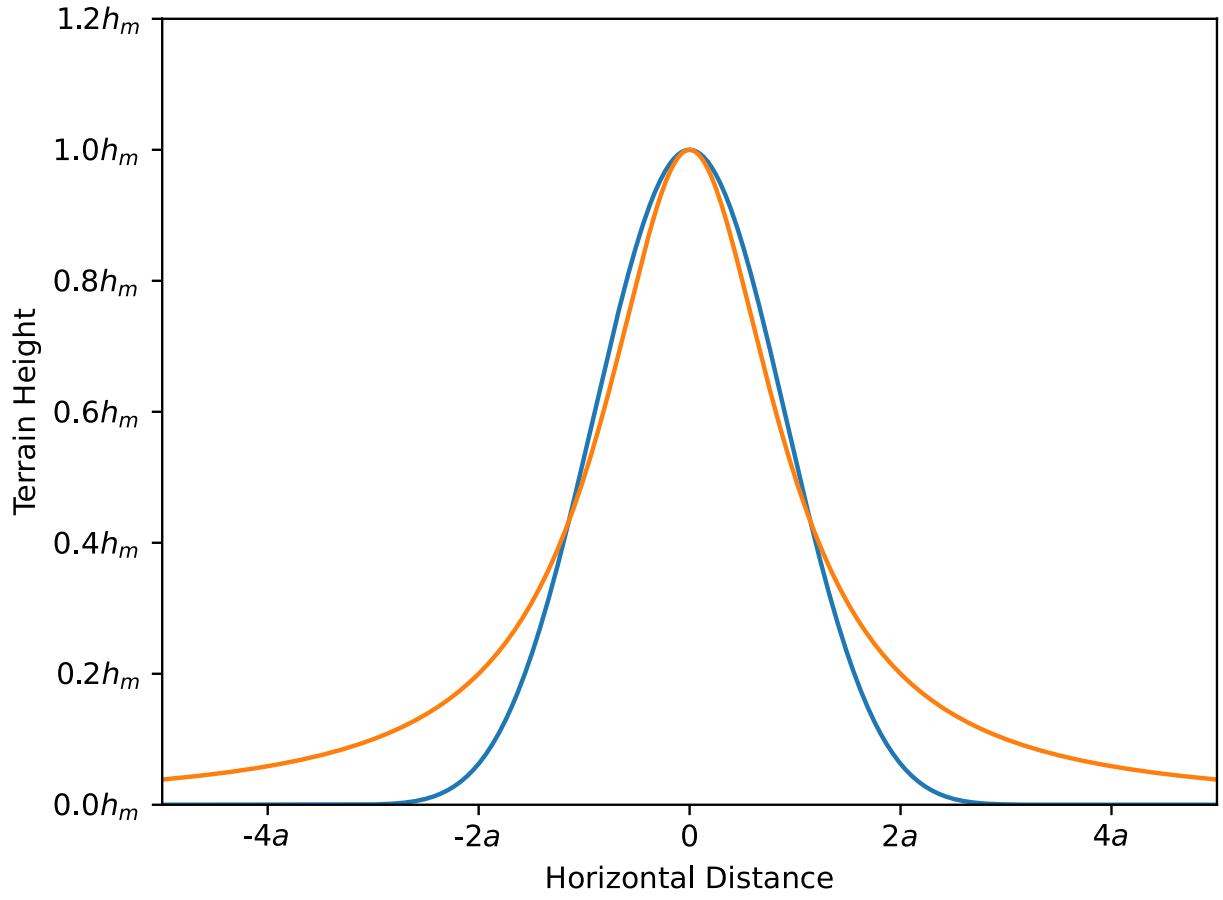

Figure 2.2: Comparison of a $\cos^4$ (blue) and a Witch of Agnesi (orange) profile with the same values of h_m and a.

2.3 Upstream Environments

Four families of numerical experiments with differing upstream soundings were conducted in which the heights of the mountain and the tropopause were systematically varied. In the first pair of experiments, where the upstream wind speed is constant with height, the tropopause height varied between $0.3\lambda_L$ and $0.8\lambda_L$ at increments of $0.05\lambda_L$, where $\lambda_L = 2\pi U/N_L$ is the vertical wavelength of a hydrostatic mountain wave in the lower layer (i.e., the troposphere). In the remaining experiments the height of the tropopause varied between 5 km and 15 km in 500 m increments. The mountain height h_m was varied between 100 m and 1000 m in 100 m increments in all experiments. For the first pair of experiments, this corresponds to nondimensional mountain heights $\tilde{h}_m$ from 0.1 to 1.0 with increments of 0.1.

2.3.1 Experiment 1: Sharp Tropopause, No Wind Shear

The upper-layer (the stratosphere) has a static stability of $N_U = 0.02$ s^{-1}, while the lower layer (the troposphere) has a static stability of $N_L = 0.01$ s^{-1}. The wind speed is constant throughout at $U = 20$ m/s.

2.3.2 Experiment 2: Gradual Transition at Tropopause

The static stability profile is the same as in the two-layer soundings, except for the presence of a linear transition in N over a depth Δz. For a tropopause height z_T, the static stability profile is given by

$$N(z) = \begin{cases} N_L, & 0 < z < z_T - \frac{\Delta z}{2} \\ N_U, & z > z_T + \frac{\Delta z}{2} \\ \frac{N_L + N_U}{2} + \frac{(N_U - N_L)(z - z_T)}{\Delta z}, & \text{otherwise} \end{cases} \tag{2.9}$$

Two values of Δz were considered, $\Delta z = 1\,\text{km}$ and $\Delta z = 2\,\text{km}$. For our values of static stability and wind speed, these correspond to normalized transition layer depths of $0.08\lambda_L$ and $0.16\lambda_L$, respectively.

2.3.3 Experiment 3: Sharp Tropopause, 10-30 m/s Shear

The profiles of $U(z)$ are representative of the mid-latitude westerlies, and the static-stability profile is identical to the two-layer structure in Experiment 1. The wind speed increases from 10 m/s at the surface to 30 m/s at the tropopause and drops back to a value of 20 m/s in the stratosphere. An example Experiment-3 profile is shown in Fig. 2.3 for a case with the tropopause at $z_T = 10$ km. The procedure used to generate $U(z)$ is presented in Appendix 2.A.

2.3.4 Experiment 4: Sharp Tropopause, 10-50 m/s Shear

The Experiment-4 soundings are identical to those of Experiment 3, except that the wind speed increases from 10 m/s to 50 m/s in the troposphere. The mid- to upper-stratospheric wind speed remains specified as a constant 20 m/s.

2.4 Results

2.4.1 Experiment 1: Sharp Tropopause, No Wind Shear

The Experiment-1 soundings admit analytic linear hydrostatic steady-state solutions in wavenumber space, which can be easily transformed to physical space by an inverse Fourier transform. Letting l_L and l_U denote the constant Scorer parameter values below and above the tropopause, the Fourier-transformed vertical velocity field for wavenumber k, $\hat{w}(k, z)$, is given by

$$\hat{w}(k,z) = \begin{cases} a_1 \cos\left[l_L z\right] + b_1 \sin\left[l_L z\right] & 0 < z < z_T \\ a_2 \cos\left[l_U \left(z - z_T\right)\right] + b_2 \sin\left[l_U \left(z - z_T\right)\right] & z > z_T, \end{cases} \tag{2.10}$$

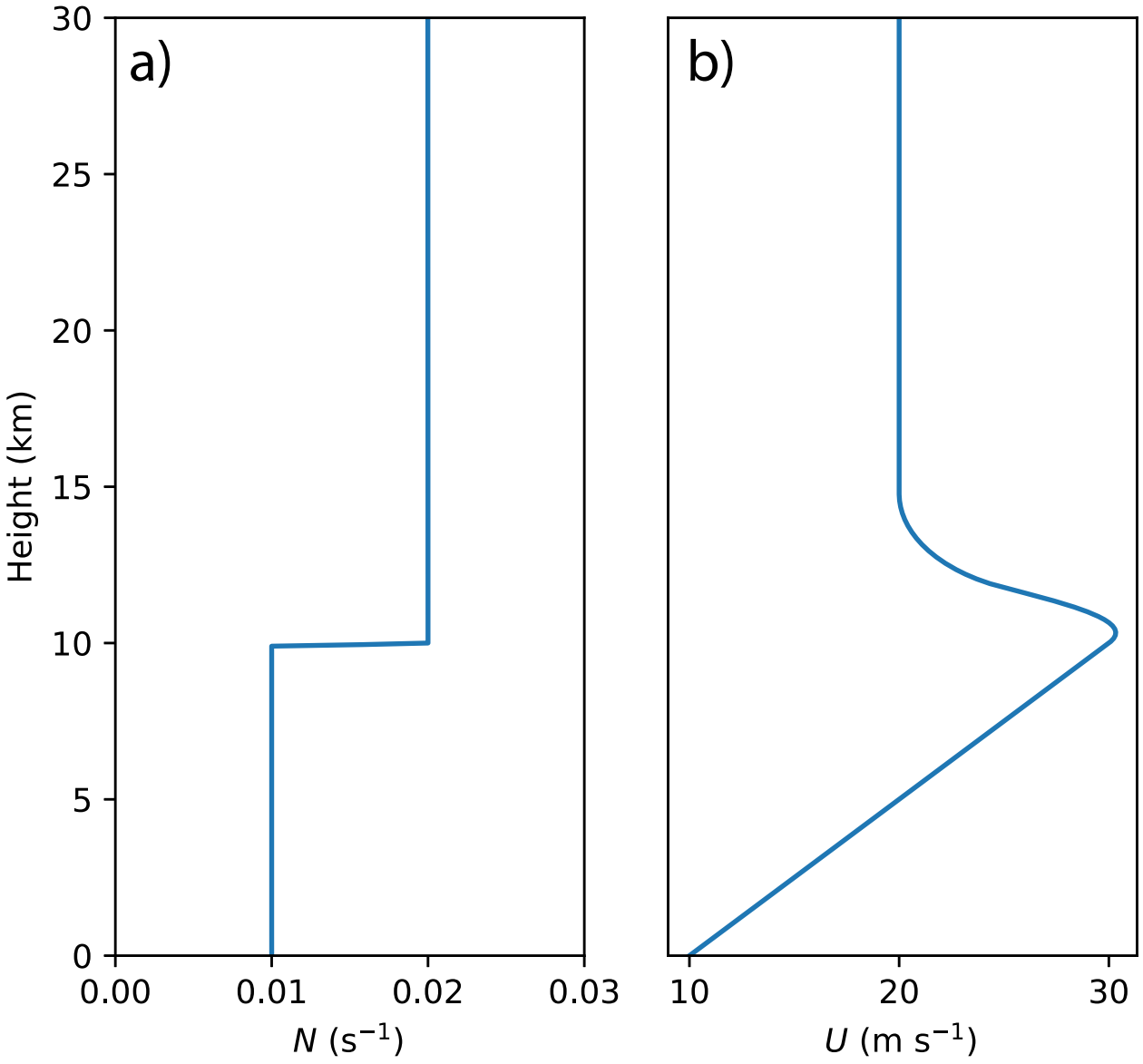

Figure 2.3: Vertical profiles of (a) Brunt-Väisälä frequency N and (b) horizontal wind speed U for an Experiment-3 case with the tropopause height set at 10 km.

where

$$a_1 = Uik\hat{h}, \tag{2.11}$$

$$b_1 = -\frac{\sin\left(l_L z_T\right) l_L\beta + \cos\left(l_L z_T\right) l_U}{\sin\left(l_L z_T\right) l_U - \cos\left(l_L z_T\right) l_L\beta} a_1 \tag{2.12}$$

$$a_2 = a_1 \cos\left(l_L z_T\right) + b_1 \sin\left(l_L z_T\right), \tag{2.13}$$

$$b_2 = a_2/\beta \tag{2.14}$$

$$\beta = \begin{cases} i, & k < 0 \\ -i, & k \geq 0 \end{cases} \tag{2.15}$$

Here $\hat{h}(k)$ is the Fourier transform of the mountain profile $h(x)$. This is a simplification of the three-layer solution of Klemp and Lilly (1975).

Using the polarization relation

$$\hat{p}(k,z) = -\frac{i\rho_0 U}{k}\frac{\partial\hat{w}}{\partial z} \tag{2.16}$$

to derive the perturbation pressure $p'(x,z)$ from Eq. 2.10, the normalized cross-mountain pressure drag

$$\tilde{D}_l = \frac{4}{\pi\rho_0 N_L U h_m^2}\int_0^{L_x} p'\left(x,0\right)\frac{\partial h}{\partial x}\,dx. \tag{2.17}$$

is plotted in Fig. 2.4 for the $\cos^4$ mountain as a function of the tropopause height nondimensionalized by the vertical wavelength of a hydrostatic mountain wave in the troposphere such that $\tilde{z}_T = N_L z_T/(2\pi U)$. These analytic results may be compared to the drag obtained from a series of linearized meso12 simulations in which p' is replaced in Eq. 2.17 by the steady-state surface pressure from the numerical simulations (orange points in Fig. 2.4). Although the linearized meso12 model is nonhydrostatic, we compare directly to the hydrostatic analytic solution because the mountain is wide enough that the response is largely hydrostatic ($a = 20\,\text{km}$, implying $N_L a/U = 10$ and $N_U a/U = 20$). The pressure drags obtained from linearized meso12 simulations are in close agreement with the analytic solution, thereby providing a check on the correctness of our linearized time-dependent numerical model.

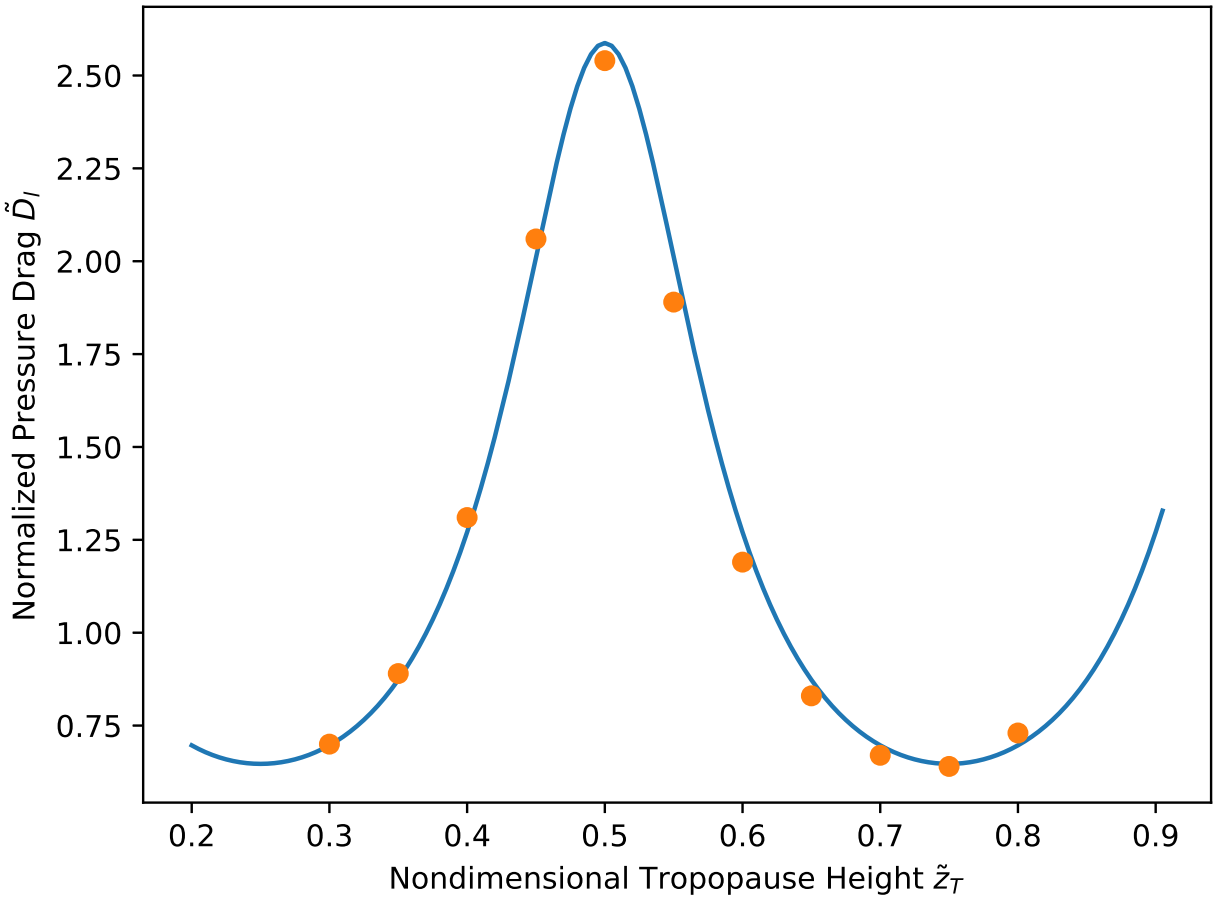

Figure 2.4: Cross-mountain pressure drag $\tilde{D}_l$ as a function of nondimensional tropopause height $\tilde{z}_T$ for Experiment 1 computed by the semi-analytic method (blue line) and using the linearized meso12 model run to steady state (orange points).

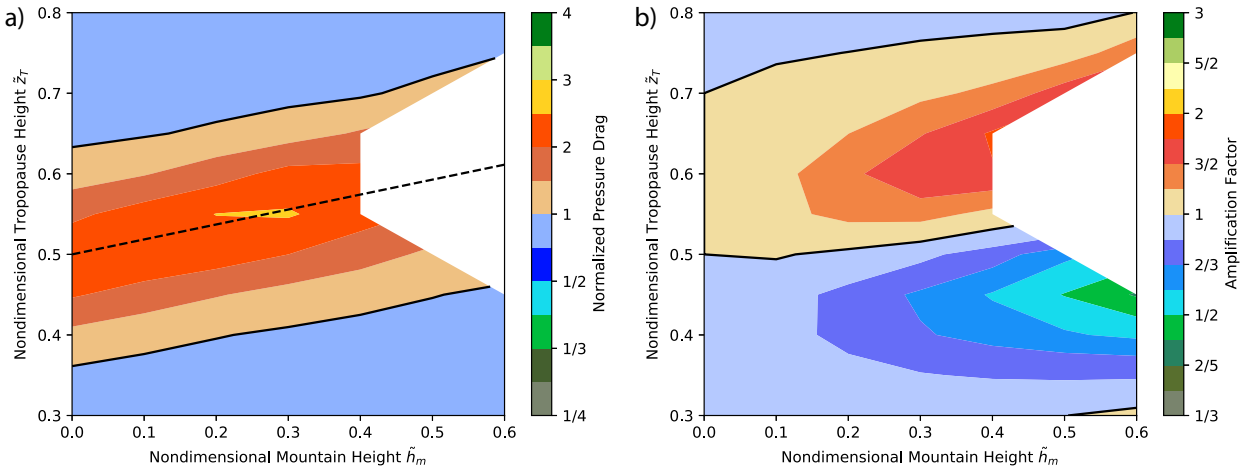

Figure 2.5: (a) Normalized cross-mountain pressure drag $\tilde{D}_{nl}$ for the Experiment-1 simulations contoured as a function of nondimensional mountain and tropopause heights, and (b) Amplification of the nonlinear drag relative to that for the corresponding linear solution. The linear solution is plotted at a mountain height of 0.0. The thick black line indicates a normalized pressure drag or amplification of 1.0. White areas are plotted for those values of $\tilde{h}_m$ and $\tilde{z}_T$ that produce breaking mountain waves. The black dashed line, satisfying $\tilde{z}_T = 1.17\tilde{h}_m + 0.5$, is an empirical fix to the set of $(\tilde{h}_m, \tilde{z}_T)$ along which $\tilde{D}_{nl}$ is maximized and is discussed in connection with Fig. 2.13.

The deviations from the linear uniform-atmosphere pressure drag for the finite-amplitude case are shown in Fig. 2.5a, in which the normalized drag is contoured as a function of the nondimensional mountain height $\tilde{h}_m = N_L h_m/U$ and $\tilde{z}_T$. Letting $p(x,z)$ be the pressure computed with the nonlinear model at quasi-steady state, the normalized nonlinear pressure drag is

$$\tilde{D}_{nl} = \frac{4}{\pi\rho_0 N_L U h_m^2} \int_0^{L_x} p\,[x, h(x), t]\, \frac{\partial h}{\partial x}\, dx, \tag{2.18}$$

We define the quasi-steady-state pressure as that occurring at the midpoint of the first interval of duration $\Delta(Ut/a) = 5$ after nondimensional time $Ut/a = 20$ in which the drag varies by less than 5% of the average value within the interval. Note that the normalization factor $\pi\rho_0 N_L U h_m^2/4$ is the drag that would be obtained from many GWD parameterizations, namely the drag generated by linear mountain waves launched by a Witch of Agnesi mountain in an atmosphere with uniform basic-state wind U and static stability N_L. No drag values are plotted in Fig. 2.5 for those combinations of h_m and z_T that do not achieve quasi-steady state. Breaking waves do not achieve quasi-steady state, and therefore our analysis is restricted to non-breaking waves.

As is well known (Klemp and Lilly, 1975) and evident in Fig. 2.4, in the limit of small $\tilde{h}_m$ the pressure drag is maximized at $\tilde{z}_T = 0.5$. Fig. 2.5a shows that, as $\tilde{h}_m$ increases, the maximum $\tilde{D}_{nl}$ occurs at progressively higher tropopause heights, a behaviour consistent with Durran (1992).[2] For $0.15 \leq \tilde{h}_m \leq 0.35$, the maximum values of $\tilde{D}_{nl}$ exceed 2.5, suggesting that use of typical GWD expressions for the drag and momentum flux could be in error by that same factor.

The normalization factor in (2.18) is for a single-layer atmosphere, not the corresponding linear two-layer problem. Therefore, to isolate the effects of finite amplitude, $\tilde{D}_{nl}/\tilde{D}_l$ is contoured as a function of $\tilde{h}_m$ and $\tilde{z}_T$ in Fig. 2.5b. Use of the ratio $\tilde{D}_{nl}/\tilde{D}_l$ also removes the factor of roughly 1.3 by which the drag over the $\cos^4$ mountain exceeds that for the reference Witch-of-Agnesi mountain. Linear theory closely approximates the 0.65 to 2.56

[2]In fact, all of our computed pressure drags are within 3% of those in Durran (1992) once they are adjusted to account for the $\cos^4$ shape of our topography.

range over which the nonlinear pressure drag varies as the tropopause height changes, but the functional dependence on the tropopause height is different in the nonlinear case. Due to the shift of the maximum $\tilde{D}_{nl}$ to increasing tropopause heights as the $\tilde{h}_m$ increases, an amplification-deamplification couplet is present in the field of $\tilde{D}_{nl}/\tilde{D}_l$. For values of $\tilde{z}_T$ above 0.5, $\tilde{D}_{nl}/\tilde{D}_l$ increases with increasing mountain height to its maximum when $(\tilde{h}_m, \tilde{z}_T) = (0.4, 0.65)$, while for $\tilde{z}_T < 0.5$ it decreases as $\tilde{h}_m$ increases, reaching its minimum when $(\tilde{h}_m, \tilde{z}_T) = (0.6, 0.45)$.

A case with strong finite-amplitude amplification ($\tilde{h}_m = 0.3$, $\tilde{z}_T = 0.55$) is illustrated in Fig. 2.6; vertical velocities and streamlines for the nonlinear solution are shown in Fig. 2.6b. Relative to the linear solution (Fig. 2.6a), the nonlinear solution (Fig. 2.6b) has a much stronger downdraft-updraft couplet over the lee slope, and the lee trough is sharper. These large-amplitude short-wavelength features in the lee trough are not present in the linear simulation because there is little direct forcing at such wavelengths by the wider topography.

A deamplifying case is shown in Fig. 2.7. While the amplitude of the nonlinear simulation (Fig. 2.7a) is clearly reduced compared to the linear simulation (Fig. 2.7b), there are fewer structural differences between the linear and nonlinear solutions than there were in the amplifying case. In particular, the nonlinear solution in the deamplifying case lacks the short-wavelength perturbations in the lee of the ridge which develop in the nonlinear amplifying case (Fig. 2.6b).

2.4.2 Experiment 2: Gradual Transition at Tropopause

As might be expected given the results of Teixeira and Argaín (2020), when there is a more gradual transition at the tropopause, the difference between the troposphere-stratosphere solutions and those for a single layer of constant N and U case is reduced. The normalized cross-mountain pressure drag $\tilde{D}_{nl}$ for cases with $\Delta z = 1\,\mathrm{km}$, shown in Fig. 2.8a, maintains the general trend of a shift of the peak drag to higher tropopause heights as the mountain height is increased, but the magnitude of the finite-amplitude enhancement is reduced substantially from that apparent in Fig. 2.5a. The deviation of the nonlinear drag from the linear solution

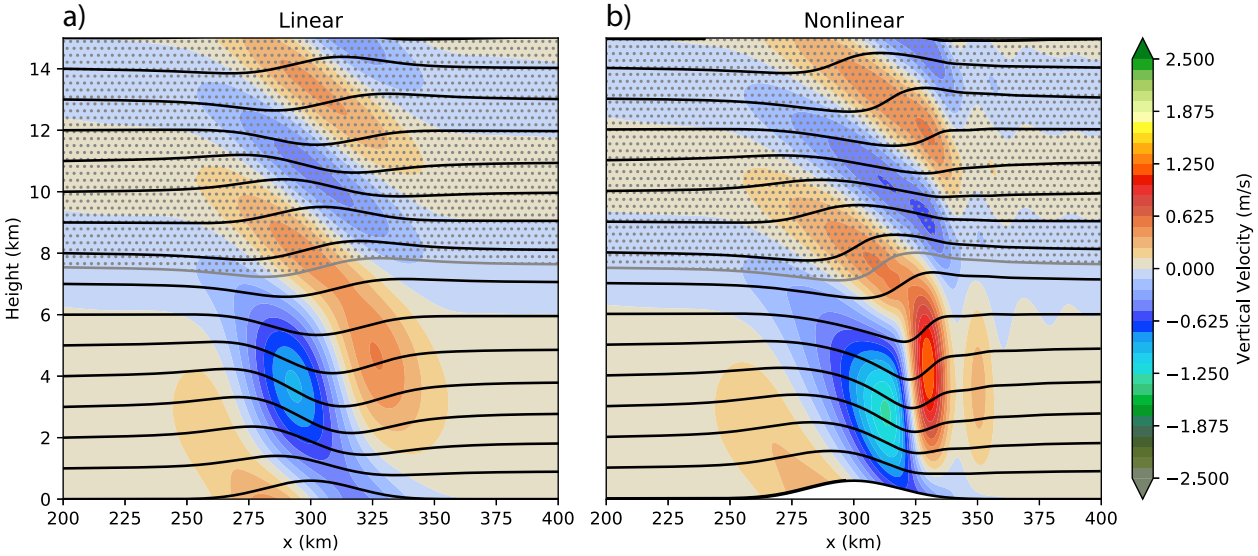

Figure 2.6: Vertical velocity (colour fill) and streamlines (black lines) from the (a) linear and (b) nonlinear meso12 simulations of an Experiment-1 case with nonlinear amplification in which $\tilde{z}_T = 0.55\lambda_L$ and $\tilde{h}_m = 0.3$. The grey line indicates the tropopause, and grey stippling indicates the stratosphere.

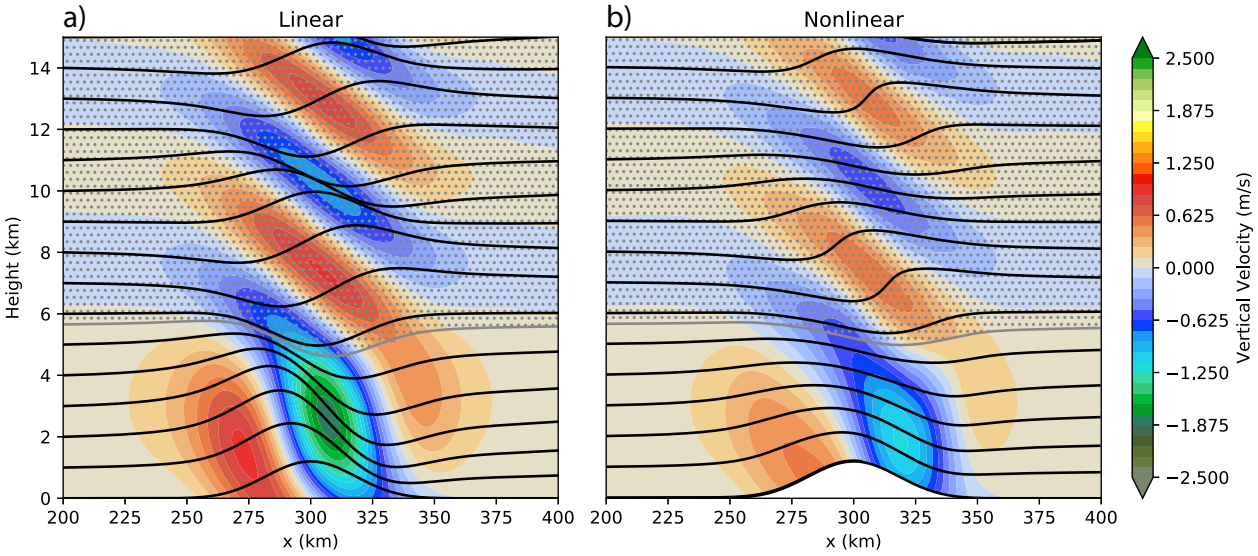

Figure 2.7: As in Fig. 2.6, but for a case with nonlinear deamplification in which $\tilde{z}_T = 0.45\lambda_L$ and $\tilde{h}_m = 0.6$.

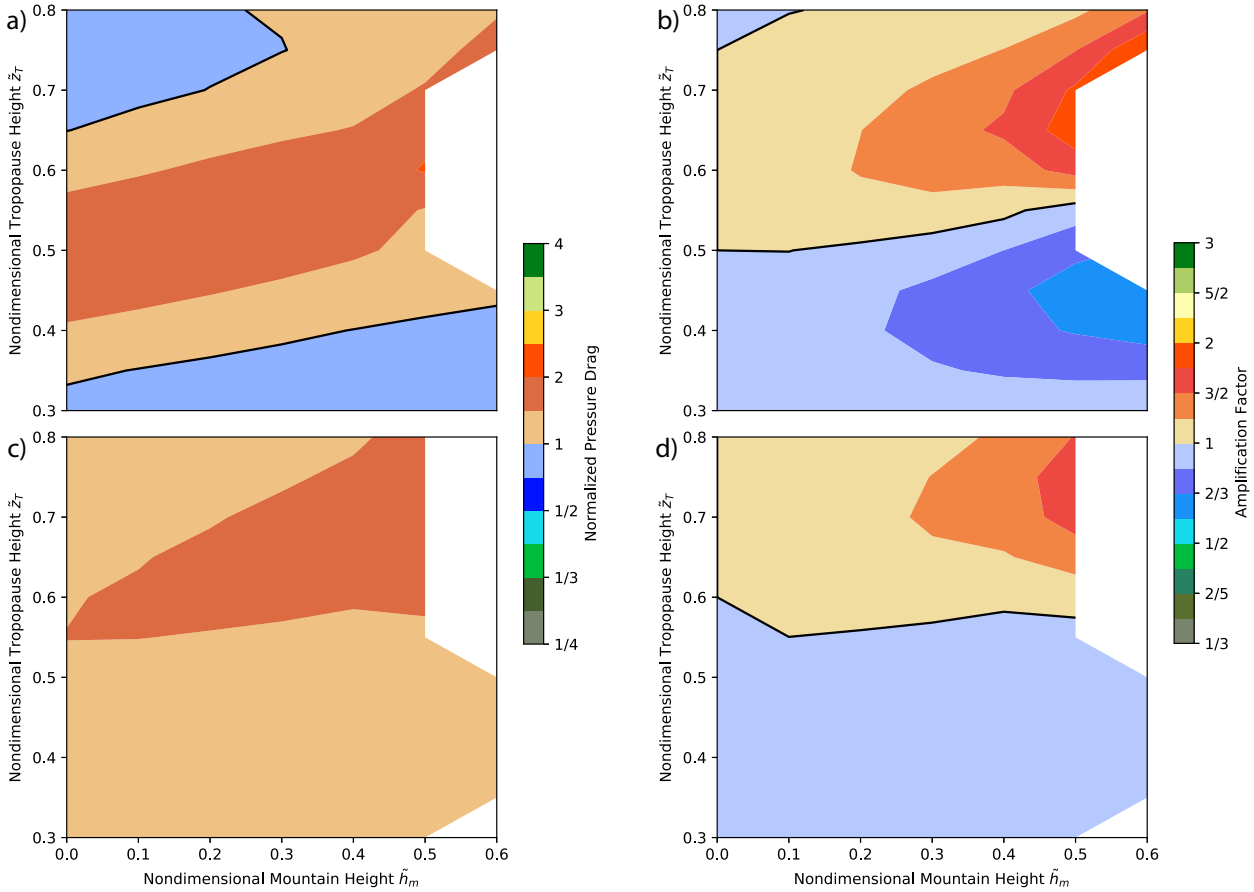

Figure 2.8: Normalized drag $\tilde{D}_{nl}$ as in Fig. 2.5a for the Experiment-2 simulations with (a) $\Delta z = 1\,\mathrm{km}$ and (c) $\Delta z = 2\,\mathrm{km}$. Amplification of the drag relative to the linear solution $\tilde{D}_{nl}/\tilde{D}_l$ as in Fig. 2.5b for cases with (b) $\Delta z = 1\,\mathrm{km}$ and (d) $\Delta z = 2\,\mathrm{km}$.

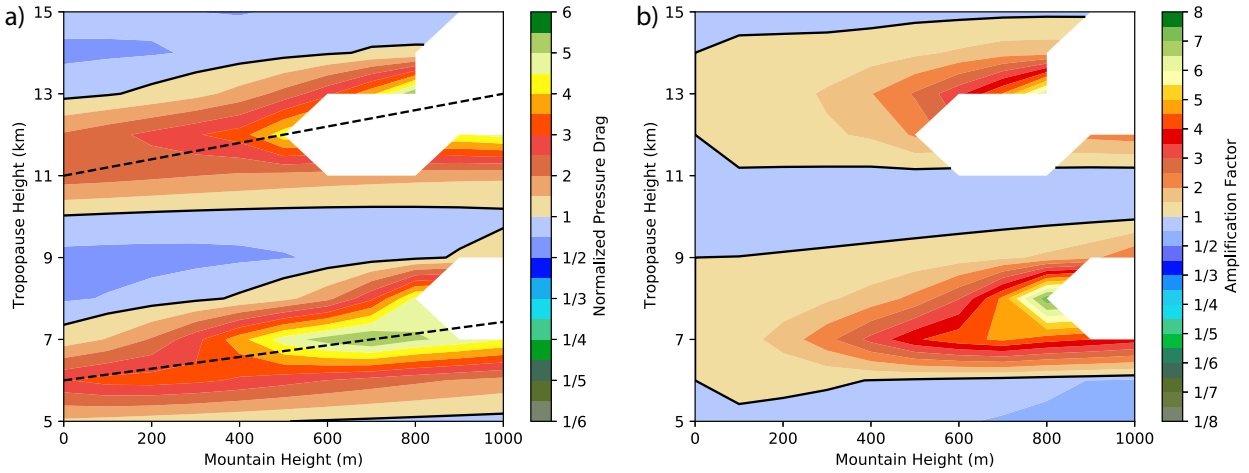

Figure 2.9: (a) Normalized drag $\tilde{D}_{nl}$ and (b) amplification of the drag relative to the linear solution $\tilde{D}_{nl}/\tilde{D}_l$, as in Fig. 2.5, for the Experiment-3 simulations.

$\tilde{D}_{nl}/\tilde{D}_l$ (Fig. 2.8b) is also reduced relative to the sharp tropopause result in Fig. 2.5b, even after accounting for the changes induced in the linear solutions by the more gradual change in static stability at the tropopause.

This lack of sensitivity to finite-amplitude processes is greater in the $\Delta z = 2\,\mathrm{km}$ case. The variation in $\tilde{D}_{nl}$ (Fig. 2.8c) is smaller than in the $\Delta z = 1\,\mathrm{km}$ case, and there is only a modest trend for the maximum drag to occur at higher tropopause heights as the mountain height increases. The difference between the drag for the linear and nonlinear solutions is particularly small (Fig. 2.8d).

2.4.3 Experiment 3: Sharp Tropopause, 10-30 m/s Shear

When moderate forward shear (cross-mountain wind speed increasing with height) and a sharp tropopause are present, the finite-amplitude enhancement of nonbreaking waves increases relative to the no-shear case. Normalized drag $\tilde{D}_{nl}$ for Experiment 3 is contoured as a function of the dimensional mountain and tropopause heights in Fig. 2.9a. The dimensional values of h_m and z_T are used in the shear flow cases for easy comparison with observations,

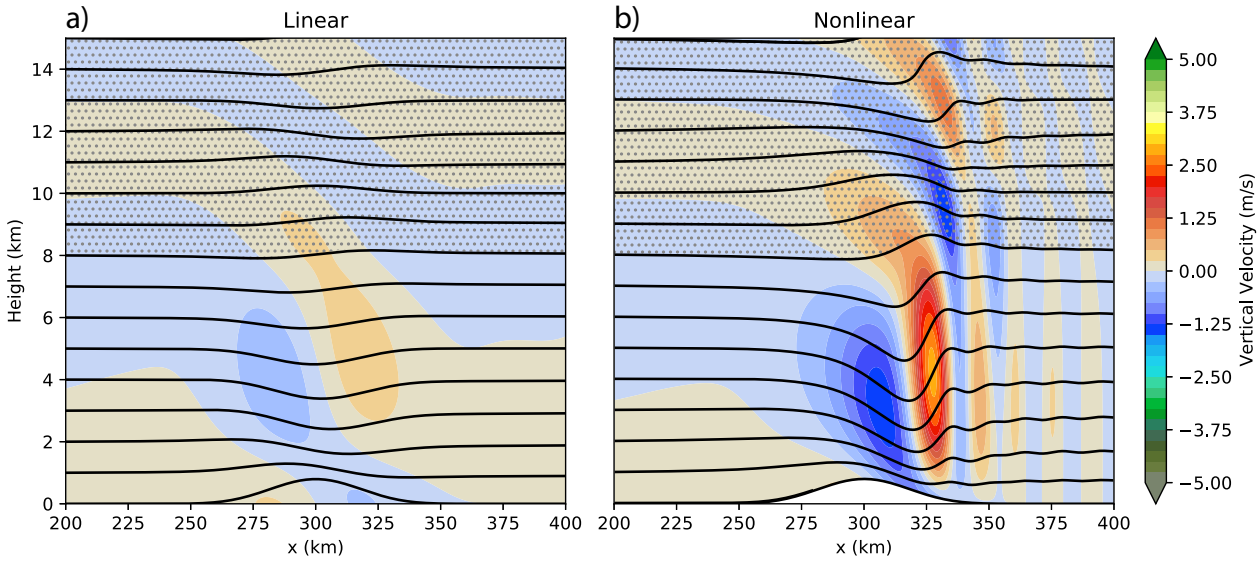

Figure 2.10: As in Fig. 2.6, but for the 10 m/s to 30 m/s shear sounding with a tropopause height of $z_T = 8\,\text{km}$ and a mountain height of $h_m = 800\,\text{m}$.

and because there is no unique choice for U in the computation of the nondimensional forms. Nevertheless, to facilitate comparison with the previous results we still compute $\tilde{D}_l$ and $\tilde{D}_{nl}$, taking U to be the value at the surface. The range of tropopause heights is sufficiently broad that $\tilde{D}_{nl}$ exhibits a quasi-periodic structure in the tropopause height z_T, with local maxima around 6.5 and 12 km. The values of $\tilde{D}_{nl}$ in these local maxima exhibit the trend seen previously in which there is a shift of the maximum drag to higher tropopause heights as the mountain height increases. The maximum $\tilde{D}_{nl}$ of 5.55 occurs for $h_m = 700\,\text{m}$, $z_T = 7$ km and is over twice the 2.56 maximum in the no shear case.

In contrast to Experiment 1, nonlinearity almost exclusively acts to increase the pressure drag (Fig. 2.9b). There are significant regions where $\tilde{D}_{nl}/\tilde{D}_l$ is greater than 2, with a maximum greater than 7. The de-amplification factor, on the other hand, is never less than 1/2. The maximum in $\tilde{D}_{nl}/\tilde{D}_l$ occurs in the case $h_m = 800\,\text{m}$, $z_T = 8$ km, which is particularly interesting because the linear solution is slightly deamplifying relative to the one-layer linear solution, but the nonlinear solution is strongly amplifying. The linear and

nonlinear solutions for this case are compared in Fig. 2.10. Although they do not directly contribute to the drag, weak partially-trapped waves are present in the nonlinear (Fig. 2.10b) simulation, while there are none present in the linear case (Fig. 2.10a). The generation of trapped waves due to short-wavelength forcing in the nonlinear lee wave has been previously well documented (Smith, 1976; Durran and Klemp, 1982).

2.4.4 Experiment 4: Sharp Tropopause, 10-50 m/s Shear

When the shear is stronger and $U(z)$ increases from 10 m/s at the surface to 50 m/s at the tropopause, the increase in the local WKB vertical wavelength of hydrostatic mountain waves in the troposphere places the region of maximum amplification in both $\tilde{D}_{nl}$ and $\tilde{D}_{nl}/\tilde{D}_l$ at typical mid-latitude tropopause heights between 9 and 11 km (Fig. 2.11). The amplification is similar to that for the the weaker shear in Experiment 3, although it occurs at lower mountain heights. In particular, $\tilde{D}_{nl}$ is greater than 4 when h_m is just 300 m and $z_T = 9$ km. $\tilde{D}_{nl}$ reaches a maximum of 6.6 when $h_m = 700$ m and $z_T = 10$ km, while $\tilde{D}_{nl}/\tilde{D}_l$ exceeds 9.5 when $h_m = 800$ m and $z_T = 11$ km. Very strong nonlinear effects in nonbreaking mountain waves can develop at very small mountain heights when there is strong forward shear in the troposphere.

As in Experiment 3, at most combinations of h_m and z_T, nonlinear effects amplify rather than damp the solution. Vertical velocities and streamlines from the strongly amplifying case $h_m = 800$ m and $z_T = 11$ km are shown in Fig. 2.12. Leaky trapped waves are pronounced in the nonlinear solution, but as in the previous Experiment 3 with weaker shear, they are absent in the linear case. The vertical velocities and trapped wave amplitudes in the nonlinear Experiment-4 simulation are both significantly stronger than in Experiment 3, despite both cases having equal values of h_m.

2.5 Discussion

Neither the free-slip boundary condition at the surface, nor the matching conditions across the tropopause (requiring continuity of the pressure and the normal component of the ve-

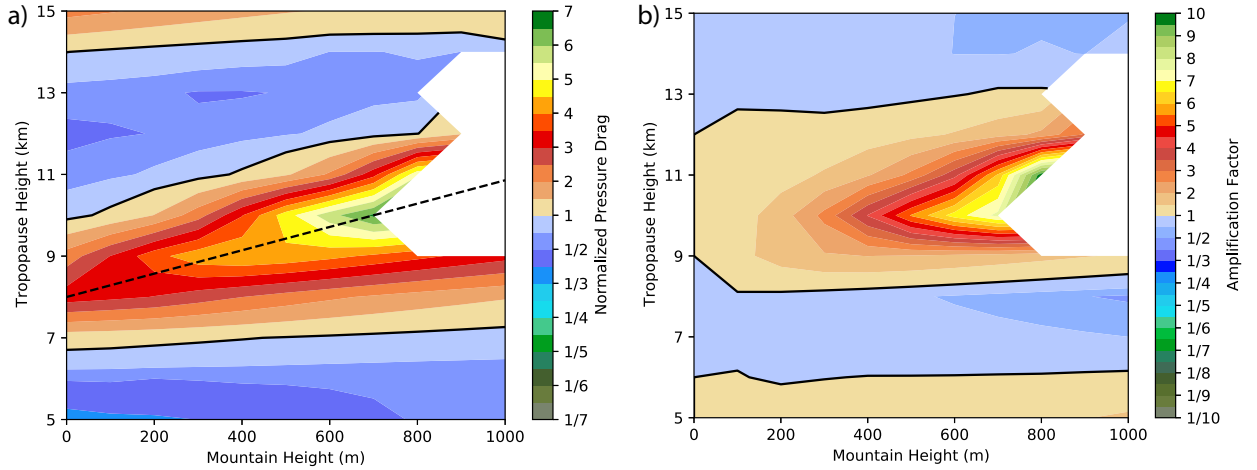

Figure 2.11: (a) Normalized drag $\tilde{D}_{nl}$ and (b) amplification of the drag relative to the linear solution $\tilde{D}_{nl}/\tilde{D}_l$, as in Fig. 2.5, for the Experiment-4 simulations.

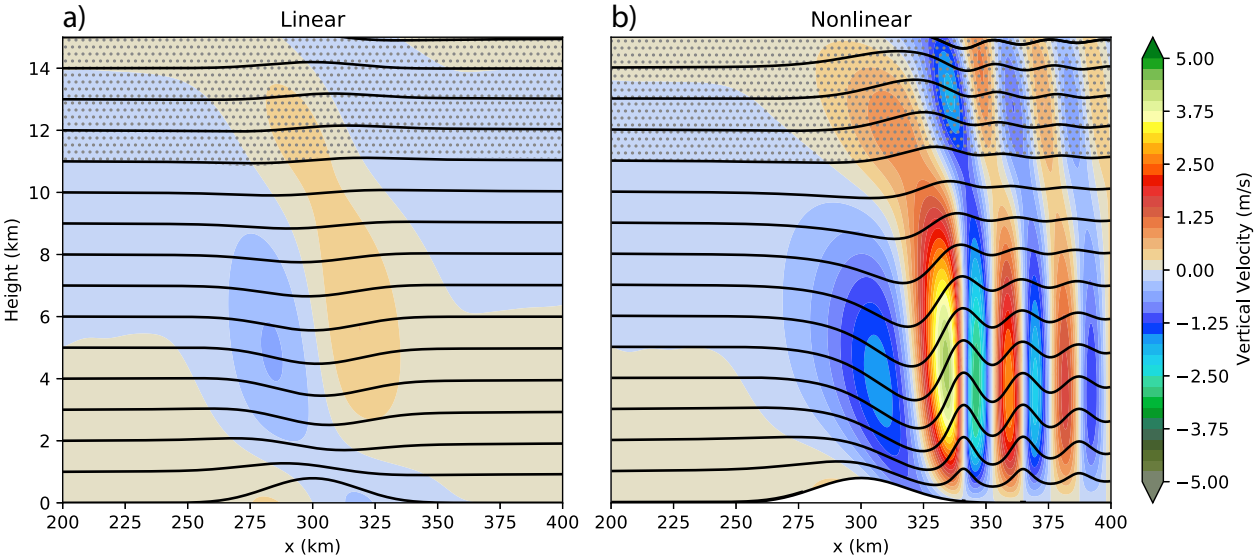

Figure 2.12: As in Fig. 2.6, but for Experiment 4 with $h_m = 800\,\mathrm{m}$ and $z_T = 11\,\mathrm{km}$.

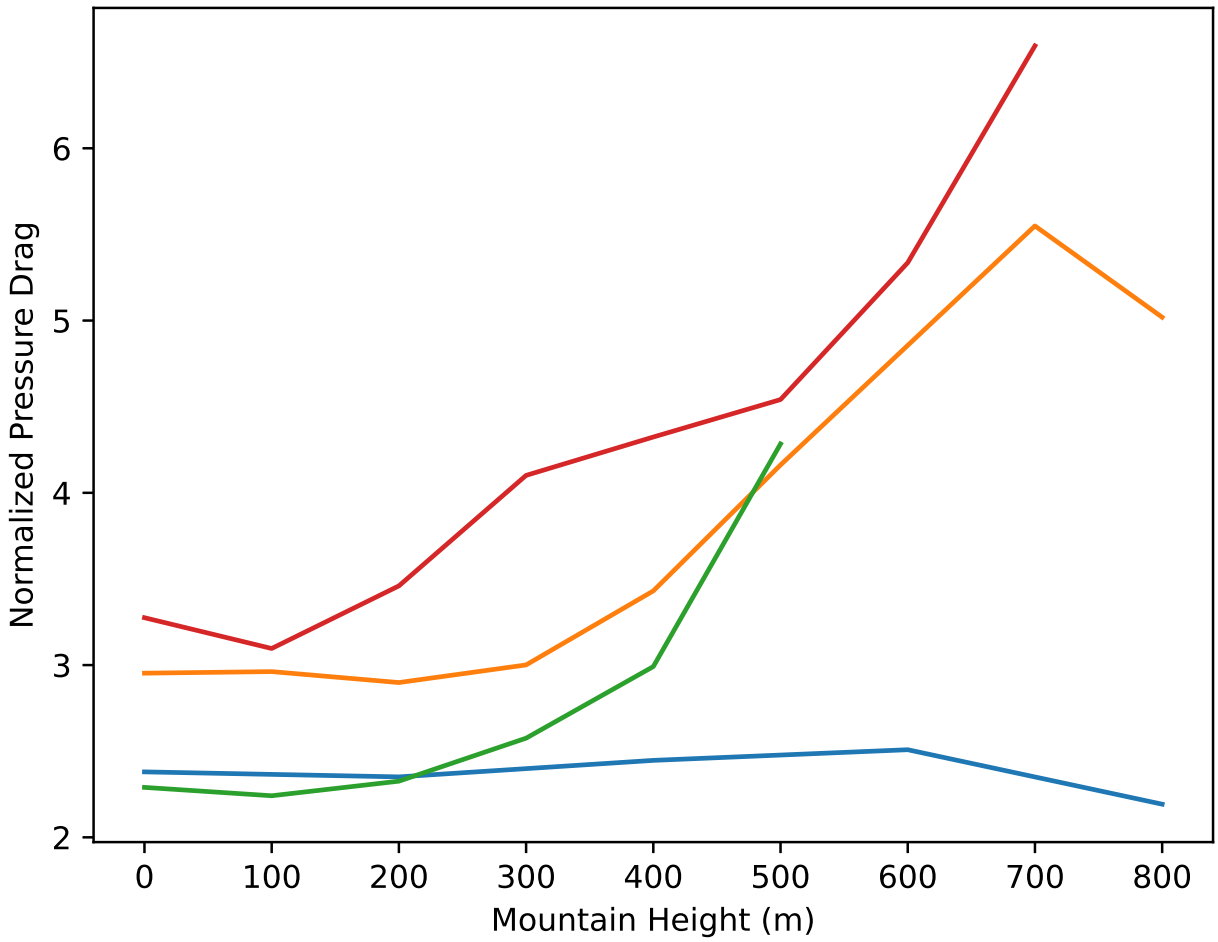

Figure 2.13: Normalized pressure drag as a function of mountain height along the dashed lines in Figs. 2.5a, 2.9a and 2.11a for the no-shear case (blue), the lower-level/upper-level maximum in the 10-30 m/s case (green/orange), and for the 10-50 m/s case (red).

locity) are nonlinear in the unknown variables. Durran (1992) noted there is an effective reduction in the depth of the troposphere over finite-amplitude mountains, and found that tropopause heights giving the strongest drag can be adjusted to capture this finite-amplitude behaviour by generalizing the tuning criteria for maximum drag in linear hydrostatic mountain waves from $z_T = 0.5\lambda_L$ to $z_T - 1.5h_m = 0.5\lambda_L$. A similar adjustment works well over the wider range of mountain heights and tropopause elevations considered in our no-shear simulations, for which normalized drags are plotted in Fig. 2.5a along with a dashed line following the extrema in $\tilde{D}_{nl}$ given by $z_T - 1.17h_m = 0.5\lambda_L$ (fit by eye; note that this is close to simply calculating the tropopause height as the distance above the mountain top, instead of the surrounding flat ground). Plotting $\tilde{D}_{nl}$ as a function of mountain height *along this dashed line* yields the almost-horizontal blue curve in Fig. 2.13, indicating that linear theory for the two-layer problem can give the correct drag, at least for the strongest events, after making a finite-amplitude adjustment to the depth of the troposphere.

Similar attempts to apply two-layer linear theory via a simple adjustment of the effective depth of the troposphere did not, however, work well for the cases with vertical wind shear. Dashed lines indicating the approximate (h_m, z_T) values for which $\tilde{D}_{nl}$ achieves a local maximum appear in Figs. 2.9a and 2.11a; the normalized pressure drags along these curves are plotted as a function of h_m in Fig. 2.13. These curves are not quasi-horizontal, but rather indicate that, in the wind-shear simulations, a significant amplification of $\tilde{D}_{nl}$ occurs beyond that which can be accounted for by simple reductions in the tropospheric depth above finite-amplitude mountains.

The additional amplification of the drag in the wind-shear cases is associated with a significant nonlinear strengthening of the lee-side trough, as may be illustrated by plotting the local contribution to the pressure drag $p' \, dh/dx$ at each point on the topography. Fig. 2.14 shows the behaviour of this local drag for three different environments: no-shear with $z_T =$ 8.16 km ($\tilde{z}_T = 0.65$), winds increasing from 10 to 30 m s^{-1} with $z_T = 8$ km, and winds increasing from 10 to 50 m s^{-1} with $z_T = 11$ km. Individual curves for mountain heights of 200, 400, 600, and 800 m are plotted for each environmental profile. In all three cases,

the largest contribution to the pressure drag occurs along the lee slopes as a result of low surface pressures under the lee-side trough. The increase in the amplitude of this lee-side contribution, as h_m increases from 400 to 600 to 800 m, is much more pronounced in the two cases with wind shear. In those cases the rate at which the drag increases with h_m is also much faster than the h_m^2 scaling that would be expected from linear theory if the influence of finite mountain height on the effective tropospheric depth is neglected.

Streamlines and vertical velocities for the linear and nonlinear h_m = 800-m, 10-30 m s^{-1} simulations are compared in Fig. 2.10. The dramatic intensification of the lee trough responsible for the increased local drag in Fig. 2.14b is clearly apparent. Nonlinear wave interactions have substantially amplified short-wavelength contributions to the wave downstream of the trough axis. At a height of $z = 2$ km, the half wavelength between the trough and the downstream ridge ($325 \leq x \leq 340$) is approximately 15 km. The terrain itself is too wide to directly force strong 30-km-wavelength perturbations—instead they are forced by the nonlinear wave dynamics. A similar situation is apparent for the 10-50 m s^{-1} simulations shown in Fig. 2.12, for which the local drag contribution is plotted in Fig. 2.14c.

Smith (1976) proposed that nonlinear flow over barrier can trigger a strong, short wavelength trough, thereby forcing larger-amplitude lee waves downstream than those which would be obtained from a linear calculation. Further evidence of such nonlinear amplification appears in Durran (1992, 2015b), and in all the cases in these previous studies, the environmental profile supporting the trapped waves has a two-layer structure with high static stability in the lower layer. In contrast to these previous studies, the decrease in the Scorer parameter with height responsible for partially trapping the waves in Figs. 2.10b and 2.12b is produced by the increase in U with height without any variation of the static stability within the troposphere.

The vertical structures of the partially trapped waves supported by the environmental profiles of the Scorer parameter in the shear-flow cases in Figs. 2.10 and 2.12 were evaluated using the eigenvalue-eigenfunction solver described in Durran et al. (2015) as modified in Metz et al. (2020). Fig. 2.15a,c shows the vertical profile of the Scorer parameter squared

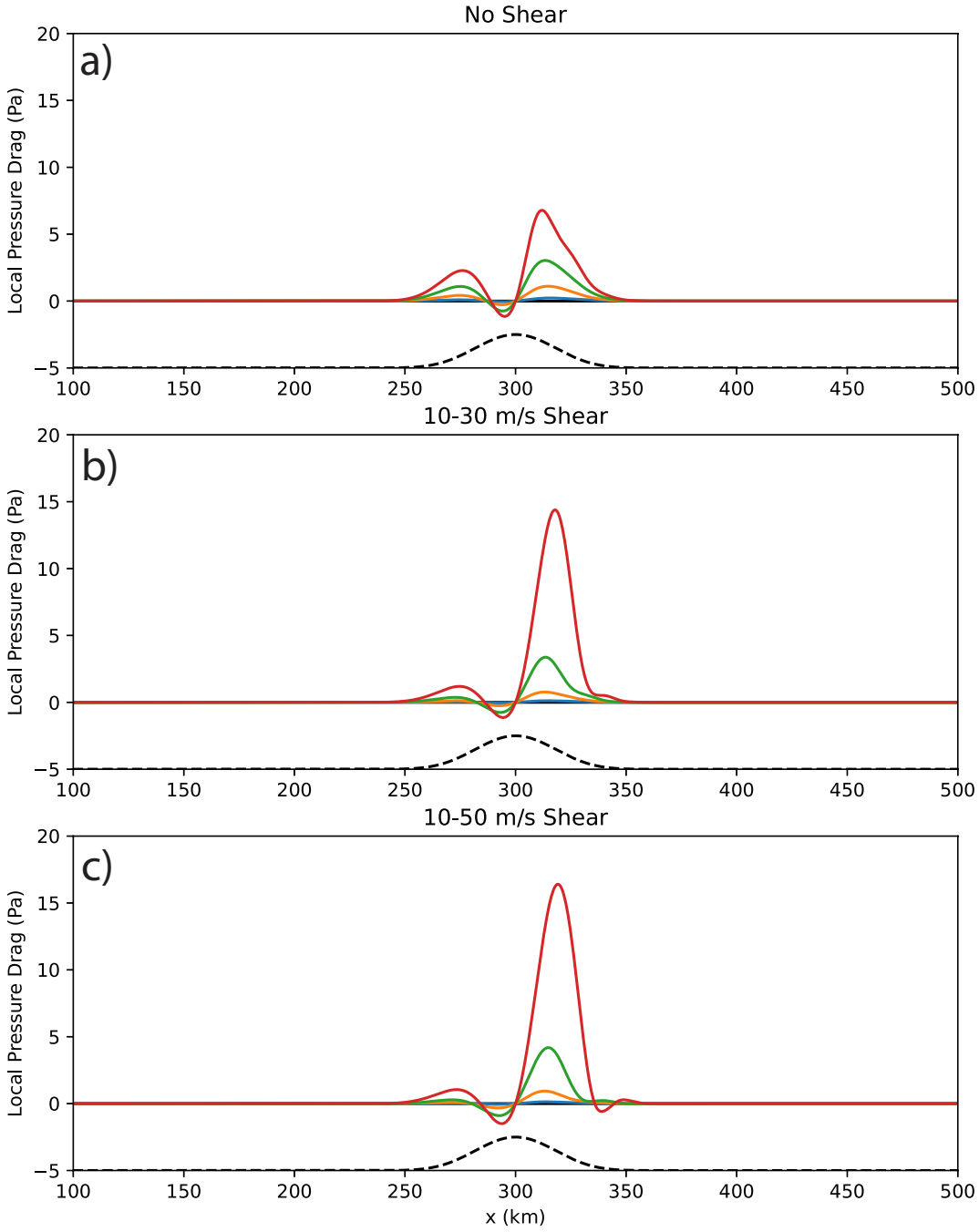

Figure 2.14: Local pressure drag for the (a) no-shear case, (b) 10-30 m/s shear case, and (c) 10-50 m/s shear case. Blue, orange, green, and red lines are for mountain heights of 200 m, 400 m, 600 m, and 800 m, respectively. Tropopause heights are $\tilde{z}_T = 0.65$ for the no-shear case and $z_T = 8\,\text{km}$ and $z_T = 11\,\text{km}$ for the 10-30 m/s and 10-50 m/s shear cases, respectively. For reference, the mountain profile is plotted as a black dashed line.

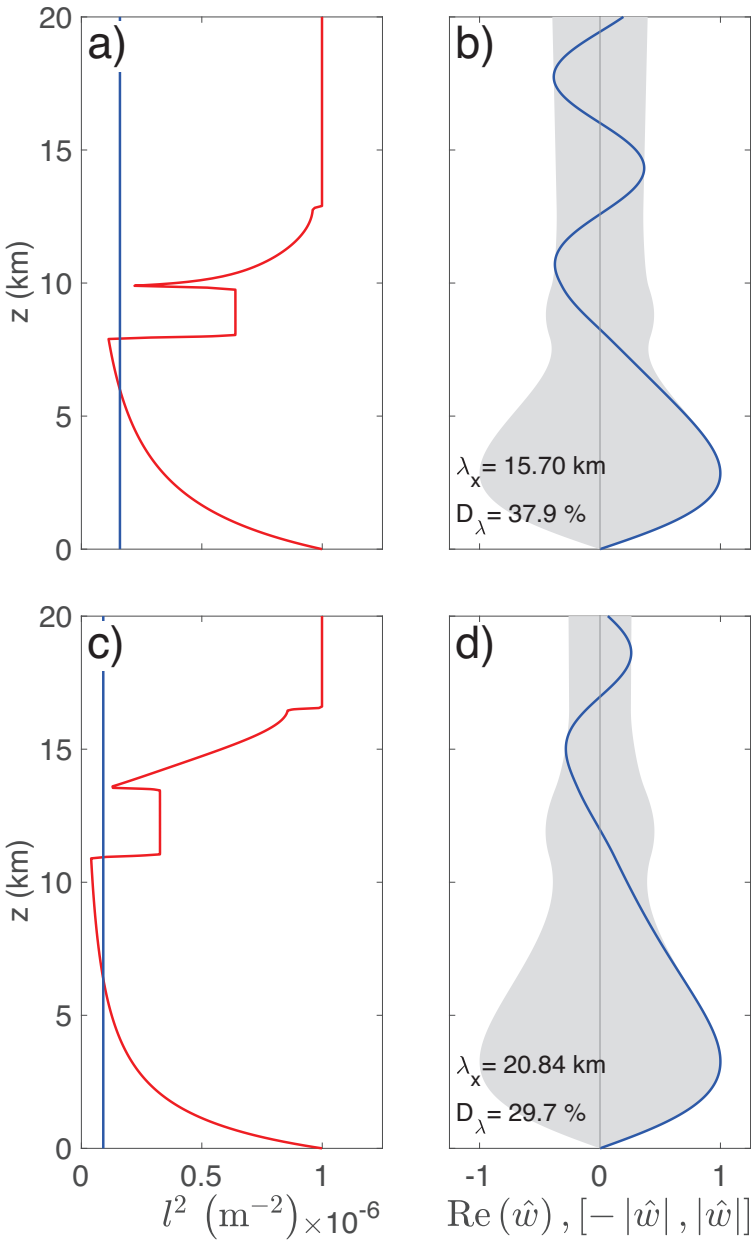

Figure 2.15: Vertical profiles of (a, c) Scorer parameter l squared (red) and (b, d) real part of the Fourier-transformed vertical velocity $\hat{w}(z)$ for the trapped wave mode supported by the (a, b) 10-30 m/s shear case with a tropopause height of 8 km and (c, d) 10-50 m/s shear case with a tropopause height of 11 km. The horizontal wavenumber k of this mode is plotted as the blue vertical line in (a, c). The grey shading in (b, d) indicates the interval $[-|\hat{w}|\,,|\hat{w}|]$, where $|\hat{w}|$ is the magnitude of $\hat{w}$. The parameters λ_x and D_λ indicate the horizontal wavelength and downstream decay per wavelength, respectively.

for the 10-30 and 10-50 m s^{-1} shear flows, respectively, while Fig. 2.15b,d illustrates their modal structures by profiles of $\hat{w}(z)$, defined such that $w(x,z) = \mathrm{Re}\left(\hat{w}(z)e^{ikx}\right)$. Also noted in panels b and d are the horizontal wavelengths $\lambda_x = 2\pi/k$ for each mode and their downstream decay rate D_λ, defined as the fraction of the wave amplitude lost over a distance λ_x. The upper-tropospheric layer throughout which $l^2 < k^2$, and the waves decay, is only a few kilometres deep (the layer just below the tropopause where the red curve lies to the left of the blue line in Fig. 2.15a,c), so it is not surprising that both modes decay rapidly downstream as they leak energy upward, losing roughly 38% and 30% of their amplitude over one horizontal wavelength. The wavelengths and vertical structure of the downstream waves in the numerical simulations closely match those shown in Fig. 2.15.

The extent to which these partially trapped modes contribute to the drag is unclear. The ability of trapped waves to exert a drag on the flow was demonstrated in the classic paper by Bretherton (1969), yet the trapped waves themselves do not transport momentum vertically. Rather their interaction with the mountain produces a vertical divergence in the horizontally averaged momentum flux (Durran, 1995; Lott, 1998; Broad, 2002). The situation for these rapidly decaying waves that do transport momentum vertically (note the sinusoidal oscillations in the stratosphere in Fig. 2.15b,d) is more complex and needs further study. Nevertheless, the pronounced amplification of these waves clearly illustrates the consequences of the nonlinear scale interactions in the high-drag simulations with significant vertical shear.

2.6 Conclusions

Our simulations have demonstrated that mountain waves encountering a sharp tropopause can experience large changes in amplitude and substantial deviations in momentum flux compared to that which would be present in an environment with constant values of N and U representative of the conditions near mountain-top level. Many GWD parameterizations will, therefore, be in error because they assume the low-level momentum flux is proportional to the constant-N-and-U drag in linear waves launched by the unblocked flow over the top of the ridge. Note in particular that large deviations between constant-N-and-U GWD

estimates and the actual momentum fluxes can occur at amplitudes below the wave-breaking threshold.

Linear theory is often applied to the mountain wave problem using WKB theory, but that theory assumes a slowly varying background state that is violated at a sharp tropopause. Linear theory can alternatively be formulated for distinct atmospheric layers with matching conditions between the layers, including cases with linear variations in $U(z)$ within each layer (Klemp and Lilly, 1975), thereby allowing a reasonably close match to observed sounding profiles. Nevertheless, our results suggest that the finite-amplitude solutions can differ dramatically from such multi-layer linear solutions, which is consistent with previous findings in the more limited case without vertical wind shear (Durran, 1992). The differences between the linear and finite-amplitude results are large enough that there would be little reason to try to incorporate complex multi-layer linear models with vertical wind shear in GWD parameterizations.

In the simplest two-layer case with no vertical wind shear, linear theory accurately predicts the range over which the drag varies in response to changes in the tropopause height, but the functional dependence on z_T is incorrect. Finite-amplitude effects tend to shift the extrema in the drag to higher tropopause heights as the mountain height increases, decreasing the effective depth of the troposphere (Fig. 2.5). Similar to Durran (1992), the optimal tropopause height for maximum drag could be estimated by empirically correcting the condition from linear theory through the inclusion of a term proportional to the mountain height. We also demonstrated that, at least for the strongest cases, good estimates of the finite-amplitude drag could also be obtained from linear theory using the same empirical correction.

The sensitivity of the surface pressure drag to finite-amplitude effects increases when the cross-mountain winds increase with height. In this case, multi-layer linear theory does not accurately predict the range of possible pressure drags. For example, in the 10-30 m/s shear case, $\tilde{D}_l$ ranges from approximately 0.5 to 3.0, while $\tilde{D}_{nl}$ varies from 0.5 to 4.8. In the 10-50 m/s shear case, strong nonlinear amplification relative to typical GWD estimates can occur

over mountains that are just 250 m high (Fig. 2.11a). Nonlinear dynamics are important in the high-drag cases with wind shear, and it is not possible to obtain good agreement with linear theory by simply compensating for changes in the effective tropospheric depth above finite-height topography. Leaky trapped waves appear in the high-drag simulations with significant wind shear, triggered by short-wavelength structures in the lee-trough immediately downstream of the mountain. These waves match the vertical-mode structure of the leaky modes supported by the oncoming background flow as computed using linear theory. The strong nonlinear response in vertically sheared environments is qualitatively similar to that previously documented in cases where a significant decrease in the Scorer parameter with height is produced, not by increases in wind speed, but by decreases in the upper tropospheric static stability (Durran, 1986). The influence of these leaky waves on the drag, and the influence of the tropopause on these leaky waves, are topics for further study.

An important additional influence of vertical shear, due to the change in the vertical wavelength from the varying wind speed, is to modulate the level at which the drag is most sensitive to partial reflections from the tropopause. The dry Brunt-Väisälä frequency, averaged over the full depth of the troposphere, is usually near 0.01 s^{-1}. Given an N_L of 0.01 s^{-1}, an environmental wind profile in which $U(z)$ increases linearly from 10 m/s near the surface to 50 m/s at the tropopause will be conducive to very strong nonlinear amplification of the mountain-wave drag when z_T has a typical mid-latitude value in the range between 8 and 11 km.

We have focused on the impact of partial back reflections of vertically propagating waves at the tropopause, and on the influence of strong vertical wind shear, because they are ubiquitous mid-latitude features (Birner, 2006). Other sharp changes in atmospheric structure, such as the presence of an inversion layer near mountain top-level, are also known to have a strong influence on the amplitude of mountain waves (Durran, 1986, Figs. 10-13), and these influences extend into the wave-breaking regime. A thorough analysis in the influence of elevated inversions and the behaviour of breaking mountain waves in environments with wind shear and static-stability layering is beyond the scope of this paper. Nevertheless,

our results demonstrate that finite-amplitude effects in mountain waves cannot be reliably accounted for without numerically computing the actual wave response. As a consequence, the associated gravity-wave drag is not easily parameterized, and errors due to improper representation of GWD in global weather and climate models are likely to remain nontrivial unless the grid spacing becomes small enough to resolve the waves. The current efforts to develop and migrate to global cloud-resolving models could provide the required numerical resolution and thereby promise to improve representation of orographic wave drag (Satoh et al., 2019).

Appendix 2.A Generation of Shear Soundings

The shear soundings are constructed differently in the troposphere than in the stratosphere. In the troposphere, we specify $N = 0.01\,\mathrm{s}^{-1}$ and linear shear

$$U(z) = \frac{U_T - 10\,\mathrm{m/s}}{z_T} z + 10\,\mathrm{m/s}, \tag{2.19}$$

where z_T is the height of the tropopause and U_T is the wind speed at the tropopause. In the stratosphere, we employ a more complex procedure designed to obtain a smooth profile that eventually transitions to a constant value of $U_S = 20\,\mathrm{m/s}$. Note that the definition of the Scorer parameter (Eq. 2.2) can be rearranged as a second order nonlinear ordinary differential equation for the basic-state wind speed U:

$$\frac{d^2U}{dz^2} - \frac{N^2}{U} + Ul^2 = 0. \tag{2.20}$$

This equation can be solved numerically as an "initial value problem" in the height variable z, for which purpose we use the SciPy `odeint` function. Defining $\zeta = z - z_T$, we specify $U(\zeta = 0) = U_T$ and $U'(\zeta = 0) = (U_T - 10\,\mathrm{m/s})/z_T$. In addition, we specify a constant value for the Scorer parameter, $l = 0.02/U_m\ \mathrm{m}^{-1}$, where $U_m = (U_T + 20)/2$ is chosen as the average of the wind speed at the tropopause and the constant upper-stratospheric value.

Specifying N^2 will completely specify the profile of U. However, in general, a constant value of N in the stratosphere will result in large sinusoidal variations in U with height. To prevent this, we still specify a constant value of $N = 0.02\,\mathrm{s}^{-1}$, but we transition from the oscillatory wind profile to a constant U profile by fitting an elliptic wind profile in between. The wind profile in the elliptic transition region is given by

$$U_e(z) = U_0 - \sqrt{a^2 \left[1 - \frac{(z - z_0)^2}{b^2}\right]}. \tag{2.21}$$

This equation has four free parameters: the U- and z-coordinates of the centre of the ellipse U_0 and z_0 and the length of the semi-major and semi-minor axes a and b. We in turn specify four matching conditions, two at each boundary of the elliptic transition region. The lower

boundary is specified as being at the first point $z = z_i$ above the tropopause where the curvature of the wind profile is zero, while the upper boundary is specified to be $\Delta z = 3\,\mathrm{km}$ above the lower boundary. At both of these points we require that both the wind profile and the first derivative be continuous. The resulting equations for each parameter are given by

$$U_0 = \frac{U(z_i)\,U'(z_i)\,\Delta z + U(z_i)^2 - U_S^2}{U'(z_i)\,\Delta z + 2\,[U(z_i) - U_S]}, \tag{2.22}$$

$$a^2 = (U_S - U_0)^2, \text{ and} \tag{2.23}$$

$$b^2 = \frac{(U_0 - U_S)^2\,\Delta z^2}{2U(z_i)\,U_0 - U(z_i)^2 - 2U_S U_0 + U_S^2}, \tag{2.24}$$

where $U_S = 20\,\mathrm{m\,s^{-1}}$ is the constant wind speed above the transition region, $\Delta z = 3\,\mathrm{km}$ is the thickness of the transition region, and $U(z_i)$ and $U'(z_i)$ is the wind speed and first derivative of the wind speed at the lower boundary z_i of the transition region. An example result from this procedure is shown in Fig. 2.16.

Appendix 2.B Computation of Linear Streamlines

Linear solutions are obtained by assuming all perturbations about a reference state are arbitrarily small. Under this small-amplitude assumption, the vertical excursions of streamlines about a horizontal reference line would be infinitesimal, and they would simply appear as horizontal lines. The amplitude of linear solutions is scaled up when approximating the flow over a finite-amplitude mountain, but this leads to an inconsistency between two possible ways to display the streamlines.

Streamlines in the 2D x-z plane satisfy

$$\frac{dz}{dx} = \frac{w}{u}. \tag{2.25}$$

In the standard finite-amplitude computation, the velocities on the right side of the preceding are evaluated at each point along the streamline, in which case the (x, z) coordinates of a streamline originating at the point (x_0, z_0) may be computed as a function of the parameter s using

$$x(s) = x_0 + \int_0^s u\,(x(\alpha), z(\alpha))\,d\alpha \tag{2.26}$$

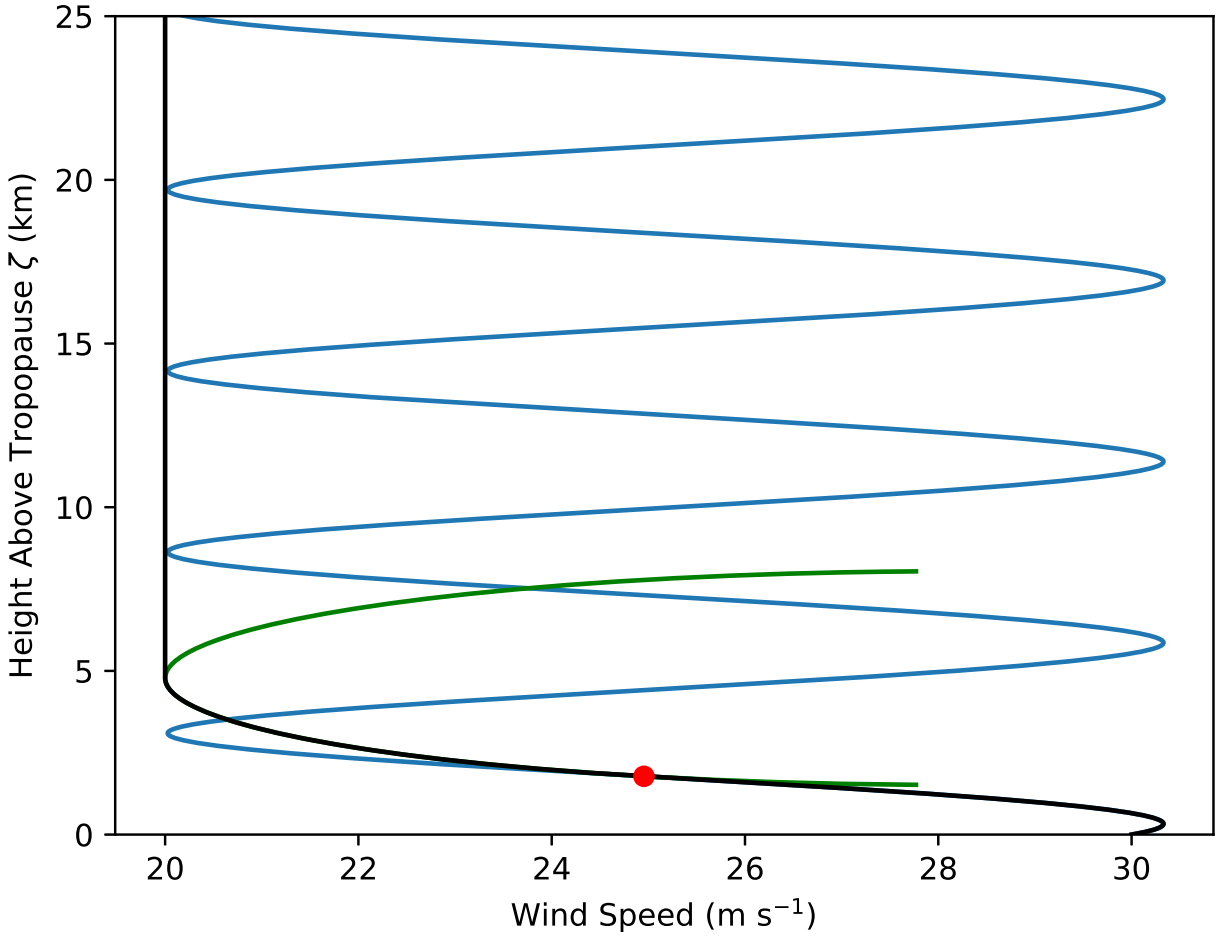

Figure 2.16: Demonstration of the construction of a wind profile in the stratosphere. The blue curve indicates the solution for a constant Scorer parameter l. The red dot indicates the first point with zero curvature above the tropopause, while the green curve indicates the ellipse used to transition between the constant-l and constant-U profiles. The resulting wind profile is shown in black.

$$z(s) = z_0 + \int_0^s w\left(x\left(\alpha\right), z\left(\alpha\right)\right) d\alpha. \tag{2.27}$$

Streamlines computed in this manner are plotted in red in Fig. 2.17 for one-layer constant-N-and-U linear flow over a Witch-of-Agnesi mountain. Note that the surface streamline does not follow the mountain profile (shown in blue). For steady adiabatic flow, this procedure generates lines identical to those that would be obtained by applying a standard contouring algorithm to the potential temperature field. As with streamlines, if isentropes are plotted in this manner, they will not coincide with the mountain profile.

To obtain a streamline that follows the mountain, it is necessary to return to the small-amplitude assumption by neglecting the functional dependence of u and w on the amplitude of the streamline displacement. This requires replacing $z(\alpha)$ in Eq. 2.26 and 2.27 with z_0. Consistent with the linearization assumption, u must be approximated by the basic-state horizontal velocity U. The coordinates $(\tilde{x}, \tilde{z})$ of such streamlines satisfy

$$\tilde{x}(s) = x_0 + U(z_0)s \tag{2.28}$$

$$\tilde{z}(s) = z_0 + \int_0^s w\left[\tilde{x}(\alpha), z_0\right] d\alpha. \tag{2.29}$$

Streamlines plotted using Eqs. 2.28 and 2.29 are shown in black in Fig. 2.17. The surface streamline perfectly follows the mountain contour, and is identical to the blue curve. Over the mountain, the magnitudes of the slopes of the black streamlines are similar around $z = 2.3$ and 4.6 km, but they are opposite in sign. In contrast, the red streamlines are much steeper than the black streamlines at 4.6 km, and less steep at 2.3 km. *In this case where U is constant with height, the red lines are actually streamlines for the solution to Long's equation (Eq. 2.1) for flow over a mountain whose profile matches the lowest red streamline in Fig. 2.17.*

We have used Eqs. 2.28 and 2.29 in all plots of linear solutions in this paper because in most respects this choice more faithfully represents the linear solution. But there is one drawback to this approach: when the amplitude is sufficiently large and the streamline spacing is sufficiently tight, sets of $(\tilde{x}, \tilde{z})$ streamlines can cross. Such crossing streamlines are

a manifestation of the inconsistency resulting from computing solutions under an assumption of infinitesimal amplitude and then scaling up the amplitude of the result.

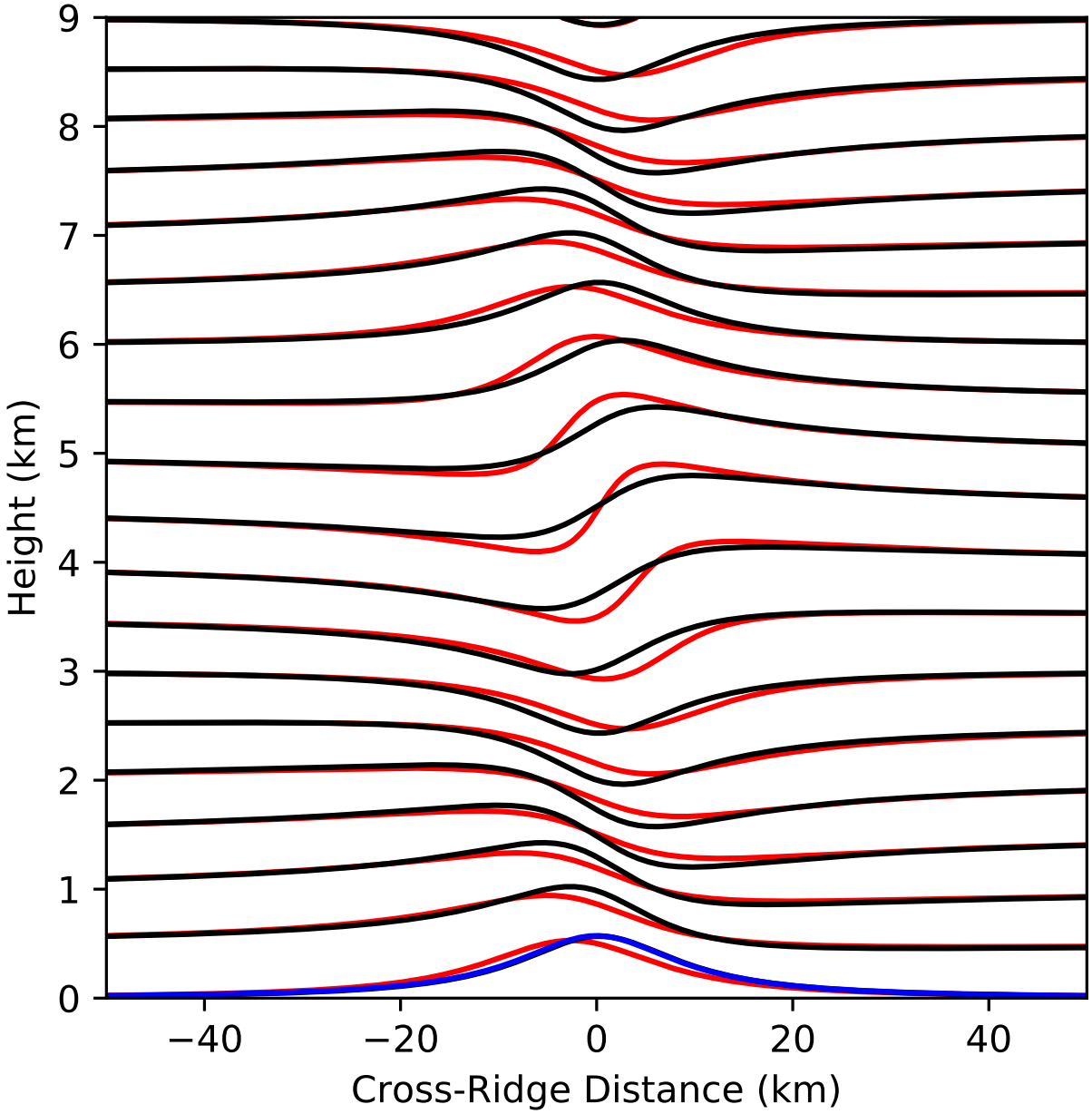

Figure 2.17: Comparison between two methods of plotting linear streamlines in flow from left to right over a Witch of Agnesi mountain: red lines use Eqs. 2.26 and 2.27; black lines use Eqs. 2.28 and 2.29. The mountain profile is shown in blue and coincides with the lowest black streamline.

Chapter 3

PREDICTABILITY OF DOWNSLOPE WINDSTORMS IN CRITICAL-LEVEL AND NON-CRITICAL-LEVEL ENVIRONMENTS

3.1 Introduction and Background

Downslope windstorms in the lee of mountains are high-impact weather events, where the peak winds have been known to exceed 50 m/s (Durran, 1990). Damage from these events can be severe, and in areas prone to these windstorms, for example the Colorado Front Range, accurate prediction with as much lead time as possible is important. Whether or not it is actually possible to accurately predict downslope windstorms with long lead times is, therefore, an important question to answer. Reinecke and Durran (2009) conducted experiments on two windstorm cases from the Terrain-Induced Rotor Experiment (T-REX; Grubišić et al., 2008) in the lee of the Sierra Nevada range in California. Their results showed significant variability among ensemble members, even at short lead times. In the first case with a large-amplitude breaking mountain wave, the difference between the average of the ten strongest and the average of the ten weakest members is over 22 m/s after 6 hours of simulation time. In a case without a breaking wave, where the downslope winds were generated by a high static stability layer underneath a layer of lower stability, the differences were less dramatic, but still significant.

On the other hand, there have been cases where windstorms appear to have extended predictability. For example, Lawson and Horel (2015b) analyzed a windstorm along the Wasatch Front of Utah on 1 December 2011. The authors noted that forecasters had cited the possibility of a damaging downslope event up to 90 hours prior to the event. Lawson and Horel (2015b) attributed the increased predictability to the correct depiction of the synoptic

setup in most of the ensemble members and flow diversion due to a secondary topographic ridge, which steers the flow to an easterly direction. Although long lead time predictions for this case verified, the long-term reliability of downslope-wind forecasts for the Wasatch Front was not investigated.

However, the nature of the windstorm along the Wasatch Front, in particular its occurrence along the west side of the Wasatch Range, leads to another possible source of enhanced predictability: the presence of a mean-state critical level. Since easterly winds are required for a downslope windstorm to occur on the west side of a mountain range, the presence of a mean-state critical level, i.e., a level where the cross-mountain basic-state wind speed $U = 0$, is almost assured as the typical upper-tropospheric flow at the latitude of the Wasatch Range is westerly. As discussed in Chapter 1, the presence of a mean-state critical level can enhance the mountain wave response and lead to strong wind perturbations at the surface (Klemp and Lilly, 1978; Clark and Peltier, 1984; Smith, 1985). This type of flow regime also occurs in the Santa Ana winds of Southern California and the Croatian bora, but it is notably not present in the flows responsible for the windstorms in the Owens Valley in Reinecke and Durran (2009).

There is some indication that winds in the Croatian bora may be relatively insensitive to the exact height and structure of the critical level (Klemp and Durran, 1987). If that is so, perhaps downslope windstorms induced by this mechanism exhibit enhanced predictability. Why might downslope windstorms in the mean-state critical level regime exhibit enhanced predictability? The work of Smith (1985) and Bacmeister and Pierrehumbert (1988), coupled with the hypotheses of Anthes et al. (1985), discussed more fully in Chapter 1, provide a theoretical context. Essentially, since a wide range of critical level heights are capable of supporting the transition from subcritical to supercritical flow, and since there appears to be an adjustment mechanism to allow the flow to adjust to the transition critical level height corresponding to a given mountain height, there appears to be a relative insensitivity to the precise height of the mean-state critical level, as long as it is low enough. This is because the adjustment process of Bacmeister and Pierrehumbert (1988) appears to only raise the critical

level from its initial position, not lower it. This relative insensitivity due to the adjustment mechanism may mean that the synoptic-scale flow dows not need to be as adequately forecast as in the other downslope wind regimes.

We propose to test this potential difference in predictability through the use of a state-of-the-art mesoscale ensemble initialized every day for a period of 2.5 years. However, from a practical predictability standpoint, even if it is true that downslope windstorms in the presence of a mean-state critical level are less sensitive to the synoptic scale flow, there is still not necessarily a guarantee that the ensemble is able to produce synoptic conditions that are "close enough" to the actual state of the atmosphere to predict the proper windstorm response. In order to assess this question, we also need information about the true state of the atmosphere. For this purpose, we make use of observational data from Mesowest, a database and data access provider of observational data from various networks in the United States (Horel et al., 2002).

We will assess the relative predictability of different types of windstorm events within the context of the numerical forecasts by comparing the ensemble spread for each type of event. We will also compare the ensemble forecasts against observations, assessing both the probability of correctly predicting events and the rate of false alarms. In addition, we will consider how forecasting performance depends on the fraction of ensemble members that forecast windstorms. To do this, we will test criteria for issuing a warning based on the number of ensemble members that predict a windstorm and apply this forecast procedure to 2.5 years of data at 15 observing stations in the western US.

3.2 Methodology

3.2.1 NCAR Ensemble Description

The NCAR ensemble was a real-time convection allowing ensemble designed and run by the National Center for Atmospheric Research from 7 April 2015 to 30 December 2017. The ensemble was initialized at 00 UTC each day and integrated to a model time of 48 h. The

ensemble consisted of 10 WRF-ARW members run at 3 km horizontal resolution over the continental United States.

All variation among the ensemble members was produced by varying the initial conditions; the dynamical core configuration and parameterization choices remained fixed among the ensemble members. Ensemble perturbations were generated from a continuously cycling Ensemble Kalman Filter (EnKF). Eighty (initially 50 until 2 May 2016) ensemble members with 15-km horizontal resolution were utilized in the data-assimilation system. These members were updated every 6 hours by assimilating a quality-controlled observational dataset. Every 24 hours, at 00 UTC, 10 of the members were downscaled to 3-km horizontal resolution and used to initialize the 48-hour forecasts (Schwartz et al., 2018).

Output from all ensemble members is archived at NCAR, but not all fields are available. In particular, much archived output relates to convective indices useful for forecasting severe thunderstorms, and many of the three-dimensional variables have either been omitted or are at too coarse resolution in the vertical to be of use. Therefore, we have necessarily restricted our analysis to 10-meter wind speed, which is output at a time resolution of 1 hr.

The configuration of the ensemble is such that there are two ensemble forecasts for every forecast time within the verification period: one forecast from the ensemble initialized at 00 UTC of the forecast day and one forecast from the ensemble initialized at 00 UTC the day before. Therefore, for each forecast time, there are 20 verifying ensemble members: 10 from each of the two forecasts. However, the lead times for these forecasts necessarily vary throughout the day from as short as 1 hr and 25 hr in the case of a forecast for 01 UTC to as long as 24 hr and 48 hr for a forecast for 00 UTC. (Technically, there is an ensemble forecast with a lead time of 0 hr, but since the analysis is not useful for forecasting purposes or for analyzing predictability, we have omitted it.)

This varying lead time is a potential complication. One could envision that forecasts for 01 UTC may show more predictability than forecasts for 23 UTC simply because of the shorter lead times. To address this, our analysis of the ensemble spread is conducted as a function of lead time. On the other hand, our other analysis, a forecast evaluation,

includes time periods of both relatively shorter and longer lead times, which should somewhat compensate for this effect.

3.2.2 Station Selection

Stations for the analysis were selected from a filtered Mesowest dataset. For our analysis, we began with several known downslope windstorm susceptible stations. We then attempted to supplement this list through the use of a terrain selection criterion as follows. First, we filtered the list of all Mesowest stations in the western United States and Canada to only retain stations potentially susceptible to downslope windstorms though the use of a GIS analysis of the terrain.

The GIS terrain analysis was computed using ESRI's ArcGIS software package, while all topographic data was obtained from the United States Geological Survey through their Three-Dimensional Elevation Program (3DEP) dataset (Sugarbaker et al., 2014). Since the ArcGIS software is limited to one computer without significant financial and human investment in the parallel processing configuration, this analysis was limited to the western United States and Canada, specifically inside a box extending from 32° N to 53° N and from 103° W to 125° W. This region captures most of the expected downslope windstorm susceptible regions of the United States and Canada while still remaining small enough to be computationally tractable on one machine.

The 3DEP dataset is provided at 1 arc-second (1/3600 degree) resolution in tiles of size 1 degree by 1 degree. For computational cost reasons, all computations described below are applied to each tile individually.

Various methods were utilized to filter the USGS dataset to obtain potential downslope windstorm sensitive regions. While all methods are objectively applied to the entire dataset, various thresholds must be set, most of which were determined subjectively to include previously well-known regions susceptible to windstorms. These terrain analyses are guided by the question, "Which areas are located near the base of major mountain slopes?"

To answer these questions, we make use of both a local slope analysis as well as a more

large-scale metric. The local slope of the terrain is computed using the ArcGIS Terrain Slope function. This function computes the slope in geodesic coordinates, i.e. taking into account the map projection. We define large slopes to be to be 15% or greater.

However, we desire regions that are close to the base of mountain slopes but are not high on the slopes themselves. Therefore, we compute the intersection of the points that are within 2 km of the region of high slope but also have a slope less than 5%. This can be thought of as points being in the plains immediately next to mountain ridges.

The large scale metric is designed to remove steep but small ridges that are unlikely to generate significant downslope flows. If there is an elevation change of 500 m within 2 arc-minutes of a point, that point is determined to have satisfied the large-scale criterion. This criterion was implemented through the use of the ArcGIS FocalStatistics function. Both the small- and large-scale criteria are shown in Fig. 3.1 for a mountain ridge in northeastern Nevada. Stations were selected from the region composing the intersection of the two criteria.

Stations satisfying both the small- and large-scale criteria were selected for the downslope windstorm analysis. After a list of suitable stations were identified, the station list was pared down to a manageable size as follows. First, the stations were ranked according to a criterion corresponding to the total number of hours with gusts above $20\,\mathrm{m\,s^{-1}}$. The criterion is given by

$$h_g = \int_0^t g\left(\alpha\right)\ d\alpha, \tag{3.1}$$

where

$$g(t) = \begin{cases} 0, & |\mathbf{u_g}| < 20\,\mathrm{m/s} \\ 1, & |\mathbf{u_g}| \geq 20\,\mathrm{m/s}. \end{cases} \tag{3.2}$$

Here h_g is the criterion, $|u_g|$ is the magnitude of the wind gust vector, and α is a dummy integration variable. The integral was evaluated using the trapezoidal rule. Use of the integral, as opposed to metrics such as simply counting the number of data points above the threshold, allows for a better comparison between stations which report data at different intervals. Various thresholds for this criterion were evaluated; $20\,\mathrm{m\,s^{-1}}$ was chosen quali-

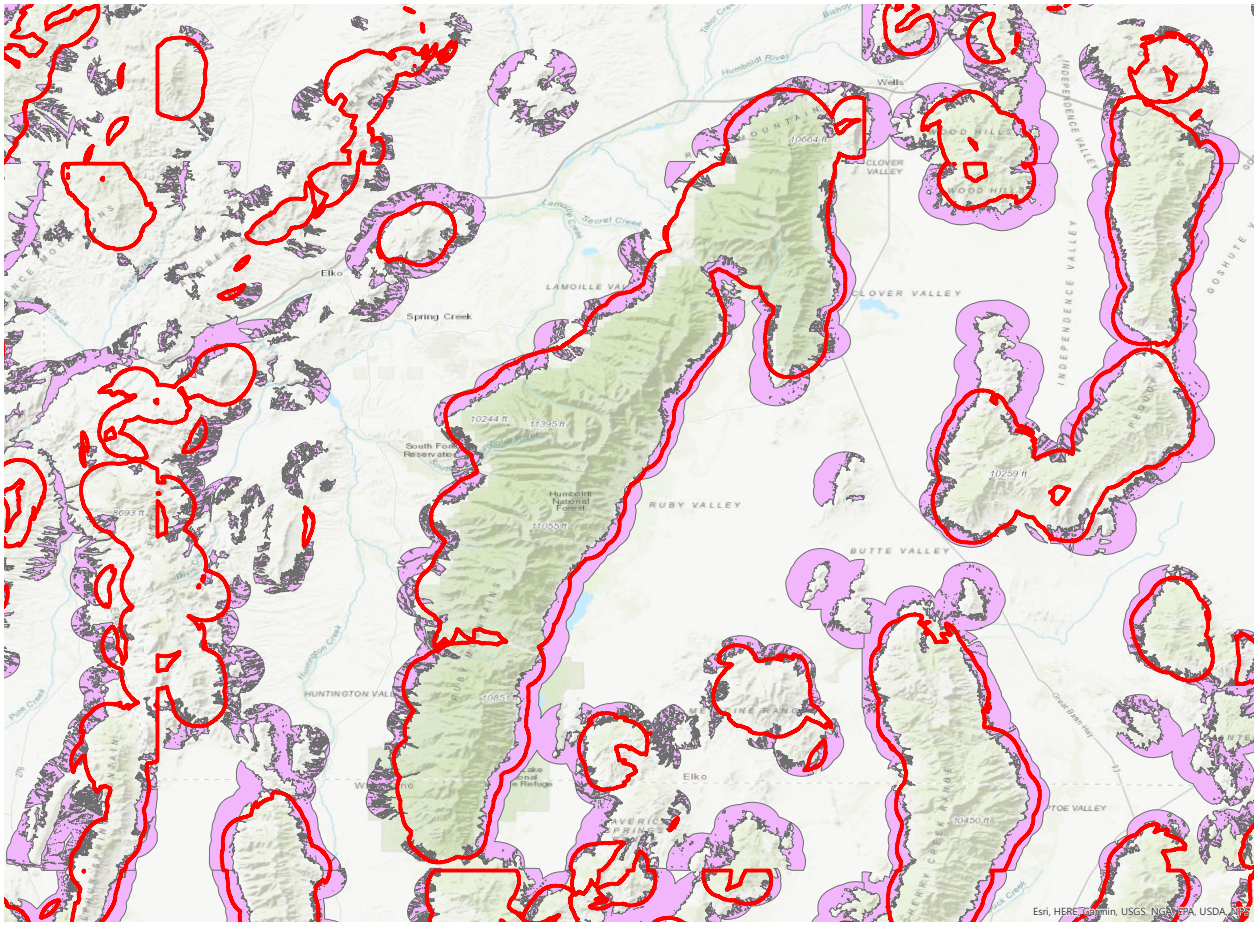

Figure 3.1: Regions satisfying the small-scale criterion (purple color fill) and the boundary of the large-scale criterion (red contour).

tatively as a threshold which gives a large enough sample set but yet is not too low as to represent inconsequential wind speeds.

Stations with the highest values of this criterion were, in general, chosen for the analysis. However, some quality control was required. While Mesowest does perform some automated quality control (Horel et al., 2002), there were still remaining issues with data from certain stations. Further quality control was conducted by manually examining the time series and qualitatively determining whether obvious errors were present.

Once stations with obvious bad data were removed from consideration, further manual examination was conducted to ensure that most of the winds were indeed due to downslope events. The terrain was examined for two main considerations. The first was to ensure that the high wind flow was indeed in a direction corresponding to downslope flow, while the second was to ensure that the station was not located at the mouth of a valley or other such terrain feature, which ensures that the strong wind events were not related to gap flow type phenomena.

Our resulting list of stations includes 15 stations across the western United States. While most are in locations well-known to be susceptible to downslope windstorms, several are in locations not as well recognized. For example, our analysis includes a station in West Texas that experiences downslope flow from the Guadalupe Mountains and a station in eastern Washington that experiences downslope flow from a ridge near the Hanford Site. Stations located in well-known windstorm-susceptible locations include stations near Boulder, Colorado, Centerville, Utah, and stations in San Diego County, California. A full list of stations, including the direction of the mountain-normal vector, is provided in Table 3.1. The location of these stations is shown in Fig. 3.2. The location of these stations relative to the terrain, as well as the mountain-normal vector, is shown for stations on the east side of mountain ranges in Fig. 3.3; the corresponding figure for west-side stations is shown in Fig. 3.4.

All of these stations have observations of sustained wind and gusts throughout the forecast period of the NCAR ensemble. To determine a model forecast wind speed for comparison with these observations, we find the nearest two grid cells corresponding to the location of

Mesowest Station ID	Location	Mountain Normal Direction (°)	Mean Bias (m/s)
CO109	Boulder, CO	270	3.3
NWTC	Boulder, CO	270	-2.0
SRNNV	Sierra Nevada Mountains, NV	230	-5.6
PSGT2	Guadalupe Mountains, TX	311	3.0
GALN2	Sierra Nevada Mountains, NV	277	5.2
IDPC1	Owens Valley, CA	268	3.9
WSM16	White Sands Missile Range, NM	294	-5.9
HEOC	Hanford Site, WA	213	-8.1
RBYNV	Ruby Mountains, NV	304	1.9
CEN	Centerville, UT	90	10.0
UP138	Centerville, UT	90	6.1
AP611	Centerville, UT	90	4.9
SILSD	San Diego County, CA	99	-4.8
HP016	San Diego County, CA	80	-5.0
WSM39	White Sands Missile Range, NM	61	-8.0

Table 3.1: List of the 15 selected stations by Mesowest ID and general location. The direction of the mountain normal vector and mean bias at each station is also provided.

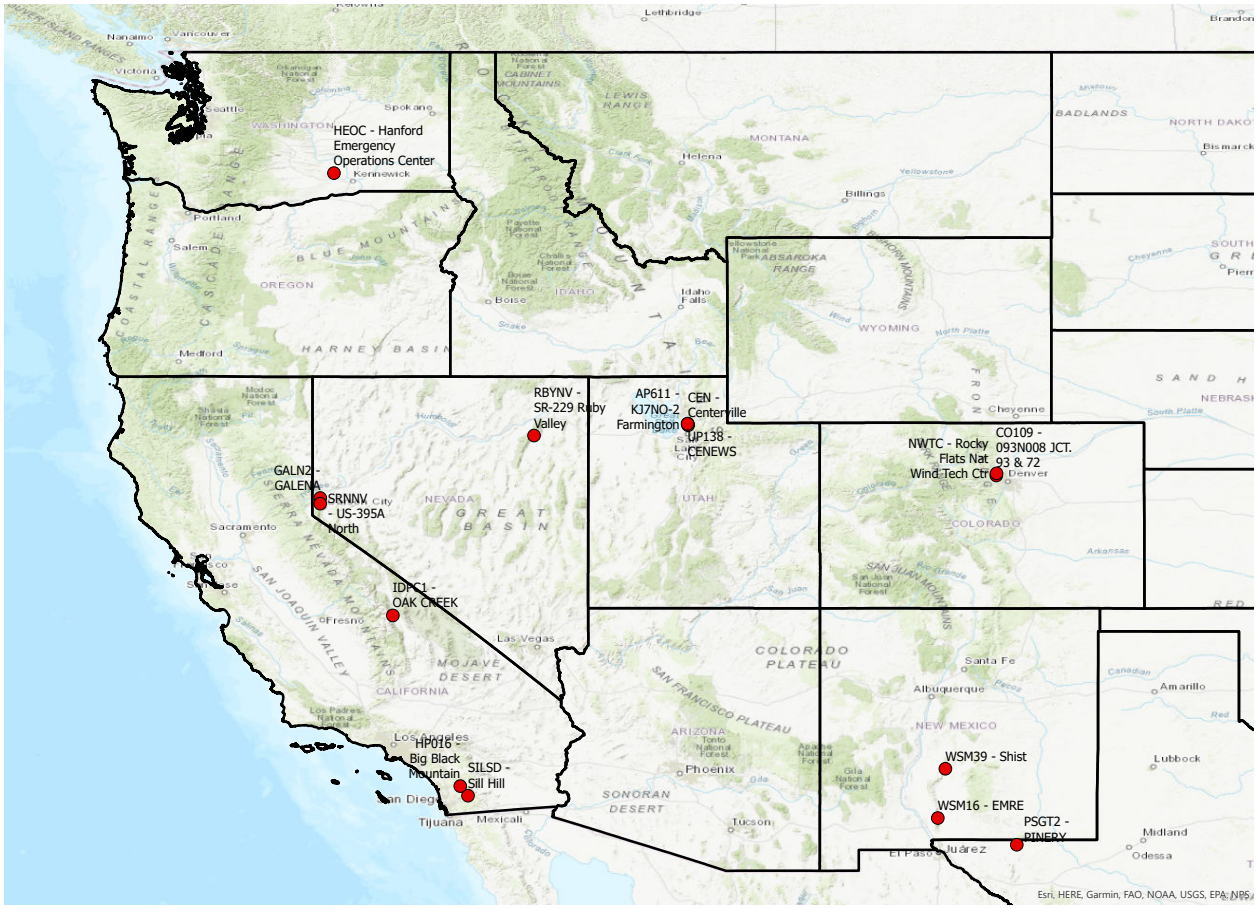

Figure 3.2: Location of the 15 selected observation stations in the western United States.

the observation station. Then, for each ensemble member, we take the wind components from the point with the greatest vector Euclidean norm. Use of the two-point metric allows the analysis to not be bound to the values at a single grid cell while still remaining local to the corresponding observation station.

3.2.3 Critical Level Dataset

Unfortunately, the NCAR archive does not contain enough upper level data to determine the presence and height of a critical level. As a proxy for the missing data, we utilize the ERA5 reanalysis dataset from the European Center for Medium Range Weather Forecasts

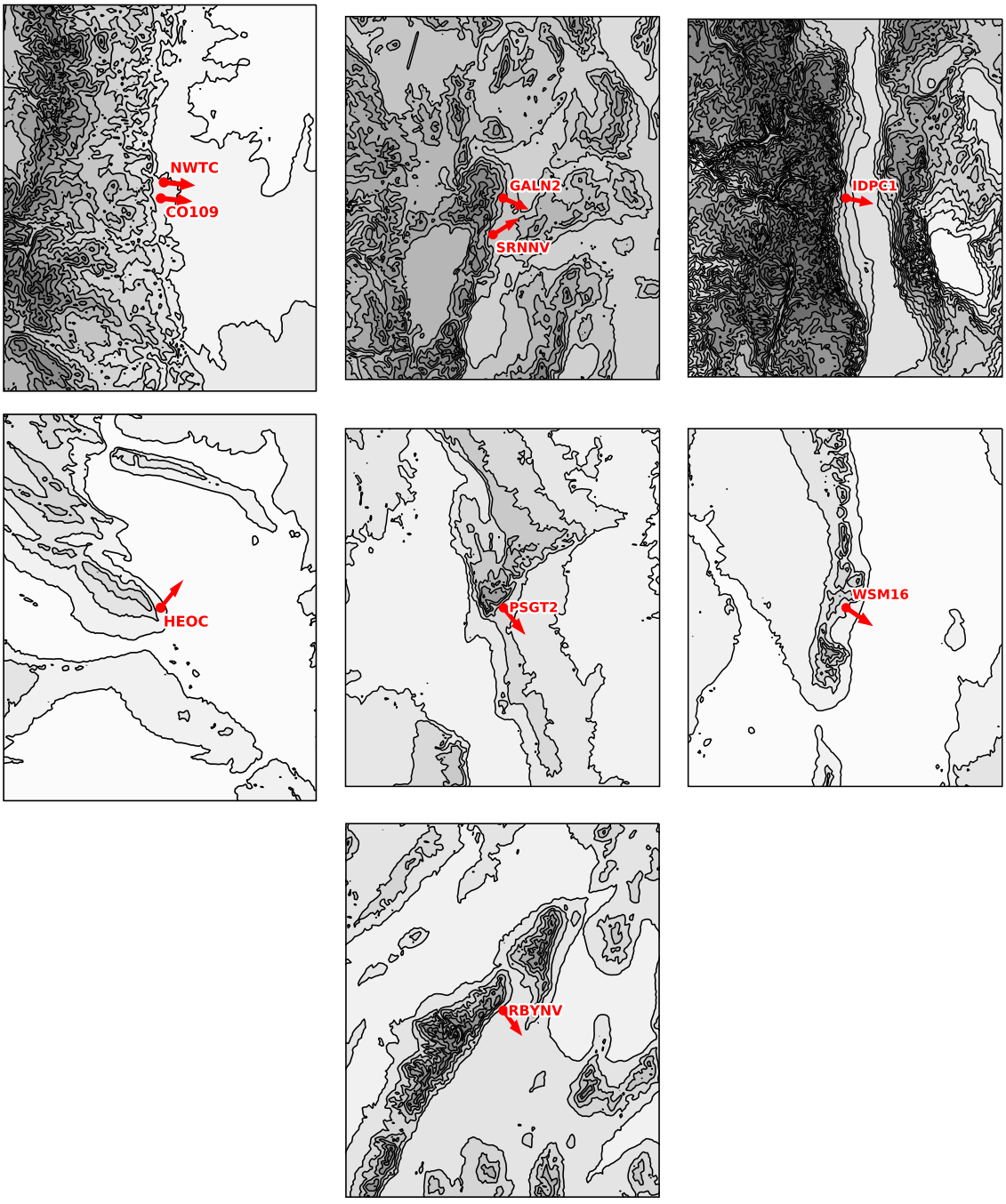

Figure 3.3: Station location relative to terrain for stations on the east side of mountain ranges. Filled contours indicate terrain height, with darker shades of gray indicating progressively higher terrain. Terrain contours are in 250 m intervals. The mountain-normal vector for each station is plotted as a red arrow.

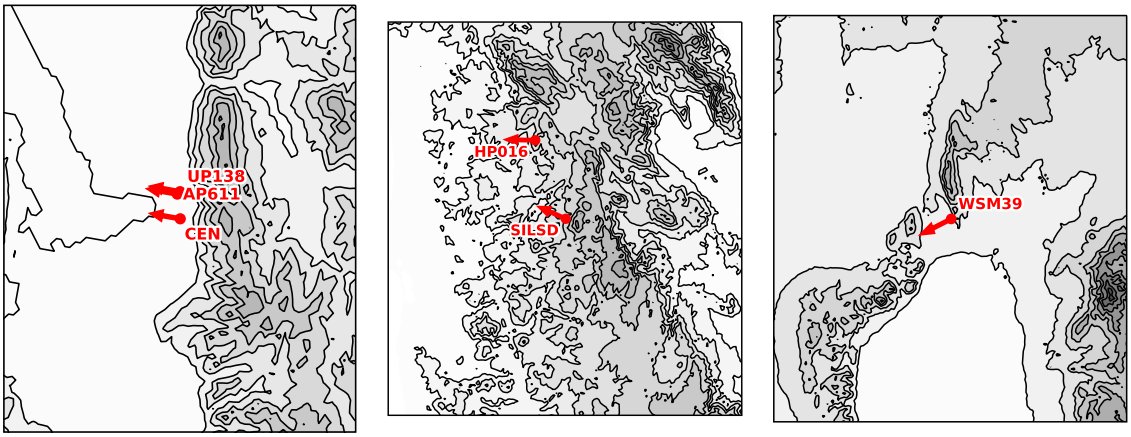

Figure 3.4: As in Fig. 3.3, but for stations on the west side of mountain ranges. The left-most panel is magnified in space by a factor of two for clarity.

(Hersbach et al., 2020). While the ERA5 dataset provides one of the best estimates of the true presence or absence and height of a critical level, it unfortunately is not necessarily representative of the true model state. We are, for example, unable to diagnose critical level properties within individual ensemble members.

One concern is whether or not the critical levels found in the ERA5 dataset are mean-state critical levels or are self-induced by wave motions within the model. The ERA5 reanalysis was conducted using the ECMWF Integrated Forecast System at a horizontal resolution of 31 km (Hersbach et al., 2020). Such a horizontal resolution will not resolve most short-wavelength motions due to mountain waves well, and therefore, it is probable that most of the critical levels found in the dataset are mean-state critical levels.

3.2.4 Bias Correction

Downslope windstorms tend to be gusty events (see, for example, Durran (1990), his figure 4.11). We wish to allow for this variability in our analysis by considering wind gusts, but this introduces a mismatch with the model wind speed, which is more equivalent to the sustained wind speed since it does not include the turbulent motions responsible for producing gusts.

In addition, there are potentially other sources of bias in the model forecasts for each station.

With this in mind, we apply a bias correction to the model forecasts as follows. First, we need to establish an approximate correspondence between the sustained wind speed and the gusts for comparison with the model. To do this, we analyze all downslope observations from all stations with gusts greater than 10 m/s. Downslope observations are defined as being within a ± 45 degree angle of the vector normal to the main mountain ridge. For each observation within these events, we compute the average difference between the sustained winds and the gusts. The resulting computed average difference is 5.73 m/s.

We use the above difference to establish a baseline windstorm definition, which is used to generate a sample set on which to compute the bias. Specifically, we compute the bias on all events with either observed wind gusts of 20 m/s or ensemble wind speeds greater than 15 m/s in at least two ensemble members. The difference in wind speed is motivated by the correspondence established above; the ensemble member threshold is purposely chosen to be relatively non-restrictive. This allows for a large sample size on which to compute the bias.

We bias correct the wind speed at each station individually. The bias itself could be taken to be simply the difference between the ensemble mean wind and the observed wind gust in the direction of the mountain normal vector, but there is a complication. Since the model topography may differ from the actual topography, we employ a slightly more sophisticated procedure designed to account for this. We obtain a wind speed component for both the ensemble mean and the observed gusts as follows. If the wind direction is within the windstorm quadrant (defined above), we simply use the wind speed. If the wind direction is outside the windstorm quadrant, we project the wind velocity onto the mountain normal vector and use the resulting speed. This procedure allows us to account for some difference due to mismatch in the topography while still accounting for cases with significant difference in wind direction. After using this procedure to obtain wind speeds for both the ensemble and observations, the resulting bias is computed as the ensemble wind minus the observed wind. Resulting average biases for each station are provided in Table 3.1.

Example time series after bias correction for two stations, CO109, in Boulder, Colorado,

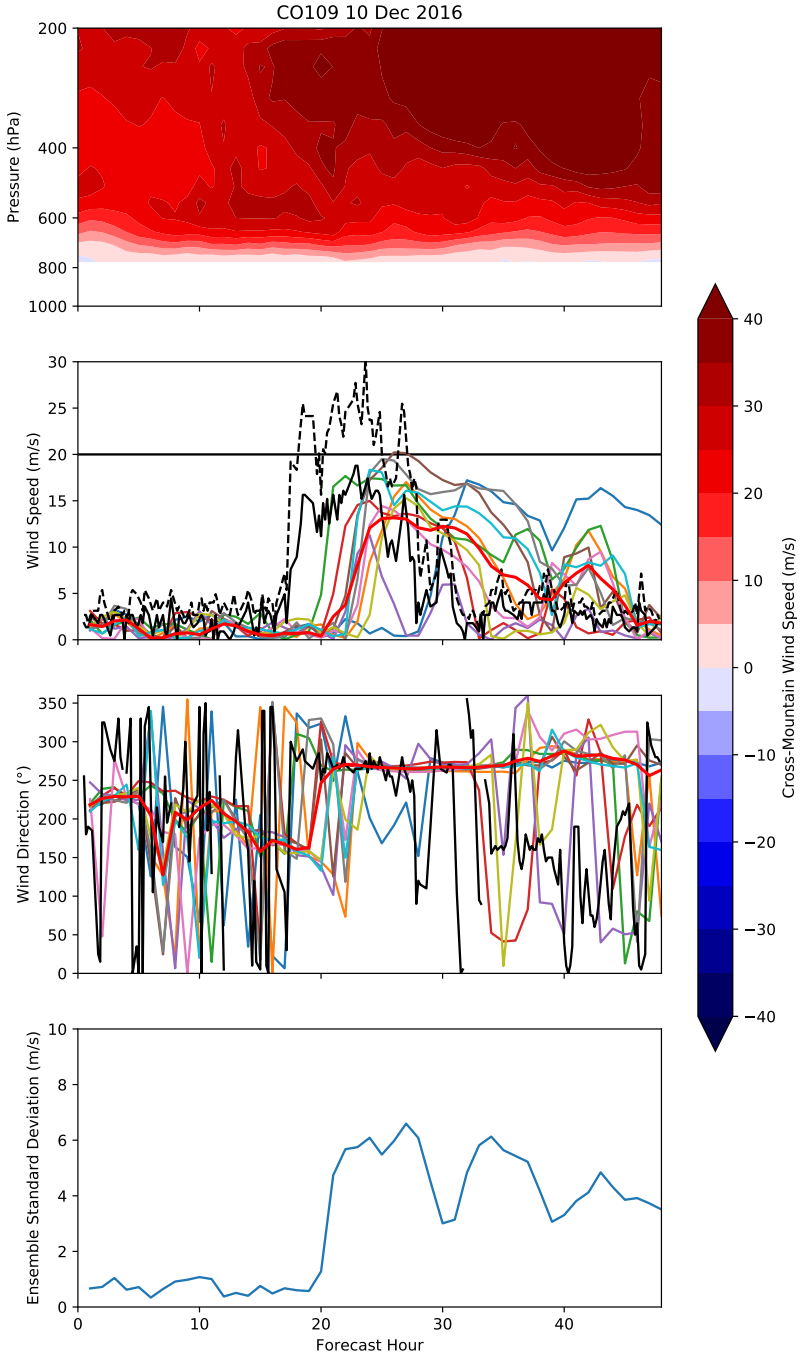

Figure 3.5: Relevant windstorm parameters for station CO109 in Boulder, CO. From top to bottom: Cross-mountain wind-component (color fill) and critical level height (when present, dashed); ensemble wind speed (thin colored curves), mean ensemble wind speed (thick solid red curve), and observed sustained winds (solid black curve) and gusts (dashed black curve); as in the panel above, but for wind direction; and standard deviation of the ensemble members. Winds below mountain-top height are not plotted (white area) in the top panel.

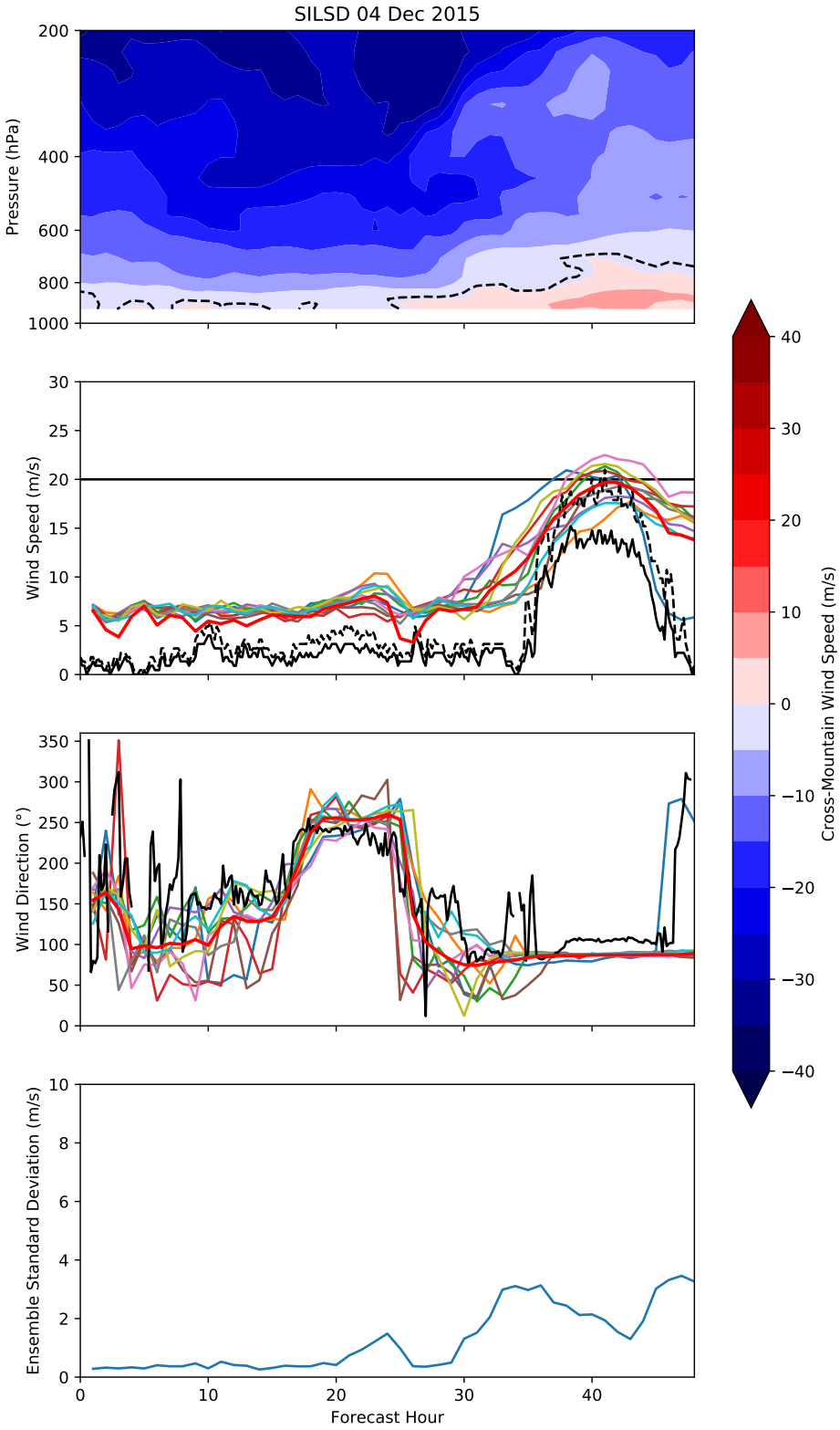

Figure 3.6: As in Fig. 3.5, but for Sill Hill, CA (SILSD).

and SILSD, in San Diego County, California, are shown in Figs. 3.5 and 3.6. The top panel shows the upper-level flow in the cross-mountain direction from ERA5. The sign is chosen so that the downslope flow direction is positive; therefore, negative values indicate the values of a critical level. The location of a critical level, determined using the criterion described above, is shown as a black dashed line. Note the absence of a critical level throughout the time series of CO109, while one is always present for the SILSD case.

The middle two panels illustrate the wind speed and wind direction, respectively. When ensemble members have strong downslope flow, there is very little variation in the wind direction between those members. In contrast, the observed winds exhibit slightly larger variation, perhaps in conjunction with the more complex topography found in the real world. One other important note is found in the time series of wind speed for SILSD. Note that the base wind speed for forecast hours 1-24 is approximately 6 m/s. This is an artifact of the bias correction; those wind speeds have been increased since SILSD was on average negatively biased. However, note that, for this case, the windstorm is quite well forecast. This amplification of the baseline wind speed is a consequence of bias correcting for high wind events; however, it has no impact on our analysis as a 6 m/s wind speed is treated the same as a 0 m/s wind. Neither is classified as a windstorm.

The time series of wind speed at CO109 (second panel in Fig. 3.5) indicates a timing error in the forecast of the windstorm. For the forecast verification, we allow for some timing error in the forecast by sorting both observations and ensembles into bins. This is discussed in further detail below. We also examine the impact of the forecast verification window size, i.e. the maximum allowable timing error, on the verification statistics.

Finally, the ensemble standard deviation, which is one measure of spread, is shown in the bottom panel. There is very little spread prior to the windstorm in both cases; however, the spread increases once a windstorm is present, as expected. In this instance, the spread in the no-critical-level case is greater than that of the critical-level case. This result holds in general, but not to a significant degree, as will be shown in the full spread analysis.

3.2.5 Ensemble Spread

Ensemble spread is often used as one metric for predictability. It is also used in one method for determining whether an ensemble is well calibrated (Fortin et al., 2014). There are two methods used to compute the average ensemble spread: the first is to take the average over all forecasts (at a given lead time) of the standard deviations of the ensemble members for each forecast, while the second is to use the square root of the average variance of the ensemble members. Mathematically, the first definition is given by

$$\frac{1}{N}\sum_{j=1}^{N}\sqrt{\frac{1}{n-1}\sum_{i=1}^{n}(u_{j,i}-\bar{u}_j)^2}, \tag{3.3}$$

while the second definition is given by

$$\sqrt{\frac{1}{N}\sum_{j=1}^{N}\frac{1}{n-1}\sum_{i=1}^{n}(u_{j,i}-\bar{u}_j)^2}. \tag{3.4}$$

Here, n is the number of ensemble members, N is the number of verification times, $u_{j,i}$ is the wind speed of the i-th ensemble member at verification time j, and $\bar{u}_j$ is the ensemble mean wind speed at verification time j. Note that the difference between the two metrics lies in when the square-root operator is applied.

As Fortin et al. (2014) notes, these metrics are similar, but not equivalent. In fact, only the second method is valid for determining whether or not an ensemble has the proper amount of spread. However, the first metric does have one advantage: it is the mean of some sample, namely that of the standard deviations of the ensemble members, and therefore it is more natural to compute other corresponding summary statistics, such as the standard deviation and resulting confidence intervals of the standard deviation distribution.

We therefore make use of both of these definitions of spread. We use the first definition to perform a statistical analysis of the spread in order to determine whether or not the difference in spread between no-critical-level and critical-level cases are significant. However, for comparison with the root-mean-square-error of the ensemble, we use the second definition,

as is proper per Fortin et al. (2014), although it should be noted that this measure was first defined by Leith (1974) and Murphy (1988).

We are interested in the ensemble spread of wind speed. However, we are only interested in the spread for windstorm events, and therefore we need to define a windstorm subsample of the full datasets. For this purpose, we use a superset of both the observed and forecast windstorms, where the observed windstorms were defined to have gusts greater than 20 m/s, and the ensemble windstorms were defined to have at least two ensemble members with bias-corrected wind speeds greater than 20 m/s. Using thresholds related to individual ensemble members instead of an overall summary statistic like the ensemble mean is motivated by the presence of a bifurcation response in the results of Doyle and Reynolds (2008) and others; ensemble members tend to have either a high wind state or a minimal response. The ensemble mean in this instance is unrepresentative of either the members with a windstorm or those without.

3.2.6 Forecast Evaluation

For the purposes of forecast evaluation, the data are sorted into 6 hr bins. Results for bin sizes of 3 and 12 hr were also computed. As will be shown later, the results and conclusions are not sensitive to the choice of the bin size. Sorting both observations and forecasts into bins allows for some mismatch in the timing of events between the model and observations.

We define binary success criteria (i.e. either a hit or a miss) for both observations and ensemble forecasts as follows. For observations, if the maximum wind gust inside a bin exceeds a given threshold, that bin is counted as a windstorm bin. For the ensembles, we define a hit to be a certain number of ensemble members exceeding a threshold. We computed results for ensemble member thresholds between 2 and 18. Note that there are twenty ensemble members in each bin (ten from the forecast initialized at 00 UTC on the day of the bin and ten from the forecast initialized at 00 UTC the day prior).

We also need to categorize each bin by the presence or absence of a critical level. Using the wind field from the ERA5 dataset described above, we take the closest point to the

given station. We then compute the wind component in the cross-mountain direction. Then, we define a critical level as a wind speed of -1 m/s or less in the cross-mountain direction. Although theory dictates that 0 m/s is necessary and sufficient for a critical level, the choice of -1 m/s is made to ensure a more robust critical level is present.

We look for critical levels between the surface and 100 hPa. Critical levels above 100 hPa are quite high and should not have a significant effect on the mountain wave and development of a downslope windstorm below. Therefore, it seems more correct to categorize these extremely high critical levels as no-critical-level events. However, we do separate the critical level cases into low- and high-elevation critical-level cases, using a cutoff mean critical level height of 8 km above ground level, which corresponds to the cutoff height chosen in Nance and Colman (2000). If more than half of the times in the bin exhibit critical levels, we designate the bin a critical-level bin.

We use standard analysis metrics on each bin to evaluate the forecast performance. Specifically, we use the probability of detection (POD), false alarm ratio (FAR), and critical success index (CSI). These metrics have been utilized in many previous analyses of various forecasting problems, including, for example, tornado forecasting (Brooks and Correia, 2018; Schaefer, 1990).

Defining a to be the number of bins where both the ensemble and observations recorded a forecast (true positives), b to be the number of bins where the ensemble forecast a windstorm but none was observed (false positives), and c to be the number of bins where the ensemble did not forecast a windstorm but one was observed (false negatives), the probability of detection is defined by

$$\mathrm{POD} = \frac{a}{a+c}. \tag{3.5}$$

Similarly, the false alarm ratio and critical success index are defined by

$$\mathrm{FAR} = \frac{b}{a+b} \tag{3.6}$$

and

$$\mathrm{CSI} = \frac{a}{a+b+c}, \tag{3.7}$$

respectively. Simply put, the POD is the ratio of all successfully forecast windstorms to all observed windstorms, and the FAR is the ratio of all false alarms to all forecast windstorms. The CSI, which can also be expressed as a combination of POD and FAR, is maximized when POD = 1 and FAR = 0, corresponding to a perfect forecast with no false alarms. Therefore, it represents one possible method of objectively combining the two previous metrics.

3.3 Results

3.3.1 Ensemble Spread

Taking ensemble spread as an indicator of predictability, we compare the average ensemble spread for no-critical-level (no-CL), low-critical-level (low-CL), and high-critical-level (high-CL) events. The spread for these events, plotted as a function of lead time, is shown with 95% confidence intervals in the top panel of Fig. 3.7 and unsurprisingly increases as the lead-time of the forecast increases. However, there is a approximately diurnal quasi-periodic variation superimposed on the trend in the low-CL events that is not present in either the high-CL or no-CL events. This quasi-periodic variation results in times where the average spread for low-CL events is greater than the no-CL events. This occurs at forecast times around 24 and 48 hr. On the other hand, the average spread of the low-CL cases is lower than the no-CL cases around 12 and 36 hr. At longer lead times, the high-CL cases exhibit lower average spread than either the no-CL or low-CL events. However, at shorter lead times, the difference in average spread between low- and high-CL events is more equivocal.

The difference in average ensemble mean (the third panel in Fig. 3.7) between the no-CL and CL events raises the question as to whether the *relative* ensemble spread is higher for CL events or if the spread is greater simply due to the larger average magnitude of the wind speed for the CL events. One way to determine this is to simply scale the spread by the average ensemble mean for each regime. The results of this adjustment are shown in the second panel of Fig. 3.7. Doing so does not significantly change the conclusion, but there is now often a statistically significant separation between the no-CL and high-CL cases. This

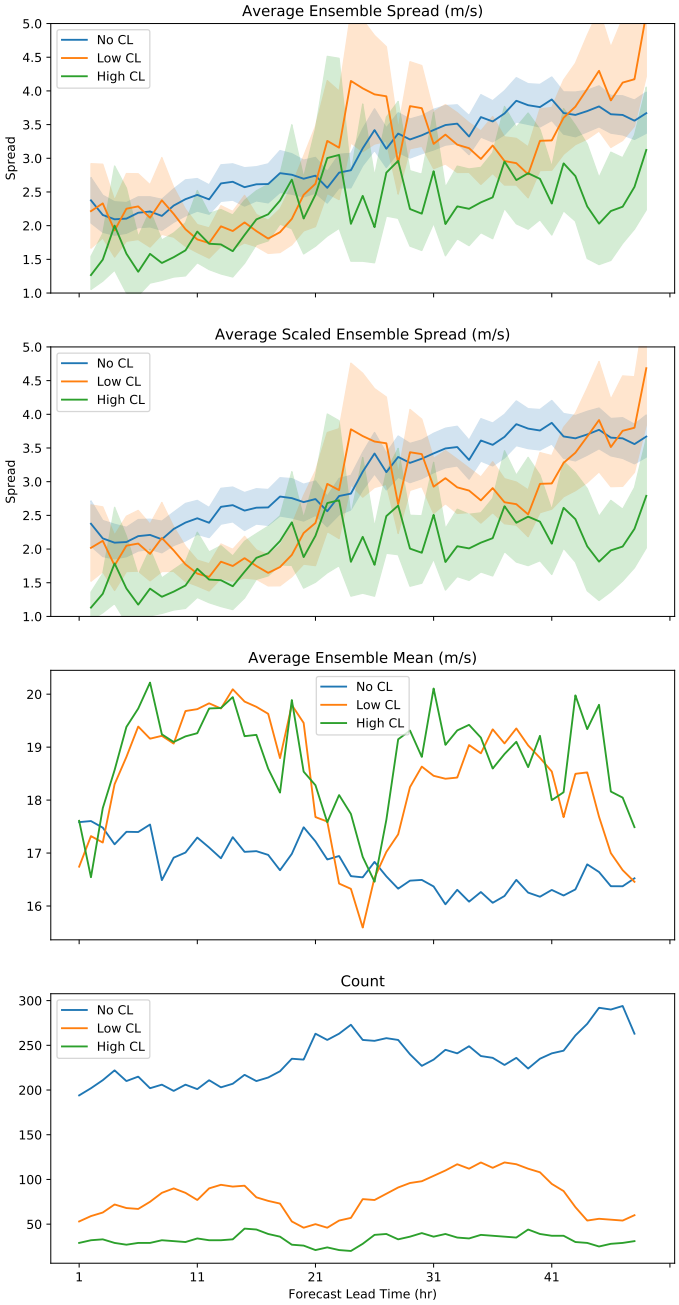

Figure 3.7: From top to bottom: average ensemble spread and 95% confidence intervals as a function of lead time for no-CL events (blue), low-CL events (orange), and high-CL events (green); average ensemble spread scaled by the average ensemble mean; the average ensemble mean as a function of lead time and critical level presence/height; and the number of data samples as a function of lead time and critical level presence/height.

occurs for most lead times, with the exception of a cluster of lead times around 24 hr. This may indicate some potential enhanced predictability for the high-CL events in relation to the no-CL events and some longer-lead-time low-CL events, but drawing a robust conclusion is complicated by the fairly large set of lead times on which there is not statistically significant separation. One issue is the large size of the confidence interval for the high-CL cases due to the relatively small sample (last panel in Fig. 3.7); a larger sample size would be needed to draw a more robust conclusion.

One important metric for an ensemble prediction system is whether it has the proper amount of spread to encompass the proper range of possible outcomes (Warner, 2010). One method of determining whether an ensemble has the proper amount of spread is to compare the root-mean-square error (RMSE),

$$\sqrt{\frac{1}{N}\sum_{j=1}^{N}(\bar{u}_j - \hat{u}_j)^2}, \tag{3.8}$$

to the ensemble spread (Eq. 3.4). Here, N is the number of verification times, $\bar{u}_j$ is the ensemble-mean forecast for the variable u (in our case, the wind speed component obtained from the procedure described in Section 3.2.4) at verification time j, and $\hat{u}_j$ is the true value of the variable u at verification time j. In this case, the spread must be defined as the square root of the average variance, not as the average of the standard deviation, as shown in Fortin et al. (2014). This result is due to Murphy (1988), who determined that for a perfect ensemble whose members are equally likely to represent the true state of the atmosphere, the mean-square error $\langle e_M \rangle$ (the squared version of Eq. 3.8) over an infinite number of forecasts and the average variance of the ensemble members $\langle S \rangle$ (the squared version of Eq. 3.4) are related by

$$\langle e_M \rangle = \frac{M+1}{M}\langle S \rangle, \tag{3.9}$$

where M is the number of ensemble members. In the RMSE framework, where the square root of Eq. 3.9 is taken, the correction factor becomes $\sqrt{(M+1)/M}$. In our case, $M = 10$, and the correction factor is $\sqrt{11/10} \approx 1.05$.

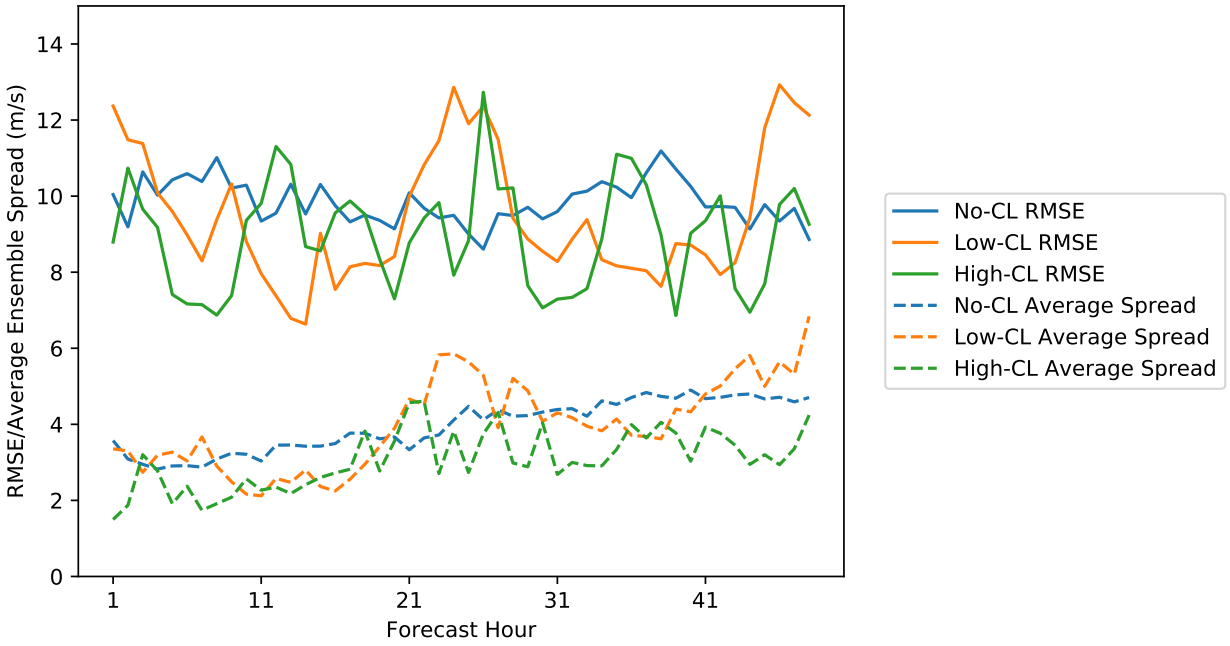

Figure 3.8: Root mean square error (solid) and corrected ensemble spread, calculated as in Eq. 3.4 and multiplied by the correction factor $\sqrt{11/10}$ (dashed), as a function of lead time for the no-CL (blue), low-CL (orange), and high-CL (green) cases. The dashed curves differ from the curves shown in the top panel of Fig. 3.7 in that these curves are the square root of the average variance instead of the average standard deviation.

A comparison of RMSE and spread (multiplied by the appropriate correction factor) for windstorm events, as shown in Fig. 3.8, indicates that the ensemble does not have enough spread for downslope windstorm events. Although this result is specific to the NCAR ensemble, this may be a potential problem in other ensembles as the NCAR ensemble, like all other ensembles known to the author, is not specifically designed to be properly spread with respect to windstorms. Furthermore, a lack of the proper amount of spread for other variables is common in initial condition ensembles (Buizza et al., 2005).

With regard to the RMSE itself as a function of lead time, there is not a significant difference between the no-CL cases and the low- and high-CL cases, although the low- and high-CL RMSE values exhibit greater variation as a function of lead time. The low-CL RMSE exhibits some of the same quasi-diurnal periodic variation as the low-CL ensemble spread, but this variation tends to oscillate around the no-CL RMSE values and is within the range of the high-CL RMSE. Taken together, the low- and high-CL RMSE values vary between 7 m/s and 13 m/s while the no-CL RMSE tends to be confined between 9 m/s and 11 m/s, resulting in a similar average value for all three regimes. Specifically, the mean RMSE over all lead times is 9.84 m/s, 9.47 m/s, and 8.94 m/s for the no-CL, low-CL, and high-CL cases, respectively. Although the CL cases, and particularly the high-CL cases, have a slightly lower mean RMSE over all lead times when compared to the no-CL cases, this is not a particularly significant difference. Finally, and perhaps unexpectedly, the RMSE does not seem to have any significant trend as a function of lead time.

3.3.2 Forecast Evaluation

Fig. 3.9 shows verification results by station for the no-critical-level cases with a windstorm threshold of 20 m/s and a 4/20-ensemble member threshold (i.e., if four ensemble members are greater than the windstorm threshold at any time during the 6-hr forecast period, the bin is considered to have an ensemble forecast windstorm). As expected, the stations on the east side of mountain ranges (names in black) are the most likely to experience downslope windstorms without a mean-state critical level. The forecast accuracy varies significantly

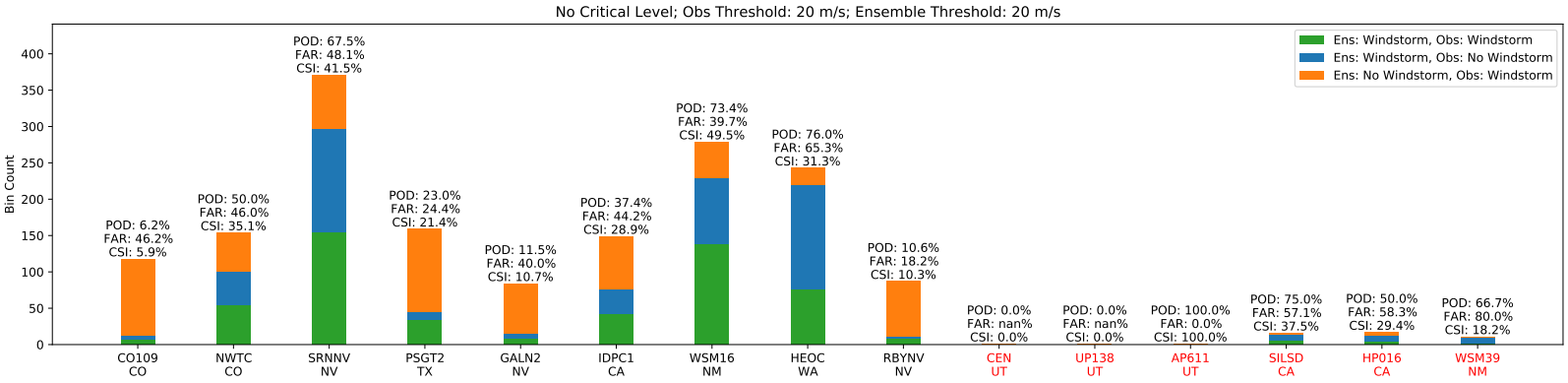

Figure 3.9: Number of no-critical-level bins at each station where the ensemble forecast a windstorm and one was observed (true positives; green), where the ensemble forecast a windstorm and none was observed (false positives; blue), and where the ensemble did not forecast a windstorm and one was observed (false negatives; orange). POD, FAR, and CSI are shown for each station. Station names are printed in black for those stations on the east side of mountain ranges; those on the west are shown in red.

between these stations. For the stations with more than 50 total observed or forecast events, the POD varies between 6.2% and 76.0%, while the FAR varies between 18.2% and 65.3%. This results in quite low CSI overall, with the maximum CSI of 49.5% occurring at WSM16. Overall, even with the bias correction, these results seem to indicate an over-prediction problem. However, as these results are presented for a relatively low threshold of 4/20 ensemble members greater than 20 m/s, it is not surprising that there is over-prediction. We will discuss the impacts of the choice of thresholds in the next section.

Corresponding results for all critical level cases are shown in Fig. 3.10. In general, there are fewer cases with a mean-state critical level, which is not unexpected. However, in contrast to the no-critical-level events, which were essentially non-existent for stations on the west side of mountain ranges, several east-side stations exhibit a fair number of critical-level events. Synoptic charts from some of these events revealed strong troughs resulting in slight reverse flow at upper levels. In addition, three stations located relatively close together near Centerville, Utah, are known to experience strong downslope winds in the presence of a critical level but experienced less than 25 6-hour events within our 2.5-year sample. The critical level events on the east-side stations exhibit low CSI values below 30%.

The source of these low CSI values varies. Four east-side stations have POD values above 35%, including three above 50%, and the low CSI values at these stations largely comes from the high FAR. On the other hand, some stations, such as PSGT2 and RBYNV, have relatively low FAR, and the low CSI values come from low POD. Analysis of the west-side stations is made more complex by the lack of data for the Utah stations. However, for the remaining west-side stations, CSI values are higher, although not significantly so when compared to the no-critical-level events above.

It should be noted that the exact values of the verification metrics are sensitive to the choice of ensemble member threshold. Increasing the ensemble member threshold generally decreases the FAR, but it comes at the cost of a corresponding decrease in POD. This generally results in CSI values that are not significantly better than those for the lower ensemble member thresholds. The impact of ensemble member threshold is discussed more

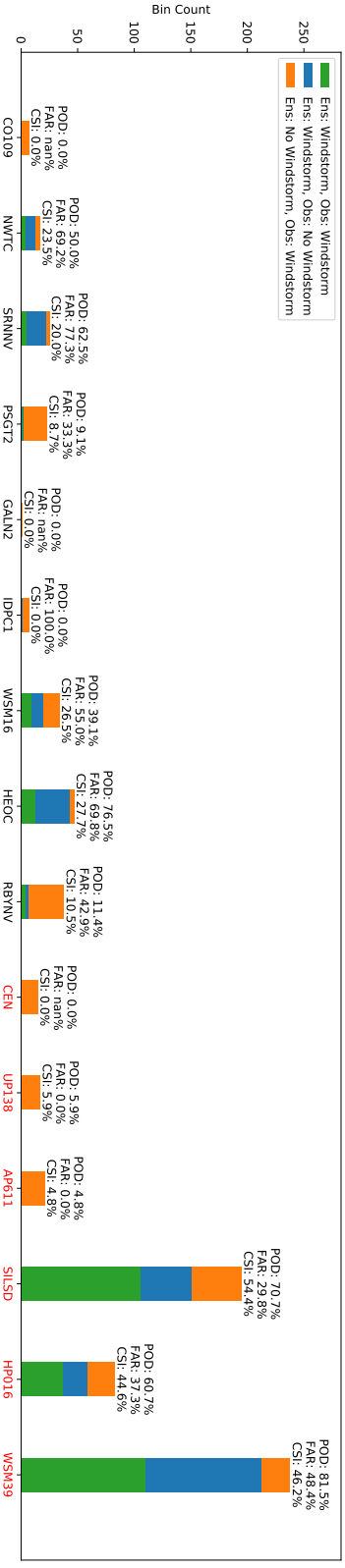

Figure 3.10: As in Fig. 3.9, but for critical level bins.

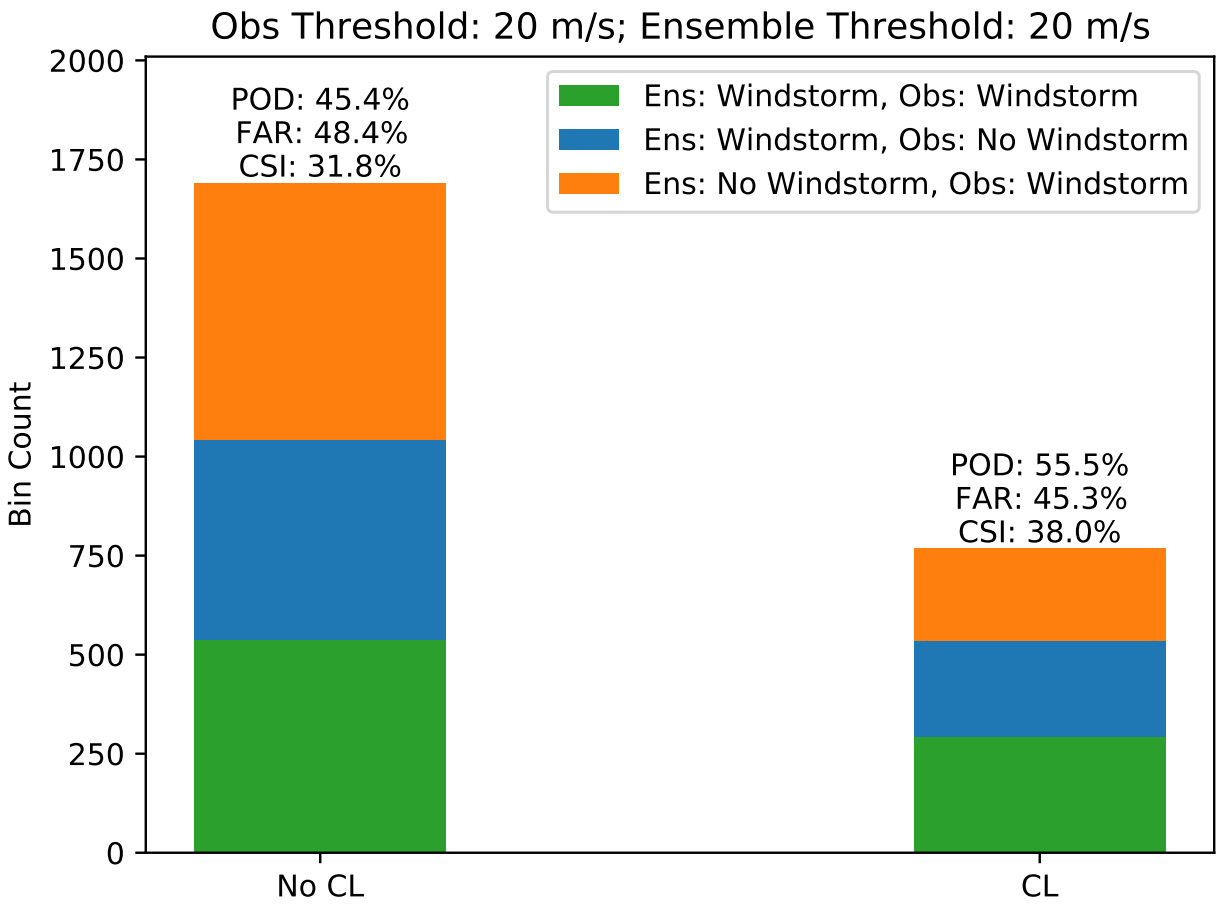

Figure 3.11: Comparison of no-CL and CL events for all stations aggregated together. The meaning of bar colors is equivalent to Fig. 3.9.

fully in conjunction with the aggregated analyses below.

Due to the wide variation in statistics and results between stations, it is hard to draw conclusions that hold for every individual station. However, aggregating all of the stations together and computing statistics only based upon the presence or absence of a critical level reveals a simpler picture. The results from this analysis are shown in Fig. 3.11. When aggregated together, statistics for the no-CL and CL cases are broadly similar. This result is robust across various choices of wind speed thresholds (not shown). At the ensemble

member threshold shown (4/20 members greater than 20 m/s), the probability of detection is relatively high, at 45.4% for the no-CL cases and 55.5% for the CL cases. However, this comes at the expense of a high false alarm ratio of 48.4% and 45.3% for the no-CL and CL cases, respectively. This combination results in rather low CSI values of 31.8% for the no-CL cases and 38.0% for the CL cases. These results are in agreement with previous results, such as Reinecke and Durran (2009) and Doyle and Reynolds (2008), that indicate a quite limited predictability horizon for downslope windstorms. The longest lead-time included in the NCAR ensemble is 48 hr. Having this poor predictability on two-day time scales has unfortunate implications for our ability to forecast windstorms well in advance. Analyzing short (< 24 hr) and long (≥ 24 hr) lead times separately led to no significant differences in the analysis metrics.

Sensitivity to Parameters

Our results are broadly similar regardless of the ensemble member threshold. As shown in Fig. 3.12, increasing the threshold from 2/20 to 8/20 ensemble members increases the CSI for the critical level cases, but this comes at the expense of a significant decrease in the POD. In contrast, increasing the threshold does not have a significant impact on the CSI for the no-critical-level cases, because the POD and FAR fall more and less quickly, respectively, than in the CL case. Above the 8/20 threshold, the CSI continues to drop for both the CL and no-CL cases, although the CL CSI remains higher than the no-CL CSI. At the higher thresholds, the difference in CSI is almost entirely due to differences in POD as there is essentially no difference in FAR between the no-CL and CL cases for thresholds of 12/20 and above. Although there is a significant difference in CSI between the no-CL and CL cases at higher thresholds, sometimes above 10 percentage points, this occurs at thresholds high enough to result in much lower values of POD, which limits the practical utility of these results. Therefore, the difference in CSI at higher thresholds, although interesting, does not result in a significant practical difference in predictability between the no-CL and CL cases.

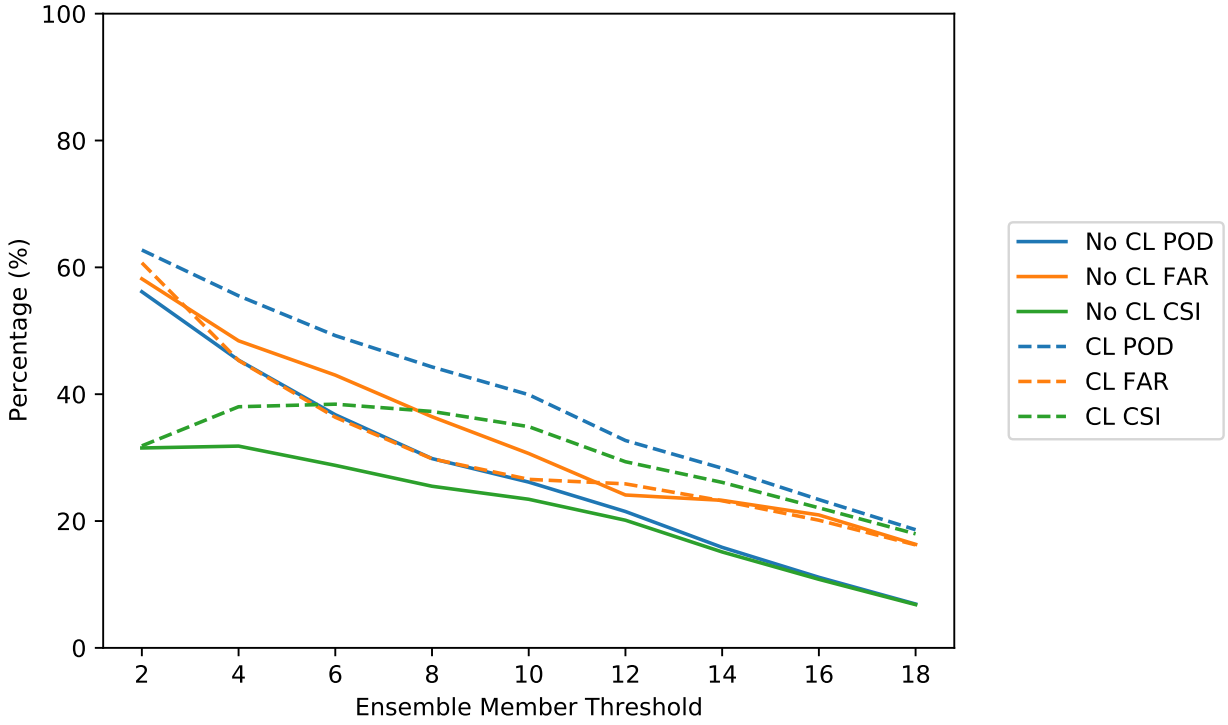

Figure 3.12: POD (blue), FAR (orange), and CSI (green) as a function of ensemble member threshold for the no-CL (solid) and CL (dashed) cases.

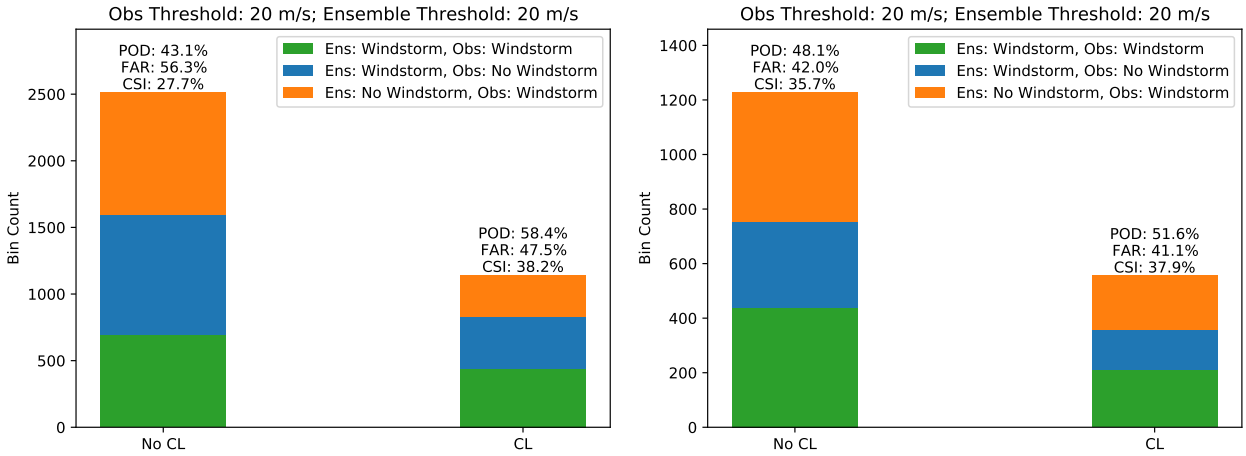

(a) Verification window: 3 hr

(b) Verification window: 12 hr

Figure 3.13: As in Fig. 3.11, but for verification windows of 3 and 12 hours.

For our cases, the 4/20 threshold appears to be the best performing. Above this threshold, the CSI drops for the no-CL cases, while it remains relatively constant for the CL cases. It is for this reason that the 4/20 threshold was chosen for Figs. 3.9-3.11 and also for Figs. 3.13-3.14. One key takeaway from this result is the the best performing (in terms of CSI) threshold represents only 1/5 of the total ensemble members predicting a windstorm. Although the exact threshold is necessarily specific to the configuration of the NCAR ensemble, this result indicates that waiting for even a majority of the ensemble members to indicate a windstorm before issuing a warning may not deliver the best forecast performance.

Results for forecast verification window sizes of 3 and 12 hr are shown in Fig. 3.13. There is a clear improvement of 8.0 percentage points in the CSI for the no-CL cases when increasing the verification window from 3 hr to 12 hr. However, the CL cases exhibit almost no change at all; the CSI in fact decreased, albeit marginally, by 0.3 percentage points. This may be one area where the CL cases are better forecast; the lack of an significant change in the CL CSI when increasing the verification window size may indicate fewer issues with the correct timing of forecast events.

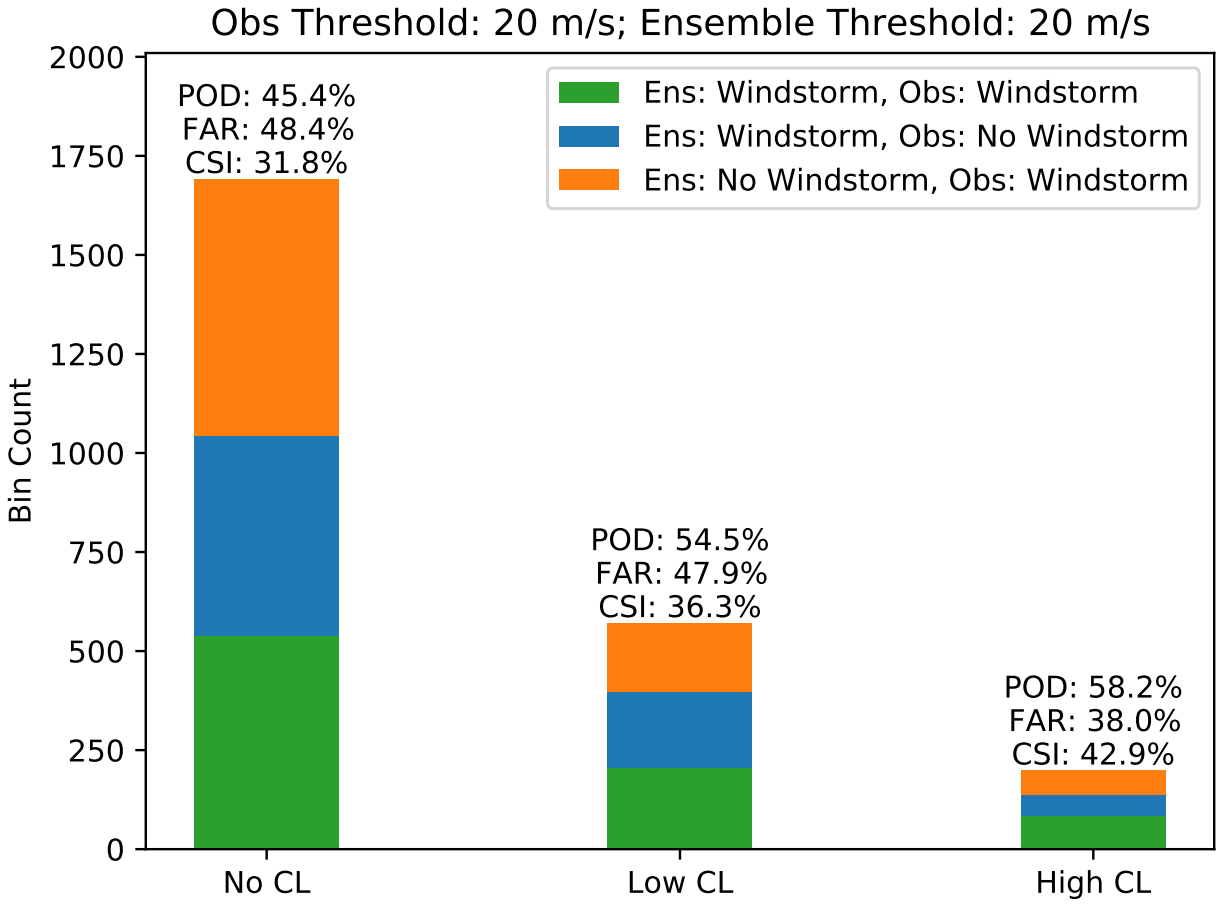

Figure 3.14: As in Fig. 3.11, but with the critical level cases separated into low ($z < 8\,\mathrm{km}$) and high ($z \geq 8\,\mathrm{km}$) cases.

Our ensemble spread results, shown previously, indicate lower ensemble spread for the high-CL cases at longer lead times. If we separate the critical level cases into low- and high-CL bins, as done previously, we find lower FAR for the high-CL cases compared to the no-CL and low-CL cases. However, the POD remains quite similar to the low-CL cases. The corresponding difference in CSI between the low-CL case and the high-CL case is 6.6 percentage points. While this is a fairly large difference, the high-CL CSI values are still quite low to have substantial forecast skill, and thus the height of the critical level is unlikely to be a useful parameter for practical forecasting purposes. Furthermore, there is not an obvious hypothesis for why high-critical-level cases might be more predictable, and much more data and analysis is needed to definitively establish this result.

3.4 Discussion and Conclusions

The availability of the NCAR ensemble archive provided a unique opportunity to analyze the predictability of downslope windstorms with a state-of-the-art high-resolution ensemble. Using 15 downslope-windstorm-prone observational stations across the western United States, we established a windstorm event dataset. We then utilized this dataset to analyze the ensemble spread of the NCAR ensemble to compare the relative predictability of low-CL, high-CL and no-CL events in the context of the numerical forecasts. While there some minor differences between the ensemble spread for high-CL cases compared to others, the signal was not present or statistically significant at all lead times.

The results from our forecast verification analysis led to similar conclusions. The three quantitative metrics for forecast accuracy considered—POD, FAR, and CSI—were often quite similar between the no-CL and CL cases. Although increasing the number of ensemble members required to predict a windstorm before issuing a warning resulted in some improvement in the CSI values for CL cases when compared to no-CL cases, the greatest improvement occurred for relatively high number-of-ensemble-member thresholds. The low POD at these high thresholds results in little practical difference in the predictability of no-CL and CL events.

Our results indicate a continued difficulty with predictability of downslope winds. Despite our focus on lead times less than 48 hr, the quantitative forecast success metrics indicated quite poor forecast success. For comparison, our results for POD, FAR, and CSI are relatively on par with the metrics for NWS tornado warnings, but are significantly worse than that of NWS severe thunderstorm warnings (Brooks and Correia, 2018). On the other hand, the lead time for the downslope windstorm events considered in our analysis is between 1 and 48 hr, while the average lead time for tornadoes and severe thunderstorms is between 15 and 20 minutes. In comparison to the statistics for all NWS high wind warnings, which encompass more than downslope windstorms, our results exhibit lower FAR, but also lower POD (Durran, 2020). However, it should be noted that NWS warnings, although defined by purely objective criteria, are issued by human forecasters; our analysis only considers model data. The influence of human forecasters on verification statistics is a complicating factor outside the scope of this study.

In a comparative sense, then, downslope windstorms appear to have better predictability when compared to other types of mesoscale severe weather due to the much longer lead times. However, even though our analysis only considers forecast lead times less than 48 hours, the maximum POD obtainable from our analysis is approximately 60%, but that comes at the cost of a significant FAR, also with a value of approximately 60%. Although the average lead time is longer than that of severe thunderstorms and tornadoes, this still represents poor forecast skill in the context of preparation for significant impacts from downslope windstorms, such as property damage and fire spread. This relatively poor predictability is in line with previous theoretical results such as Doyle and Reynolds (2008) and Reinecke and Durran (2009), but stands in contrast to some other studies such as Lawson and Horel (2015b) and colloquial forecast evidence. In addition, the apparent increased predictability of mean-state critical-level events in Nance and Colman (2000) did not manifest in our analysis.

The lack of a significant practical difference between non-CL and CL events implies that a different explanation is required to resolve the discrepancy between the short predictability horizons of some studies (including ours) and the apparently long predictability horizons

indicated by other studies and colloquial evidence. While downslope windstorms themselves still appear to have little predictability, other phenomena such as gap flows may be easier to predict. In addition, large-scale downslope flow is responsible for the large areal extent of the Santa Ana winds. Although these large-scale winds do not necessarily reach as strong speeds as true downslope windstorms, their broad extent and capability to bring warm, dry air down into fire-prone areas are still important. Forecast success of fire weather events may be largely to do with the ability to predict these large-scale flows, even if prediction of the exact magnitude and distribution of true downslope windstorms is still difficult. Investigation of the predictability of such larger-scale winds would be an important area for future research.

One other potential avenue of research is whether statistical methods can provide better predictability for downslope windstorms. Such statistical methods include both traditional model-output statistics (MOS) and newer machine learning methods, each of which can incorporate various parameters to obtain a better forecast. We did not pursue this approach because our focus was on *dynamically-driven* sources of enhanced predictability; in other words, whether the presence of the mean-state critical level could, in and of itself, provide enhanced predictability. Nonetheless, for practical forecasting purposes, potential improvements resulting from statistical methods are important to explore.

Whatever the ultimate resolution to the predictability discrepancy, it is clear from these results that downslope windstorms remain a significant forecasting challenge. While an ensemble calibrated specifically for downslope windstorms may better categorize the inherent uncertainty, it does not solve the inherent deterministic forecasting problem. As with so many other phenomena, a probabilistic approach is clearly better suited to the forecasting of downslope winds. Regardless of the presentation of the forecast, however, the limited predictability horizon will continue to complicate forecasts and the public response.

Chapter 4

CONCLUSIONS

Complex topography has many effects on the atmosphere. These effects can be exerted both locally, as in the case of mountain-wave-induced turbulence and downslope windstorms, or remotely, as in the case of gravity wave drag. In this dissertation, we examined both types of phenomena: the impact of finite-amplitude effects on the surface pressure drag and hence the resulting gravity wave drag; and the predictability of downslope windstorms, which are local in scope with their primary effects occurring on and in close proximity to the mountain slope.

Our research on finite-amplitude effects in non-breaking mountain waves revealed significant differences between linear theory and finite-amplitude results, depending on the height of the tropopause and the amount of forward shear present in the background state. These effects have significant implications for the design of gravity wave drag parameterizations, as the current generation of GWD parameterizations use a specified drag at the surface computed by linear theory, which is then propagated upward through the atmosphere using a formulation derived from WKB theory. While more complex phenomena have been incorporated into GWD parameterizations over the years, this fundamental pairing of linear surface drag and WKB-based parameterization has not changed. Therefore, our results suggest there can be significant differences between the true GWD and what would be output from GWD parameterizations.

Since GWD is an important component of the atmospheric circulation, under- or overestimating GWD has significant consequences for the accuracy of weather and climate simulations. Orographic GWD is an important momentum sink, particularly in the Northern Hemisphere, but is also important in the Southern Hemisphere due to the presence of the

Andes, and to a much lesser degree, the Southern Alps. Incorrectly estimating the magnitude of this momentum sink results in incorrect magnitudes for the relevant jet streams and consequently has impacts on cyclogenesis and the propagation of the resulting cyclones.

Therefore, our work recognizes an important limitation in our current formulation of models. Unfortunately, improving GWD parameterizations to account for finite-amplitude effects is difficult without directly simulating the appropriate wave response. Further investigation of different shear profiles may prove useful to determine the degree of sensitivity to the precise shear profile. Adjoint methods may also prove useful to quantitatively determine the sensitivity of the wave response. If the wave response is not highly sensitive to the precise shear profile, there is some possibility that finite-amplitude effects arising due to the presence of shear may be able to be accounted for in GWD parameterization. However, if there is a strong degree of sensitivity, as seems likely, significant improvement in estimates of GWD may have to wait until computing technology allows us to resolve the waves directly with a high degree of accuracy. As of this writing, numerical weather prediction models are approaching the required resolution, but long-duration climate models are still run at resolutions too coarse to directly resolve most of the relevant mountain wave spectrum.

Of course, more direct impacts to communities are caused by the other topic of this dissertation: downslope windstorms. Unfortunately, the results of our examination of downslope windstorm predictability have a similarly pessimistic conclusion: downslope windstorms are difficult to predict, even with a state-of-the-art mesoscale ensemble. Although this conclusion has been reached before, our hypothesis was that different regimes of downslope windstorm generation may have different predictability horizons. In particular, the mean-state critical-level regime was hypothesized to be more predictable than the other regimes, as a dynamical adjustment mechanism exists which allows for downslope windstorm responses to form for a wide range of mean-state critical-level heights.

However, our results indicate that not only are mean-state critical level cases not more predictable, there is little difference in predictive skill between no-critical-level and critical level windstorm regimes. This is somewhat surprising, as the three downslope windstorm

regimes are quite distinct dynamically. Regardless, this has unfortunate implications for downslope windstorm impacts, including both direct property damage due to high winds and indirect impact related to other phenomena such as fire spread.

As a result of the limited predictability, probabilistic forecasts appear to be the best approach for downslope windstorms. Correctly estimating probabilities of downslope windstorm events requires a well-calibrated ensemble. However, as we have shown, the NCAR ensemble was not well calibrated for windstorm events. Running a dedicated ensemble specifically calibrated for windstorm events is likely too resource-intensive for most operational centers, as windstorms are both relatively rare and quite geographically confined. Furthermore, it may not actually be possible to construct such a well-calibrated ensemble. Nonetheless, the important impacts for communities in mountainous regions ensure that downslope windstorms will continue to be an important forecasting challenge.

Mountainous terrain clearly presents many difficulties for accurate weather and climate prediction. First and foremost, the accurate representation of complex topography is important. However, many previous results, including our own, indicate the complex nonlinear nature of atmospheric flows over mountainous terrain. Unfortunately, this has many implications beyond, for example, just accurately representing the structure of mountain waves. The known impact of GWD, and our shown sensitivity of finite-amplitude effects to the background state, indicate that impacts from errors due to inaccurate parameterization can be significant at regional and global scales. In addition, our work indicates that complex topographic flows having significant impacts on mountainous communities will still remain significant forecasting challenges. Although some of our results present rather pessimistic conclusions, particularly in the parameterization space, there are some potential open research questions that may present more hopeful conclusions. Other mountainous phenomena, such as gap winds and large-scale downslope flow, also have significant impacts on mountainous communities and may be more predictable. However, further research would be required to validate those hypotheses. For now, our best options are to account for the errors when possible, push for higher resolution simulations to alleviate the errors caused

due to parameterizations, and take into account the large uncertainty inherent in forecasts of downslope windstorm events.

BIBLIOGRAPHY

Anthes, R. A., Y.-H. Kuo, D. P. Baumhefner, R. M. Errico, and T. W. Bettge, 1985: Predictability of Mesoscale Atmospheric Motions. *Advances in Geophysics*, B. Saltzman, Ed., Issues in Atmospheric and Oceanic Modeling, Vol. 28, Elsevier, 159–202, doi: 10.1016/S0065-2687(08)60188-0.

Bacmeister, J. T., and R. T. Pierrehumbert, 1988: On High-Drag States of Nonlinear Stratified Flow over an Obstacle. *Journal of the Atmospheric Sciences*, **45 (1)**, 63–80, doi: 10.1175/1520-0469(1988)045<0063:OHDSON>2.0.CO;2.

Birner, T., 2006: Fine-scale structure of the extratropical tropopause region. *Journal of Geophysical Research: Atmospheres*, **111 (D4)**, doi:10.1029/2005JD006301.

Blumen, W., 1965: Momentum Flux by Mountain Waves in a Stratified Rotating Atmosphere. *Journal of the Atmospheric Sciences*, **22 (5)**, 529–534, doi:10.1175/1520-0469(1965)022<0529:MFBMWI>2.0.CO;2.

Blumen, W., 1985: Reflection of Hydrostatic Gravity Waves in a Stratified Shear Flow. Part I: Theory. *Journal of the Atmospheric Sciences*, **42 (21)**, 2255–2263, doi:10.1175/1520-0469(1985)042<2255:ROHGWI>2.0.CO;2.

Booker, J. R., and F. P. Bretherton, 1967: The critical layer for internal gravity waves in a shear flow. *Journal of Fluid Mechanics*, **27 (3)**, 513–539, doi:10.1017/S0022112067000515.

Bretherton, F. P., 1969: Momentum transport by gravity waves. *Quart. J. Roy. Meteor. Soc.*, **95 (404)**, 213–243, doi:10.1002/qj.49709540402.

Brewer, M. J., and C. B. Clements, 2020: The 2018 Camp Fire: Meteorological Analysis

Using In Situ Observations and Numerical Simulations. *Atmosphere*, **11 (1)**, 47, doi: 10.3390/atmos11010047.

Broad, A. S., 2002: Momentum flux due to trapped lee waves forced by mountains. *Quarterly Journal of the Royal Meteorological Society*, **128 (584)**, 2167–2173, doi: 10.1256/003590002320603593.

Brooks, H. E., and J. Correia, 2018: Long-Term Performance Metrics for National Weather Service Tornado Warnings. *Weather and Forecasting*, **33 (6)**, 1501–1511, doi:10.1175/WAF-D-18-0120.1.

Buizza, R., P. L. Houtekamer, G. Pellerin, Z. Toth, Y. Zhu, and M. Wei, 2005: A Comparison of the ECMWF, MSC, and NCEP Global Ensemble Prediction Systems. *Monthly Weather Review*, **133 (5)**, 1076–1097, doi:10.1175/MWR2905.1.

Cao, Y., and R. G. Fovell, 2015: Downslope Windstorms of San Diego County. Part I: A Case Study. *Monthly Weather Review*, **144 (2)**, 529–552, doi:10.1175/MWR-D-15-0147.1.

Cao, Y., and R. G. Fovell, 2018: Downslope Windstorms of San Diego County. Part II: Physics Ensemble Analyses and Gust Forecasting. *Weather and Forecasting*, **33 (2)**, 539–559, doi:10.1175/WAF-D-17-0177.1.

Chen, J.-H., and Coauthors, 2019: Advancements in Hurricane Prediction With NOAA's Next-Generation Forecast System. *Geophysical Research Letters*, **46 (8)**, 4495–4501, doi: 10.1029/2019GL082410.

Choi, H.-J., and S.-Y. Hong, 2015: An updated subgrid orographic parameterization for global atmospheric forecast models. *Journal of Geophysical Research: Atmospheres*, **120 (24)**, 2015JD024 230, doi:10.1002/2015JD024230.

Clark, T. L., and W. R. Peltier, 1984: Critical Level Reflection and the Resonant Growth of Nonlinear Mountain Waves. *Journal of the Atmospheric Sciences*, **41 (21)**, 3122–3134, doi:10.1175/1520-0469(1984)041<3122:CLRATR>2.0.CO;2.

Doyle, J. D., C. Amerault, and C. A. Reynolds, 2007: Sensitivity analysis of mountain waves using an adjoint model. *Meteorologische Zeitschrift*, **16 (6)**, 607–620, doi:10.1127/0941-2948/2007/0236.

Doyle, J. D., and C. A. Reynolds, 2008: Implications of Regime Transitions for Mountain-Wave-Breaking Predictability. *Monthly Weather Review*, **136 (12)**, 5211–5223, doi:10.1175/2008MWR2554.1.

Durran, D. R., 1986: Another Look at Downslope Windstorms. Part I: The Development of Analogs to Supercritical Flow in an Infinitely Deep, Continuously Stratified Fluid. *Journal of the Atmospheric Sciences*, **43 (21)**, 2527–2543, doi:10.1175/1520-0469(1986)043<2527:ALADWP>2.0.CO;2.

Durran, D. R., 1990: Mountain Waves and Downslope Windstorms. *Meteorological Monographs*, **23 (45)**, 59–81.

Durran, D. R., 1992: Two-Layer Solutions to Long's Equation For Vertically Propagating Mountain Waves: How Good Is Linear Theory? *Quarterly Journal of the Royal Meteorological Society*, **118 (505)**, 415–433, doi:10.1002/qj.49711850502.

Durran, D. R., 1995: Do Breaking Mountain Waves Decelerate the Local Mean Flow? *Journal of the Atmospheric Sciences*, **52 (22)**, 4010–4032, doi:10.1175/1520-0469(1995)052<4010:DBMWDT>2.0.CO;2.

Durran, D. R., 2010: *Numerical Methods for Fluid Dynamics with Applications to Geophysics*. 2nd ed., Texts in Applied Mathematics ; 32, Springer, New York.

Durran, D. R., 2015a: Downslope Winds. *Encyclopedia of Atmospheric Sciences*, G. R. North, J. A. Pyle, and F. Zhang, Eds., 2nd ed., Elsevier Ltd., 69–74.

Durran, D. R., 2015b: Lee waves and mountain waves. *Encyclopedia of Atmospheric Sciences*, G. R. North, J. A. Pyle, and F. Zhang, Eds., 2nd ed., Elsevier Ltd., 95–102.

Durran, D. R., 2020: Can the Issuance of Hazardous-Weather Warnings Inform the Attribution of Extreme Events to Climate Change? *Bulletin of the American Meteorological Society*, **101 (8)**, E1452–E1463, doi:10.1175/BAMS-D-20-0026.1.

Durran, D. R., and M. Gingrich, 2014: Atmospheric Predictability: Why Butterflies Are Not of Practical Importance. *Journal of the Atmospheric Sciences*, **71 (7)**, 2476–2488, doi:10.1175/JAS-D-14-0007.1.

Durran, D. R., M. O. G. Hills, and P. N. Blossey, 2015: The Dissipation of Trapped Lee Waves. Part I: Leakage of Inviscid Waves into the Stratosphere. *Journal of the Atmospheric Sciences*, **72 (4)**, 1569–1584, doi:10.1175/JAS-D-14-0238.1.

Durran, D. R., and J. B. Klemp, 1982: The Effects of Moisture on Trapped Mountain Lee Waves. *Journal of the Atmospheric Sciences*, **39 (11)**, 2490–2506, doi:10.1175/1520-0469(1982)039<2490:TEOMOT>2.0.CO;2.

Durran, D. R., and J. B. Klemp, 1983: A Compressible Model for the Simulation of Moist Mountain Waves. *Monthly Weather Review*, **111 (12)**, 2341–2361, doi:10.1175/1520-0493(1983)111<2341:ACMFTS>2.0.CO;2.

Durran, D. R., and J. B. Klemp, 1987: Another Look at Downslope Winds. Part II: Nonlinear Amplification beneath Wave-Overturning Layers. *Journal of the Atmospheric Sciences*, **44 (22)**, 3402–3412, doi:10.1175/1520-0469(1987)044<3402:ALADWP>2.0.CO;2.

ECMWF, 2020: Part IV: Physical Processes. *IFS Documentation CY47R1*, No. 4, IFS Documentation, ECMWF.

Eliassen, A., and E. Palm, 1960: Wave energy transfer in stationary gravity waves. *Geofys. Publ.*, **22 (3)**.

Fortin, V., M. Abaza, F. Anctil, and R. Turcotte, 2014: Why Should Ensemble Spread Match the RMSE of the Ensemble Mean? *Journal of Hydrometeorology*, **15 (4)**, 1708–1713, doi:10.1175/JHM-D-14-0008.1.

Grubišić, V., and Coauthors, 2008: The terrain-induced rotor experiment. *Bulletin of the American Meteorological Society*, **89 (10)**, 1513–1534, doi:10.1175/2008BAMS2487.1.

Guest, F. M., M. J. Reeder, C. J. Marks, and D. J. Karoly, 2000: Inertia–Gravity Waves Observed in the Lower Stratosphere over Macquarie Island. *Journal of the Atmospheric Sciences*, **57 (5)**, 737–752, doi:10.1175/1520-0469(2000)057<0737:IGWOIT>2.0.CO;2.

Hersbach, H., and Coauthors, 2020: The ERA5 global reanalysis. *Quarterly Journal of the Royal Meteorological Society*, **146 (730)**, 1999–2049, doi:10.1002/qj.3803.

Horel, J., and Coauthors, 2002: MESOWEST: COOPERATIVE MESONETS IN THE WESTERN UNITED STATES. *Bulletin of the American Meteorological Society*, **83 (2)**, 211–226, doi:10.1175/1520-0477(2002)083<0211:MCMITW>2.3.CO;2.

Kim, Y.-J., and A. Arakawa, 1995: Improvement of Orographic Gravity Wave Parameterization Using a Mesoscale Gravity Wave Model. *Journal of the Atmospheric Sciences*, **52 (11)**, 1875–1902, doi:10.1175/1520-0469(1995)052<1875:IOOGWP>2.0.CO;2.

Kim, Y.-j., and J. D. Doyle, 2005: Extension of an orographic-drag parametrization scheme to incorporate orographic anisotropy and flow blocking. *Quarterly Journal of the Royal Meteorological Society*, **131 (609)**, 1893–1921, doi:10.1256/qj.04.160.

Kim, Y.-J., S. D. Eckermann, and H.-Y. Chun, 2003: An overview of the past, present and future of gravity-wave drag parametrization for numerical climate and weather prediction models. *Atmosphere-Ocean*, **41 (1)**, 65–98, doi:10.3137/ao.410105.

Klemp, J. B., and D. R. Durran, 1987: Numerical modelling of Bora winds. *Meteorology and Atmospheric Physics*, **36 (1)**, 215–227, doi:10.1007/BF01045150.

Klemp, J. B., and D. K. Lilly, 1975: The Dynamics of Wave-Induced Downslope Winds. *Journal of the Atmospheric Sciences*, **32 (2)**, 320–339, doi:10.1175/1520-0469(1975)032<0320:TDOWID>2.0.CO;2.

Klemp, J. B., and D. K. Lilly, 1978: Numerical Simulation of Hydrostatic Mountain Waves. *Journal of the Atmospheric Sciences*, **35 (1)**, 78–107, doi:10.1175/1520-0469(1978)035<0078:NSOHMW>2.0.CO;2.

Klemp, J. B., and R. B. Wilhelmson, 1978: The Simulation of Three-Dimensional Convective Storm Dynamics. *Journal of the Atmospheric Sciences*, **35 (6)**, 1070–1096, doi:10.1175/1520-0469(1978)035<1070:TSOTDC>2.0.CO;2.

Laprise, J. P. R., 1993: An Assessment of the WKBJ Approximation to the Vertical Structure of Linear Mountain Waves: Implications for Gravity-Wave Drag Parameterization. *Journal of the Atmospheric Sciences*, **50 (11)**, 1469–1487, doi:10.1175/1520-0469(1993)050<1469:AAOTWA>2.0.CO;2.

Lawson, J., and J. Horel, 2015a: Analysis of the 1 December 2011 Wasatch Downslope Windstorm. *Weather and Forecasting*, **30 (1)**, 115–135, doi:10.1175/WAF-D-13-00120.1.

Lawson, J., and J. Horel, 2015b: Ensemble Forecast Uncertainty of the 1 December 2011 Wasatch Windstorm. *Weather and Forecasting*, **30 (6)**, 1749–1761, doi:10.1175/WAF-D-15-0034.1.

Leith, C. E., 1974: Theoretical Skill of Monte Carlo Forecasts. *Monthly Weather Review*, **102 (6)**, 409–418, doi:10.1175/1520-0493(1974)102<0409:TSOMCF>2.0.CO;2.

Long, R. R., 1953: Some Aspects of the Flow of Stratified Fluids: I. A Theoretical Investigation. *Tellus*, **5 (1)**, 42–58, doi:10.3402/tellusa.v5i1.8563.

Lorenz, E. N., 1969: The predictability of a flow which possesses many scales of motion. *Tellus*, **21 (3)**, 289–307, doi:10.3402/tellusa.v21i3.10086.

Lott, F., 1998: Linear mountain drag and averaged pseudo-momentum flux profiles in the presence of trapped lee waves. *Tellus A: Dynamic Meteorology and Oceanography*, **50 (1)**, 12–25, doi:10.3402/tellusa.v50i1.14509.

Lott, F., and M. J. Miller, 1997: A new subgrid-scale orographic drag parametrization: Its formulation and testing. *Quart. J. Roy. Meteor. Soc.*, **123 (537)**, 101–127, doi:10.1002/qj.49712353704.

Marks, C. J., and S. D. Eckermann, 1995: A Three-Dimensional Nonhydrostatic Ray-Tracing Model for Gravity Waves: Formulation and Preliminary Results for the Middle Atmosphere. *Journal of the Atmospheric Sciences*, **52 (11)**, 1959–1984, doi:10.1175/1520-0469(1995)052<1959:ATDNRT>2.0.CO;2.

Mass, C. F., and D. Ovens, 2021: The Synoptic and Mesoscale Evolution Accompanying the 2018 Camp Fire of Northern California. *Bulletin of the American Meteorological Society*, **102 (1)**, E168–E192, doi:10.1175/BAMS-D-20-0124.1.

McFarlane, N., 1987: The effect of orographically excited gravity wave drag on the general circulation of the lower stratosphere and troposphere. *J. Atmos. Sci.*, **44 (14)**, 1775–1800.

Metz, J. J., and D. R. Durran, 2021: Are finite-amplitude effects important in non-breaking mountain waves? *Quarterly Journal of the Royal Meteorological Society*, **n/a (n/a)**, doi:10.1002/qj.4045.

Metz, J. J., D. R. Durran, and P. N. Blossey, 2020: Unusual Trapped Mountain Lee Waves with Deep Vertical Penetration and Significant Stratospheric Amplitude. *Journal of the Atmospheric Sciences*, **77 (2)**, 633–646, doi:10.1175/JAS-D-19-0093.1.

Murphy, J. M., 1988: The impact of ensemble forecasts on predictability. *Quarterly Journal of the Royal Meteorological Society*, **114 (480)**, 463–493, doi:10.1002/qj.49711448010.

Nance, L. B., and B. R. Colman, 2000: Evaluating the Use of a Nonlinear Two-Dimensional Model in Downslope Windstorm Forecasts. *Weather and Forecasting*, **15 (6)**, 715–729, doi:10.1175/1520-0434(2000)015<0715:ETUOAN>2.0.CO;2.

Nuss, W. A., and D. K. Miller, 2001: Mesoscale predictability under various synoptic regimes. *Nonlinear Processes in Geophysics*, **8 (6)**, 429–438, doi:10.5194/npg-8-429-2001.

Palmer, T., G. Shutts, and R. Swinbank, 1986: Alleviation of a systematic westerly bias in general circulation and numerical weather prediction models through an orographic gravity wave drag parametrization. *Quart. J. Roy. Meteor. Soc.*, **112 (474)**, 1001–1039.

Peltier, W. R., and T. L. Clark, 1979: The Evolution and Stability of Finite-Amplitude Mountain Waves. Part II: Surface Wave Drag and Severe Downslope Windstorms. *Journal of the Atmospheric Sciences*, **36 (8)**, 1498–1529, doi:10.1175/1520-0469(1979)036<1498:TEASOF>2.0.CO;2.

Peltier, W. R., and T. L. Clark, 1983: Nonlinear mountain waves in two and three spatial dimensions. *Quarterly Journal of the Royal Meteorological Society*, **109 (461)**, 527–548, doi:10.1002/qj.49710946106.

Queney, P., 1948: The Problem of Air Flow Over Mountains: A Summary of Theoretical Studies. *Bulletin of the American Meteorological Society*, **29 (1)**, 16–26.

Reinecke, P. A., and D. R. Durran, 2009: Initial-Condition Sensitivities and the Predictability of Downslope Winds. *Journal of the Atmospheric Sciences*, **66 (11)**, 3401–3418, doi:10.1175/2009JAS3023.1.

Sandu, I., P. Bechtold, A. Beljaars, A. Bozzo, F. Pithan, T. G. Shepherd, and A. Zadra, 2016: Impacts of parameterized orographic drag on the Northern Hemisphere winter circulation. *Journal of Advances in Modeling Earth Systems*, **8 (1)**, 196–211, doi:10.1002/2015MS000564.

Satoh, M., B. Stevens, F. Judt, M. Khairoutdinov, S.-J. Lin, W. M. Putman, and P. Düben, 2019: Global Cloud-Resolving Models. *Current Climate Change Reports*, **5 (3)**, 172–184, doi:10.1007/s40641-019-00131-0.

Schaefer, J. T., 1990: The Critical Success Index as an Indicator of Warning Skill. *Weather and Forecasting*, **5 (4)**, 570–575, doi:10.1175/1520-0434(1990)005<0570:TCSIAA>2.0.CO;2.

Schwartz, C. S., G. S. Romine, R. A. Sobash, K. R. Fossell, and M. L. Weisman, 2018: NCAR's Real-Time Convection-Allowing Ensemble Project. *Bulletin of the American Meteorological Society*, **100 (2)**, 321–343, doi:10.1175/BAMS-D-17-0297.1.

Scinocca, J. F., and N. A. McFarlane, 2000: The parametrization of drag induced by stratified flow over anisotropic orography. *Quarterly Journal of the Royal Meteorological Society*, **126 (568)**, 2353–2393, doi:10.1002/qj.49712656802.

Scorer, R., 1949: Theory of waves in the lee of mountains. *Quart. J. Roy. Meteor. Soc.*, **75**, 41–56.

Smith, R. B., 1976: The Generation of Lee Waves by the Blue Ridge. *Journal of the Atmospheric Sciences*, **33 (3)**, 507–519, doi:10.1175/1520-0469(1976)033<0507:TGOLWB>2.0.CO;2.

Smith, R. B., 1985: On Severe Downslope Winds. *Journal of the Atmospheric Sciences*, **42 (23)**, 2597–2603, doi:10.1175/1520-0469(1985)042<2597:OSDW>2.0.CO;2.

Smith, R. B., and C. G. Kruse, 2017: Broad-Spectrum Mountain Waves. *Journal of the Atmospheric Sciences*, **74 (5)**, 1381–1402, doi:10.1175/JAS-D-16-0297.1.

Smith, R. B., B. K. Woods, J. Jensen, W. A. Cooper, J. D. Doyle, Q. Jiang, and V. Grubišić, 2008: Mountain Waves Entering the Stratosphere. *Journal of the Atmospheric Sciences*, **65 (8)**, 2543–2562, doi:10.1175/2007JAS2598.1.

Smith, R. B., and Coauthors, 2016: Stratospheric Gravity Wave Fluxes and Scales during DEEPWAVE. *Journal of the Atmospheric Sciences*, **73 (7)**, 2851–2869, doi:10.1175/JAS-D-15-0324.1.

Sugarbaker, L. J., E. W. Constance, H. K. Heidemann, A. L. Jason, V. Lukas, D. L. Saghy, and J. M. Stoker, 2014: The 3D Elevation Program initiative—A call for action. U. S. Geological Survey Circular 1399, 35 pp.

Teixeira, M. A. C., and J. L. Argaín, 2020: The dependence of mountain wave reflection on the abruptness of atmospheric profile variations. *Quarterly Journal of the Royal Meteorological Society*, **146 (729)**, 1685–1701, doi:10.1002/qj.3760.

Walters, D., and Coauthors, 2017: The Met Office Unified Model Global Atmosphere 6.0/6.1 and JULES Global Land 6.0/6.1 configurations. *Geoscientific Model Development*, **10 (4)**, 1487–1520.

Warner, T. T., 2010: *Numerical Weather and Climate Prediction*. Cambridge University Press.

Wells, H., and S. B. Vosper, 2010: The accuracy of linear theory for predicting mountain-wave drag: Implications for parametrization schemes. *Quarterly Journal of the Royal Meteorological Society*, **136 (647)**, 429–441, doi:10.1002/qj.578.

Weyn, J. A., and D. R. Durran, 2017: The Dependence of the Predictability of Mesoscale Convective Systems on the Horizontal Scale and Amplitude of Initial Errors in Idealized Simulations. *Journal of the Atmospheric Sciences*, **74 (7)**, 2191–2210, doi:10.1175/JAS-D-17-0006.1.

Zhou, L., S.-J. Lin, J.-H. Chen, L. M. Harris, X. Chen, and S. L. Rees, 2019: Toward Convective-Scale Prediction within the Next Generation Global Prediction System. *Bulletin of the American Meteorological Society*, **100 (7)**, 1225–1243, doi:10.1175/BAMS-D-17-0246.1.

VITA

Johnathan Metz grew up in south-western and south-central North Dakota. Throughout his childhood, the variety of extreme weather found on the Northern Plains—from severe thunderstorms and tornadoes to blizzards—fascinated him. He decided to pursue a degree in atmospheric sciences from the University of North Dakota, where he graduated with a Bachelor of Science in 2015. While at UND, he was awarded an Ernest F. Hollings Scholarship from the National Oceanic and Atmospheric Administration. He completed his Hollings internship, which focused on orographic gravity wave drag parameterizations in global atmospheric models, under the guidance of Mike Fiorino at the Earth System Research Laboratory in Boulder, Colorado. As a result of this work, Johnathan was awarded the Father James B. Macelwane Annual Award in Meteorology from the American Meteorological Society.

With a newfound interest in gravity waves, Johnathan applied to the University of Washington, which he entered as a graduate student in 2015. While at the University of Washington, Johnathan worked with Dale Durran and studied the impacts of mountains on multiple phenomena, including unusual stratospheric trapped-lee waves downstream of New Zealand, the influence of finite-amplitude effects on the amplitude of mountain waves, and the predictability of downslope windstorms. He has published two papers based upon this work, and a third is in preparation. Johnathan earned a Master of Science in Atmospheric Sciences in 2018, a second Master of Science in Applied Mathematics in 2021, and his Ph.D. in 2021.